Crustal Radial Anisotropy Across Eastern Tibet and the Western Yangtze Craton

Jiayi Xie[1], Michael H. Ritzwoller[1], Weisen Shen[1], Yingjie Yang[2], Yong Zheng[3], and Longquan Zhou[4]

1 – Center for Imaging the Earth's Interior, Department of Physics, University of Colorado at Boulder, Boulder, CO, 80309, USA (jiayi.xie@colorado.edu)
2 – Department of Earth and Planetary Sciences, Macquarie University, 2109, Sydney Australia
3 – State Key Laboratory of Geodesy and Earth's Dynamics, Institute of Geodesy and Geophysics, CAS, Wuhan, 430077, China
4 - China Earthquake Network Center, Beijing, 100045, China

Abstract

Phase velocities across eastern Tibet and surrounding regions are mapped using Rayleigh (8-65 sec) and Love (8-44 sec) wave ambient noise tomography based on data from more than 400 PASSCAL and CEArray stations. A Bayesian Monte-Carlo inversion method is applied to generate 3-D distributions of Vsh and Vsv in the crust and uppermost mantle from which radial anisotropy and isotropic Vs are estimated. Each distribution is summarized with a mean and standard deviation, but is also used to identify "highly probable" structural attributes, which include (1) positive mid-crustal radial anisotropy (Vsh > Vsv) across eastern Tibet (spatial average = 4.8% $\pm$ 1.4%) that terminates abruptly near the border of the high plateau, (2) weaker (-1.0% $\pm$ 1.4%) negative radial anisotropy (Vsh < Vsv) in the shallow crust mostly in the Songpan-Ganzi terrane, (3) negative mid-crustal anisotropy (-2.8% $\pm$ 0.9%) in the Longmenshan region, (4) positive mid-crustal radial anisotropy (5.4% $\pm$ 1.4%) beneath the Sichuan Basin, and (5) low Vs in the middle crust (3.427 $\pm$ 0.050 km/s) of eastern Tibet. Mid-crustal Vs < 3.4 km/s (perhaps consistent with partial melt) is highly probable only for three distinct regions: the northern Songpan-Ganzi, the northern Chuandian, and part of the Qiangtang terranes. Mid-crustal anisotropy provides evidence for sheet silicates (micas) aligned by deformation with a shallowly dipping foliation plane beneath Tibet and the Sichuan Basin and a steeply dipping or subvertical foliation plane in the Longmenshan region. Near vertical cracks or faults are believed to cause the negative anisotropy in the shallow crust underlying Tibet.

1. Introduction

The amplitude and distribution of elastic anisotropy in earth's crust and mantle provide valuable information about the deformation history of the solid earth. Mantle anisotropy has been particularly well studied in the laboratory and in the field and is believed principally to reflect the lattice preferred orientation of olivine produced by mantle kinematics [e.g., *Schlue and Knopoff, 1977; Montagner and Anderson, 1989; Montager and Tanimoto*, 1991; *Ekström and Dziewonski*, 1998; *Mainprice*, 2007; *Becker et al.,* 2008]. Crustal anisotropy has probably been explored less fully although seismological studies that relate observed anisotropy to crustal deformation and metamorphism have been developing rapidly [e.g., *Okaya et al*., 1995; *Levin and Park*, 1997; *Godfrey et al*., 2000; *Vergne et al*., 2003; *Ozacar and Zandt*, 2004; *Shapiro et al.*, 2004; *Sherrington et al*., 2004; *Champion et al*., 2006; *Xu et al*., 2007; *Readman et al*., 2009]. In parallel, petrophysical understanding of the causes of crustal anisotropy has also been growing quickly [e.g., *Barruol and Mainprice,* 1993; *Nishizawa and Yoshino*, 2001; *Okaya and McEvilly*, 2003; *Cholach et al.*, 2005; *Cholach and Schmitt*, 2006; *Kitamura*, 2006; *Mahan*, 2006; *Barberini et al.*, 2007; *Tatham et al*., 2008; *Lloyd et al.*, 2009; *Ward et al.*, 2012*; Erdman et al.*, 2013]. With the development of ambient noise tomography, surface waves now can be observed at periods short enough to allow shear wave speed models to be constructed at crustal depths including models both of azimuthal [e.g., *Lin et al.*, 2011; *Xie et al*., 2012] and polarization or radial [e.g., *Bensen et al*., 2009; *Huang et al*., 2010; *Moschetti et al*., 2010a, 2010b; *Takeo et al*., 2013] anisotropy. The current paper reports on the application of ambient noise tomography to infer radial anisotropy in eastern Tibet and surrounding regions.

Radial anisotropy is a property of a medium in which the speed of the wave depends on its polarization and direction of propagation. For a transversely isotropic medium, such as a medium with hexagonal symmetry with a vertical symmetry axis, there are two shear wave speeds: Vsv and Vsh. In such a medium, a shear wave that is propagating horizontally and polarized vertically or a shear wave that is propagating vertically and polarized horizontally will propagate with speed Vsv. In contrast, a wave that is propagating in a horizontal direction and polarized horizontally will propagate with speed Vsh. We refer to this difference in wave speed as Vs radial anisotropy or in some places merely as radial anisotropy, which is represented here as the percentage difference between Vsh and Vsv in the medium: $\gamma = (\mathrm{Vsh}-\mathrm{Vsv})/\mathrm{Vs}$. In this case, Vs is the isotropic or effective shear wave speed, and is computed from Vsh and Vsv via a Voigt-average, $\mathrm{Vs} = \sqrt{(2\mathrm{Vsv}^2 + \mathrm{Vsh}^2)/3}$ [*Babuška and Cara*, 1991].

The direct observation of radial anisotropy with regionally propagating shear waves, which are confined to the crust and uppermost mantle, is extremely difficult. Thus, the existence of radial anisotropy is typically inferred from observations of a period-dependent discrepancy between the phase or group speeds of Rayleigh and Love waves. As discussed later in the paper and in many other papers [e.g., *Anderson and Dziewonski*, 1982; *Montagner and Nataf*, 1986], Rayleigh waves are strongly sensitive to Vsv and Love waves to Vsh. The Rayleigh-Love discrepancy is identified by the inability of a simply parameterized isotropic shear velocity model to fit the dispersion characteristics of both types of waves simultaneously. Observations of this discrepancy attributed to radial anisotropy in the mantle in which Vsh > Vsv date back about half a century [*Aki*, 1964; *Aki and Kaminuma*, 1963; *McEvilly*, 1964; *Takeuchi et al.*, 1968]. Much more recently, radial anisotropy in the uppermost mantle has been mapped worldwide [*Montagner and Tanimoto*, 1991; *Trampert and Woodhouse*, 1995; *Babuška et al.*, 1998; *Ekström and Dziewonski*, 1998; *Shapiro and Ritzwoller*, 2002; *Nettles and Dziewoński*, 2008], and there have also been inroads made into mapping radial anisotropy in the crust beneath the US [*Bensen et al.*, 2009; *Moschetti and Yang*, 2010; *Moschetti et al.*, 2010] and Tibet [*Shapiro et al.*, 2004; *Chen et al.*, 2010; *Duret et al.*, 2010; *Huang et al.*, 2010]. The observations in Tibet are part of a steady improvement in the reliability and the lateral and radial resolutions of surface wave dispersion studies that cover all [*Ritzwoller et al.,* 1998; *Villaseñor et al.*, 2001; *Levshin et al.*, 2005; *Maceira et al.*, 2005; *Zheng et al., 2010; Caldwell et al.*, 2009; *Acton et al.*, 2010; *Yang et al.*, 2010, 2012] or parts of the high plateau [*Levshin et al.*, 1994; *Cotte et al.*, 1999; *Rapine et al.*, 2003; *Yao et al.*, 2008, 2010; *Guo et al.*, 2009; *Li et al.*, 2009; *Jiang et al.*, 2011; *Zhou et al.*, 2012].

The observation of crustal radial anisotropy has been taken as evidence for the existence of strong elastically anisotropic crustal minerals aligned by strains associated with processes of deformation [*Shapiro et al.*, 2004; *Moschetti et al.*, 2010]. Many continental crustal minerals are strongly anisotropic as single crystals [*Barruol and Mainprice*, 1993; *Mahan*, 2006], but some of the most common minerals (e.g., feldspars, quartz) have geometrically complicated anisotropic patterns that destructively interfere with polycrystalline aggregates [*Lloyd et al.*, 2009; *Ward et al.*, 2012]. Micas and amphiboles are exceptions that exhibit more robust alignment in both crystallographic direction and shape that produce simple patterns of seismic anisotropy [*Tatham et al.*, 2008; *Lloyd et al.*, 2009]. For this reason, recent observations of strong anisotropy in the middle crust have been attributed to the crystallographic preferred orientation (CPO) of mica

[*Nishizawa and Yoshino*, 2001; *Shapiro et al.*, 2004; *Moschetti et al.*, 2010]. In the lower crust, amphibole may also be an important contributor to seismic anisotropy [*Kitamura*, 2006; *Barberini et al.*, 2007; *Tatham et al.*, 2008].

Shapiro et al. [2004] showed that crustal radial anisotropy is strong in western Tibet and may extend into eastern Tibet where the resolution of their study was weaker. Subsequently, *Duret et al.* [2010] presented evidence from individual seismograms using aftershocks of the Wenchuan earthquake of 12 May 2008 that the Rayleigh-Love discrepancy is so significant for paths crossing Tibet that crustal radial anisotropy probably also extends into eastern Tibet. *Huang et al.* [2010] confirmed this expectation by mapping crustal radial anisotropy in far southeastern Tibet. Example cross-correlations of ambient noise for a path in the Qiangtang terrane (Figure 1) contain Rayleigh and Love waves as shown in Figure 2a. Figure 2b illustrates that a Rayleigh-Love discrepancy exists for this path, revealing that crustal radial anisotropy, indeed, is present between stations located within eastern Tibet.

The objective of this paper is to map crustal radial anisotropy across all of eastern Tibet (Figure 1), extending the results into adjacent areas north and east of the high plateau for comparison. Rayleigh and Love wave phase velocity curves are measured from ambient noise cross-correlations between each pair of simultaneously operating stations between 8 and 44 sec period for Love waves and 8 and 65 sec for Rayleigh waves. As shown later, the inability to observe Love waves at longer periods implies that radial anisotropy cannot be reliably mapped deeper than about 50 km, which means that we cannot place tight constraints on the strength of radial anisotropy in the lowermost crust beneath Tibet. For this reason, we focus discussion on mid-crustal radial anisotropy.

The inversion of surface wave data for a 3-D radially anisotropic shear wave speed model consists of two stages: first, a tomographic inversion is performed using measured Rayleigh and Love wave dispersion curves for period-dependent phase speed maps on a 0.5°×0.5° grid using the tomographic method of *Barmin et al.* [2001] with uncertainties estimated using eikonal tomography [*Lin et al.*, 2009] (Section 2), and second, a Bayesian Monte Carlo inversion [*Shen et al.*, 2013b] is carried out for a 3-D radially anisotropic shear velocity (Vsv, Vsh) model of the crust (Section 3). The inversion estimates the posterior distribution of accepted models at each location, which is used in two ways. First, at each grid node we summarize the distribution at each depth with its mean and standard deviation. Using the mean of the distribution, we show that strong mid-crustal positive (Vsh > Vsv) radial anisotropy is observed across all of eastern Tibet and terminates abruptly as the border of the high plateau is reached. It is also observed in the middle crust beneath the Sichuan Basin. Negative radial anisotropy (Vsv > Vsh) is observed in the shallow crust beneath eastern Tibet and in the middle crust of the Longmenshan region. Second, we also query the entire posterior distribution of models in order to determine which structural attributes are highly probable, which are only likely, and which are prohibited. Throughout, we attempt to address how uncertainties in prior knowledge (e.g., Vp/Vs in the crust) affect the key inferences. In particular, we investigate if prior constraints and assumptions are likely to bias the posterior distribution significantly. Finally, we ask how the observations reflect on the presence or absence of pervasive partial melt in the middle crust across Tibet and speculate on the physical causes of several observed radial anisotropy features.

2. Data processing and tomography

2.1 Love wave and Rayleigh wave tomography

For Love wave data processing, we apply the procedure described by *Bensen et al.* [2007] and *Lin et al.* [2008] to recordings at 362 stations (Figure 1), consisting of 180 PASSCAL and GSN stations and 182 Chinese Earthquake Array (CEArray) stations [*Zheng et al.*, 2010]. We downloaded all available horizontal component data for PASSCAL and GSN stations between years 2000 and 2011 from the IRIS DMC. Horizontal component data for the CEArray stations were acquired for the years 2007 through 2009. We cut horizontal component ambient noise records into 1-day long time series and then cross-correlate the transverse components (T-T) between all possible station pairs, after the performance of the time domain and frequency domain normalization procedures described by *Bensen et al.* [2007]. As *Lin et al.* [2008] demonstrated, Love wave energy dominates transverse-transverse (T-T) cross-correlations. *Yang et al*. [2008] showed that Rayleigh wave cross-correlations between stations in Tibet are typically not symmetric, but there is significant energy from most directions with the primary directions of propagation of the waves being dependent on both period and season. This is also true for Love waves, but the strongest waves (highest SNR) typically come from the southeast. After the cross-correlations, we applied automated frequency-time analysis (FTAN) [e.g., *Levshin and Ritzwoller*, 2001; *Bensen et al.*, 2007]) to produce Love wave phase speed curves for periods between 8 and 30 to 50 sec (depending on the signal-to-noise ratio) for each station pair.

Rayleigh wave phase speed measurements are obtained from cross-correlations of vertical-component ambient noise, the vertical-vertical (Z-Z) cross-correlations, which are rich in Rayleigh waves. *Yang et al.* [2010] generated Rayleigh wave phase velocity maps from ambient noise across the Tibetan Plateau. Instead of using their dispersion maps directly, we re-selected the measurements for stations within our study region and re-performed the tomography as described below. Example T-T and Z-Z cross-correlations and measured phase speeds between the station-pair X4.D26 and X4.F17 are shown in Figure 2**.**

For dispersion measurements at different periods, we exploited three criteria to identify reliable measurements: (1) the distance between two stations must be greater than two wavelengths to ensure sufficient separation of the surface wave packet from precursory arrivals and noise and to satisfy the far-field approximation (the use of a three-wavelength criterion changes results negligibly); (2) measurements must have a signal-to-noise ratio (SNR) > 10 for Love wave and SNR > 15 for Rayleigh wave to ensure the reliability of the signal; and (3) the observed travel times and those predicted from the associated phase velocity map between each accepted station-pair must agree within a specified tolerance [*Zhou et al.*, 2012]. We found that horizontal components are problematic (mainly relative to criterion (3) above) for 61 stations. Their removal left us with the 362 stations shown in Figure 1. The vertical components of 26 stations are similarly identified as problematic and are rejected from further analysis leaving 406 stations from which we obtain Rayleigh wave measurements. This procedure produces about 30,000 Love wave phase velocity curves and 40,000 Rayleigh wave curves.

Because eikonal tomography [*Lin et al.*, 2009] models off-great circle propagation, it would be preferable to straight ray tomography [*Barmin et al.*, 2001]. Eikonal tomography works best, however, where there are no spatial gaps in the array of stations.

There are gaps in our station coverage near 33°N, 100°E in eastern Tibet (Figure 1b). Thus, we apply straight-ray tomography [*Barmin et al.*, 2001] to generate phase velocity maps, but use eikonal tomography to estimate uncertainties in these maps, as described in Section 2.2. To reduce the effect of non-ideal azimuthal coverage at some locations, we simultaneously estimate azimuthal anisotropy, but these estimates are not used here. What results are Love wave phase velocity maps ranging from 8 to 44 sec and Rayleigh wave phase velocity maps from 8 to 65 sec period. Above 44 sec period, the SNR of Love waves decreases dramatically, which degrades the ability to produce reliable high-resolution maps. Examples of Rayleigh and Love wave phase speed maps at periods of 10 and 40 sec are shown in Figure 3. At 10 sec period, the maps are quite sensitive to shallow crustal structures to about 20 km depth including the existence of sediments, and at 40 sec period the maps are predominantly sensitive to structures near the Moho such as crustal thickness.

2.2 Uncertainties and local dispersion curves

Local uncertainty estimates for each of the phase speed maps provide the uncertainties used in the inversion for 3-D structure. Estimates of uncertainties in the Rayleigh and Love wave phase speed maps are determined by eikonal tomography [*Lin et al.*, 2009], which, as discussed above, does not produce uniformly unbiased phase speed estimates where there are gaps in station coverage. We find, however, that it does produce reliable uncertainty estimates, even in the presence of spatial gaps. Averaging the one-standard deviation uncertainty maps across the study region, average uncertainties are found to range between 0.012 to 0.057 km/s for Rayleigh waves and 0.016 to 0.060 km/s for Love waves (Figure 4), minimize between about 12 and 25 sec period, and increase at both shorter and longer periods. Because of the lower SNR and the smaller number of Love wave measurements, uncertainties for Love waves tend to be larger than for Rayleigh waves. In addition, the SNR decreases faster at long periods for Love waves than Rayleigh waves, so the uncertainty for Love waves at long periods is higher still than for Rayleigh waves. Uncertainties for both wave types increase toward the borders of the maps at all periods.

Having estimated maps of period-dependent dispersion and uncertainty, local Rayleigh and Love wave dispersion curves with associated uncertainties are generated on a 0.5°×0.5° grid across the study region. These data are the input for the 3-D model inversion that follows.

3. Bayesian Monte Carlo inversion of local dispersion curves

3.1 Model parameterization and prior constraints

The 3-D model comprises a set of 1-D models situated on a 0.5°×0.5° grid. Following *Shen et al.* [2013a, 2013b], each of the 1-D models is parameterized with three principal layers: a sedimentary layer, a crystalline crustal layer, and a mantle layer to a depth of 200 km. The sedimentary layer is isotropic and is described by two parameters: layer thickness and constant shear wave speed Vs. Anisotropy in the sedimentary layer is physically possible, but with the data used here cannot be resolved from anisotropy in the crystalline crust. In addition, it has little affect in the period range of the observed Rayleigh-Love discrepancy as discussed further in Section 4. For these reasons, we include anisotropy only below the sediments.

We represent anisotropy through the elastic moduli of a transversely anisotropic medium (also referred to as radial anisotropy). In such a medium the elastic tensor is specified by five moduli: A, C, L, N, and F. The moduli A and C are related to the P-wave speeds (Vph, Vpv) and L and N are related to the S-wave speeds (Vsv, Vsh) as follows: $A = \rho V^2_{ph}$, $C = \rho V^2_{pv}$, $L = \rho V^2_{sv}$, and $N = \rho V^2_{sh}$, where ρ is density. Some authors summarize radial anisotropy with three derived parameters: $\xi = N/L = (Vsh/Vsv)^2$, $\phi = C/A = (Vpv/Vph)^2$, and $\eta = F/(A-2L)$. We prefer to summarize Vs and Vp anisotropy with two different parameters in addition to η, defined as follows: $\gamma = (Vsh - Vsv)/Vs$ and $\varepsilon = (Vph - Vpv)/Vp$, where Vs is the Voigt average of Vsh and Vsv and Vp similarly is the Voigt average of Vph and Vpv. We refer to γ as Vs radial anisotropy and ε as Vp radial anisotropy. These parameters are simply related to those used by some other authors: $\gamma + 1 \approx \xi^{1/2}$ and $\varepsilon + 1 \approx \phi^{-1/2}$. In an isotropic medium, Vsh = Vsv, Vph = Vpv, and F = A – 2L, thus $\xi = \phi = \eta = 1$ and $\gamma = \varepsilon = 0$.

We make the simplifying (but nonphysical) assumption that only Vs anisotropy is present in the elastic tensor in the crust and mantle. Thus, we allow Vsh to differ from Vsv, but restrict Vph = Vpv ($\varepsilon = 0$) and $\eta = 1$. Strictly speaking this is physically unrealistic because in real mineral assemblages Vs anisotropy would be accompanied by Vp anisotropy with η differing from unity [e.g., *Babuška and Cara*, 1991; *Erdman et al.*, 2013]. In Section 5.4.4 we show, however, that the effect of this assumption on our estimate of crustal Vs anisotropy is negligible. Therefore, although we represent radial anisotropy in terms of Vs anisotropy alone, our results are consistent with the inclusion of Vp anisotropy in the elastic tensor along with η that differs from unity.

The crystalline crustal layer is described by nine parameters: layer thickness, five B-splines (1-5) for Vsv (Figure 5), and three more independent B-splines for Vsh (2-4). We set Vsh = Vsv for B-splines 1 and 5. Because B-splines 2 and 4 extend into the uppermost and lowermost crust, respectively, radial anisotropy can extend into these regions but its amplitude will be reduced relative to models in which Vsh and Vsv for B-splines 1 and 5 are free. The effect of this constraint is discussed in Section 5.4.1.

Mantle structure is modeled from the Moho to 200 km depth with five B-splines for Vsv. Vsh in the mantle differs from Vsv by the depth-dependent strength of radial anisotropy taken from the 3-D model of *Shapiro and Ritzwoller* [2002]. Thus, in the mantle we estimate Vsv, but set Vsh = Vsv +δV where δV is the difference between Vsh and Vsv in the model of *Shapiro and Ritzwoller* [2002]. Below 200 km the model reverts to the 1D model ak135 [*Kennett et al.*, 1995]. The effect on estimates of crustal anisotropy caused by fixing the amplitude of mantle anisotropy is considered in Section 5.4.2. Overall, there are 16 free parameters at each point and the model parameterization is uniform across the study region.

Because Rayleigh and Love wave velocities are mainly sensitive to shear wave speeds, other variables in the model such as compressional wave speed, Vp, and density, ρ, are scaled to the isotropic shear wave speed model, Vs. Vp is converted from Vs using a Vp to Vs ratio such that Vp/Vs is 2.0 in the sediments and 1.75 in the crystalline crust and mantle, consistent with a Poisson solid. For density, we use a scaling relation that has been influenced by the studies of *Christensen and Mooney* [1995] and *Brocher* [2005] in the crust, and by *Karato* [1993] in the mantle where sensitivity to density structure is much weaker than in the crust. The Q model comes from ak135 [*Kennett et al.*, 1995] with some modifications: shear Q is 600 in the upper 20 km and 400 between 20 and 80 km depth outside the Tibetan Plateau, while we set it to 250 within the Tibetan Plateau [*Levshin et al.*, 2010]. Vs, Vsv, and Vsh are converted to a reference period of 1 sec. To test the effect of uncertainties in the physical dispersion correction [*Kanamori and Anderson*, 1977] on estimates of Vsv and Vsv caused by ignorance of the Q of the crust, we lowered values of Q from 250 to 100 between 20 and 80 km depth. We found that the amplitude of the resulting depth averaged crustal radial anisotropy decreased only slightly for the smaller Q beneath point B shown in Figure 1a. As a constant Q of 100 between these depths is almost certainly too low and we are concerned with anisotropy amplitudes greater than 1%, uncertainties in the Q model can be ignored here.

To avoid consideration of physically unreasonable models, we imposed prior constraints on the parameter space explored in the inversion. (1) Although velocity is not constrained to increase monotonically with depth, it cannot decrease with depth at a rate ($-\Delta v/\Delta h$) larger than 1/70 s^{-1}. This constraint reduces (but does not entirely eliminate) the tendency of the shear-wave speeds to oscillate with depth. (2) Shear-wave speeds increase with depth across the sediment-basement interface and across Moho. (3) Both Vsv and Vsh are constrained to be less than 4.9 km/s at all depths. (4) The amplitude of radial anisotropy in the uppermost and lowermost crust is constrained by setting Vsh=Vsv for splines 1 and 5 (Figure 5). The last constraint is imposed to mitigate against radial anisotropy oscillating with depth, and its effect is discussed further in Section 5.4.1.

The model space is then explored starting with perturbations (Table 1) to a reference model consisting of sedimentary structure from *Laske and Masters* [1997] and crystalline crustal and uppermost mantle structure from *Shapiro and Ritzwoller* [2002]. Imposing the prior constraints in model space defines the prior distribution of models, which aims to quantify the state of knowledge before data are introduced. In particular, a new model m_i is generated by perturbing the initial model m_0 following the procedure described by *Shen et al.* [2013b]. The set of all models that can be produced in this way is called the prior distribution and example plots for various model variables are shown in Figure 6.

3.2 Inversion procedure

With the parameterization and constraints described above, we perform a Bayesian Monte Carlo inversion based on the method described by *Shen et al.* [2013b]. This method is modified to produce a radially anisotropic model using both Love and Rayleigh wave data without receiver functions. The main modifications lie in the forward calculation of surface wave dispersion for a transversely isotropic (radially anisotropic) medium, which we base on the code MINEOS [*Masters et al.,* 2007]. Unlike most seismic dispersion codes, the MINEOS code consistently models a transversely isotropic medium. In order to accelerate the forward calculation, we compute numerical first-order partial derivatives relative to each model parameter. Given the range of model space explored, the use of first-derivatives is sufficiently accurate [*James and Ritzwoller*, 1999; *Shapiro and Ritzwoller*, 2002]. For every spatial location, we start from the reference model described above, $\boldsymbol{p}_{ref}$, and the corresponding Rayleigh or Love wave dispersion curves, $\boldsymbol{D}_{ref}$, and the partial derivatives $(\partial \mathrm{D}/\partial \mathrm{p}_\mathrm{i})$ are computed numerically for all 16 free parameters using the MINEOS code. With these partial derivatives, dispersion curves $\boldsymbol{D}$ for any model $\boldsymbol{p}$ may be approximated as:

$$\boldsymbol{D} = \boldsymbol{D}_{ref} + \sum_{\boldsymbol{i}} \left(\frac{\partial \boldsymbol{D}_{\boldsymbol{ref}}}{\partial p_i}\right) \delta p_i \qquad (1)$$

where $\delta p_i = p_i - p_{ref\,i}$, is the perturbation to model parameter *i*.

The model space sampling process is guided by the Metropolis law, and goes as follows. Within the model space defined by the prior information, an initial model m_0 is chosen randomly from the prior distribution, and its likelihood function $L(m_0)$ is computed:

$$L(m) = \exp\left(-\frac{1}{2}S(m)\right) \tag{2}$$

where

$$S(m) = S_{Rayleigh} + S_{Love} = \sum_i \frac{(D(m)_i^{pred} - D_i^{obs})^2}{\sigma_i^2} + \sum_i \frac{(D'(m)_i^{pred} - D'^{obs}_i)^2}{\sigma'^2_i} \tag{3}$$

where $D(m)_i^{pred}$ is the predicted phase velocity for model *m* at period *i* (computed from (1)), and D_i^{obs} is the observed phase velocity. Here, D represents Rayleigh wave phase velocities and D' indicates Love wave phase velocities. Standard deviations of the Rayleigh and Love wave phase velocity measurements are given by σ and σ', respectively.

A new model m_i is generated by perturbing the initial model m_0 following the procedure described by *Shen et al.* [2013b]. The likelihood function $L(m_i)$ is obtained through a similar computation as described above. The model m_i is accepted or rejected according to a probability function *P* defined as follows:

$$P_{accept} = \min\left(1, L(m_i)/L(m_0)\right) \tag{4}$$

If m_i is not accepted, a new m_i is generated by perturbing the initial model m_0; this perturbation continues until a m_i is accepted. If m_i is accepted, the next model sampled in model space will be based on it rather than m_0. This sampling process repeats until the likelihood function levels off, after which a new initial model is chosen randomly from the prior distribution. The process is continued until at least 5000 models have been accepted from at least 5 initial starting points. We then calculate average values of each parameter in the >5000 accepted models and take that average as a new reference model, and then recalculate dispersion curves and partial derivatives. With this new reference model and a similar sampling procedure, we repeat the process until we find an additional 5000 models accepted from at least 10 initial starting points. The use of various initial models minimizes the dependence on the initial parameters, but we find that initial model dependence is weak. That is, convergence tends to be to similar models irrespective of the initial model starting point.

The use of partial derivatives aims to accelerate computations during the process of identifying acceptable models in the Monte-Carlo search. In order to eliminate possible bias caused by the use of the partial derivatives, the Rayleigh and Love wave phase velocity curves are recomputed for each accepted model using MINEOS when the algorithm terminates at each location. This recomputation of the dispersion curves actually takes longer than the entire Monte-Carlo search, but there is little difference between the dispersion curves computed with MINEOS and the partial derivatives. This justifies reliance on the partial derivatives to save computation time without sacrificing accuracy.

The Monte Carlo sampling will generate an ensemble of anisotropic models that fit the data better than the reference model. The ensemble is reduced further in size by an additional acceptance criterion defined as follows:

$$\chi \leq \begin{cases} \chi_{min} + 0.5 & if\ \chi_{min} < 0.5 \\ 2\,\chi_{min} & if\ \chi_{min} \geq 0.5 \end{cases}$$

where misfit $\chi = \sqrt{S/N}$ is the square root of reduced chi-squared value, S is misfit defined by equation (3), and N is the number of observed data (number of discrete points along the Rayleigh and Love wave phase velocity curves). Thus, on average, this posterior distribution includes models whose misfit is less than about twice that of the best-fitting model, which has a square root of reduced chi-squared value of χ_{min}.

Finally, the mean and standard deviation of Vsv and Vsh are used to summarize the posterior distribution for each depth and location. As an example, consider point B (Figure 1a), where mid-crustal anisotropy is needed to fit the data (Figure 6). The widths of the posterior distributions reflect how well Vsv, Vsh, and their differences are constrained at each depth. Uncertainties in shear wave speeds at depths of 20 and 35 km are less than about 50 m/s, but are about twice as large at 50 km. Moreover, radial anisotropy is inescapable at 20 and 35 km depth, but not required, if still likely, at 50 km. The poorer resolution at 50 km results from the lack of long-period Love wave data, increasing data uncertainties with period, and the tradeoff between lower crustal and uppermost mantle structures. Therefore, as mentioned earlier, we mainly focus discussion on structures no deeper than about 50 km.

We performed the Bayesian Monte Carlo inversion at every grid point in the study region to produce posterior distributions. In Section 4, we present the spatial variations in the means and standard deviations of the distribution. Then in Section 5, we query the entire distribution to address particular scientific questions.

4. Inversion Results

4.1 Example results at various locations

As examples of local dispersion curves and the results of their inversion to produce a radially anisotropic model, we consider results at four locations in different parts of eastern Tibet and its surroundings (Figure 1a, points A-D). For point A, which is north of the Kunlun fault near the eastern edge of the Qaidam Basin, the gray-shaded areas of the inverted model representing the 1σ uncertainty of the posterior distribution of accepted models in Vsh and Vsv (Figure 7b) give no indication of crustal radial anistropy. Vsh and Vsv are approximately equal in the crust, and no Rayleigh-Love discrepancy is observed (Figure 7a). In contrast, for point B in in the middle of eastern Tibet, a strong Rayleigh-Love discrepancy is seen for all isotropic models (Figure 7c), and large differences are required in Vsh and Vsv between ~20 and 50 km depth, as large as about 7.8%±1.6% (Figure 7d). The model uncertainty increases near the base of the sedimentary layer (not shown) and near the Moho, which reflects the velocity-depth tradeoff near interfaces characteristic of surface wave inversions. This prevents precise imaging of the discontinuities using surface waves alone. Although the inversion is performed to a depth of 200 km, we concentrate discussion on the crust where radial anisotropy is well resolved.

For point C in the Sichuan Basin, the Rayleigh and Love wave dispersion curves (Figure 7e) call for anisotropy only in the upper 20 km of crust (Figure 7f). As discussed in Section 4.3, the anisotropy could be confined to the sediments but would need to be about four times stronger. For point D in the Longmenshan region between Tibet and the Sichuan Basin, mid-crustal radial anisotropy is required, but in this case Vsv > Vsh and radial anisotropy is negative.

In Figure 7, green lines on the dispersion curves represent the predicted curves for the best-fitting isotropic Vs model in the crust, although the mantle contains radial anisotropy. They show the observed Rayleigh-Love discrepancy, how the best-fitting isotropic model misfits the data at points B, C, and D where radial anisotropy is required in the middle crust.

4.2 Maps of Vsv, Vsh, and Voigt-averaged Vs

Maps of the mean of the resulting posterior distributions for Vsv, Vsh, and the Voigt averaged isotropic Vs in the middle crust of Tibet (~35 km) are shown in Figure 8, in addition to the mean of crustal thickness. The most prominent feature is the low mid-crustal shear wave speed across all of eastern Tibet compared with much higher speeds outside of Tibet. In the mid-crustal Vsv map (Figure 8a), anomalies are similar to those presented in an earlier study using a similar data set [*Yang et al.*, 2012]. The Vsh model is faster than Vsv across the high plateau, indicating strong positive radial anisotropy. Combining Vsv and Vsh, an isotropic Vs estimate is computed from the Voigt averaging method mentioned in Section 1. In these maps, white contours outline regions with shear wave speeds lower than 3.4 km/s, below which partial melting may be expected to exist [e.g., *Yang et al.*, 2012]. Although Vsv < 3.4 km/s exists across much of eastern Tibet, Vsh > 3.4 km/s is present across the majority of the region. The difference between Vsv and Vsh causes the white contour in the Vsv map to contract toward the interior of eastern Tibet in the Vs map, predominantly within the Songpan-Ganzi and the northern Chuandian terrane. This feature of the Vs model is discussed further in Section 5.

4.3 Radial anisotropy

From the posterior distributions of Vsv and Vsh at each location we obtain the radial anisotropy model. Radial anisotropy at different depths and along different vertical profiles is shown in Figures 9 and 10. In this section we first discuss the distribution of radial anisotropy qualitatively, and then the estimated uncertainties are presented and discussed in Section 4.4.

In the upper crust (Figure 9a), radial anisotropy beneath the Tibetan Plateau is negative, on average. Beneath the Sichuan Basin, in contrast, it is positive with amplitudes in excess of 6%. Actually, the depth extent of the strong upper crustal radial anisotropy beneath the Sichuan Basin is not well constrained by the data. For example, it could also have been confined to the sediments, but in this case radial anisotropy of about 25% would be needed to fit the data. Because of this exceptionally large amplitude, we prefer a model with radial anisotropy confined to the upper crystalline crust.

In the middle crust (Figure 9b), relatively strong positive radial anisotropy with amplitudes ranging from 4% to 8% is observed across most of eastern Tibet, where the strongest anisotropy is concentrated near the northern margin of the Qiangtang terrane. Near the northern and eastern margins of the Tibetan Plateau, radial anisotropy decreases in amplitude. To the north, radial anisotropy decreases abruptly across the Kunlun fault, and to the east radial anisotropy decreases and becomes negative near the Longmenshan west of the Sichuan Basin. The northern margin of radial anisotropy closely follows the Kunlun fault. In contrast, the termination of radial anisotropy near the southeastern margin of Tibet does not follow the topography or geological boundaries. Strong radial anisotropy covers only the northern half of the Chuandian terrane and it ends before the plateau drops off and topography decreases. To the east of the Tibetan Plateau, negative radial anisotropy shows up near the Longmenshan, in a narrow strip between the Chuandian terrane and the Sichuan Basin. Outside the Tibetan Plateau, mid-crustal radial anisotropy is weak except within and south of the Sichuan Basin and in the Qilian terrane.

In the lower crust (Figure 9c), radial anisotropy is weak across most of the region of study, with notable isolated anomalies in the northern Songpan-Ganzi and Qiangtang terranes. In fact, radial anisotropy at this depth is not determined reliably because anisotropy trades off with both Moho depth and radial anisotropy in the uppermost mantle. This phenomenon is reflected in the large uncertainties shown in Figure 11c.

In Figure 9d, uppermost mantle anisotropy at 85 km depth is shown, which is taken from the model of *Shapiro and Ritzwoller* [2002], as mentioned in Section 3.1. Shapiro's model of anisotropy is fairly uniform across the study region with an average positive anisotropy of ~6%, but much weaker mantle anisotropy exists within and south of the Sichuan Basin. In fact, weak negative anisotropy exists beneath parts of the Sichuan Basin in their model.

The locations of the four vertical transects are shown in Figure 9a and the vertical transects themselves are presented in Figure 10. For profile A, Vsv, Vsh, and radial anisotropy are presented. For profiles B, C, and D, only radial anisotropy is presented.

For profile A, Vsv is similar to the result presented by *Yang et al.* [2012] using a similar data set. Within the high plateau, a Vsv minimum in the middle crust is seen clearly from about 20 to 40 km depth. In the Sichuan Basin, a very slow sedimentary layer is present along with faster lower crust. Compared to Vsv, Vsh is faster from the surface to the base of the crust except in the uppermost crust of the high plateau and the mid-crustal velocity minimum seen for Vsv is much more subtle. There are differences in upper crustal Vsv and Vsh in the Sichuan Basin as well. Radial anisotropy beneath the high plateau along profile A increases from an average of about -1% in the uppermost crust to values of 4% to 6% between 20 and 50 km depth. Radial anisotropy then decreases with depth in the lower crust. Near the eastern edge of the plateau, radial anisotropy vanishes as surface elevation falls off, perhaps changing sign before elevation plummets at the Longmenshan.

The three other vertical profiles shown in Figure 10 are similar to profile A in the vertical distribution of radial anisotropy in the crust across the Tibetan Plateau: radial anisotropy is negative, on average, in the uppermost crust, positive and peaks in amplitude in the middle crust, decreases in the lower crust, and terminates near the border of the high plateau except within and south of the Sichuan Basin. The nature of the termination of radial anisotropy near the border of the plateau varies from place to place. For example, in profile C, which runs across the northeastern part of the plateau, radial anisotropy decreases gradually as topography decreases. In contrast, in profile D, which goes through the southeastern part of the plateau, radial anisotropy ends abruptly before topography decreases.

In summary, within the Tibetan Plateau, strong positive radial anisotropy begins at about 20 km depth and peaks between 30 and 50 km depth. It is almost continuous between different terranes, but there is some diminishment in amplitude near terrane boundaries as profile B illustrates. Radial anisotropy has a somewhat broader depth range in the Qiangtang terrane compared with other terranes. Outside of the Tibetan plateau, strong upper-to-middle crustal radial anisotropy shows up in and south of the Sichuan Basin. Negative anisotropy is mostly confined to the uppermost crust beneath Tibet and in the middle crust in the Longmenshan region, near the border between Tibet and the Sichuan Basin.

4.4 Uncertainty in radial anisotropy

Figure 11 presents uncertainties in the estimated radial anisotropy in the region of study at depths of 10 and 35 km, as well in the lower crust at a depth of 90% of crustal thickness. The uncertainty is defined as one standard deviation of the posterior distribution at each depth. Except beneath the Sichuan Basin, uncertainties grow with depth in the crust because a smaller percentage of the observed dispersion curves are sensitive to the greater depths. Beneath the Sichuan Basin, the higher shallow uncertainties result from the trade-off of shear velocities in the crystalline crust and sediments. At 10 km depth, the average uncertainty in eastern Tibet is about 1%, whereas in the mid-crust it is about 2%, and in the lower crust it is about 3.5%. As discussed in Section 5.4.1, if we had not constrained Vsh=Vsv for crustal B-splines 1 and 5 (Figure 5) in the uppermost and lowermost crust, uncertainties in radial anisotropy in the uppermost and lowermost crust would have been larger. The higher uncertainties in the lower crust result from the fact that Love waves do not constrain Vsh well at these depths and there are trade-offs with crustal thickness and uppermost mantle structure and is why we concentrate discussion on shallower depths.

4.5 Computation of regional averages

Several of the attributes of the model observed here appear to be fairly homogeneous over extended areas. These attributes include positive mid-crustal radial anisotropy beneath eastern Tibet and the Sichuan Basin, negative mid-crustal radial anisotropy near the Longmenshan adjacent to the eastern border of Tibet, negative radial anisotropy in the shallow crust beneath parts of eastern Tibet (notably the Songpan-Ganzi terrane), and Vs in the mid-crust beneath eastern Tibet. We present here averages of the means and the standard deviations of the mean of these variables defined over the four regions. These standard deviations, in contrast with those presented in Figure 11 and discussed in Section 4.4, principally reflect spatial variations rather than uncertainties.

There are four regions over which we compute the averages. First, we consider "eastern Tibet" to be defined by the interior of the 84.2% probability contour (orange, red colors) of positive mid-crustal radial anisotropy near Tibet, which is presented later in the paper (Figure 13a). This contour approximately follows the outline of the high plateau. Second, we consider the Longmenshan region near the border between Tibet and the Sichuan Basin to be contained within the 15.8% probability contour (blue colors) of positive mid-crustal radial anisotropy (Figure 13a). Finally, we use the geological outlines of the Sichuan Basin and the Songpan-Ganzi terrane as the third and fourth regions.

In the Songpan-Ganzi terrane, the distribution of the means of shallow crustal (~10 km) radial anisotropy is presented in Figure 12a. The average of the means in this region is -1.03% ± 1.38%. This is the structural attribute with the relatively largest variability. The distribution of the means of mid-crustal radial anisotropy across eastern Tibet (~35 km) and the Sichuan Basin (~15 km) are presented in Figures 12b,c. Mid-crustal radial anisotropy averages 4.81% ± 1.41% in eastern Tibet. Across the Sichuan Basin the average is somewhat larger, 5.35% ± 1.43%. Also in the middle crust, but averaged over the Longmenshan region (~30 km), the distribution of the means of mid-crustal radial anisotropy is presented in Figure 12d. The average is -2.80% ± 0.94%. Finally, mid-crustal Vs averaged over eastern Tibet is 3.427 km/s ± 0.050 km/s, as seen in Figure 12e.

5. Identifying highly probable model attributes

The means of the posterior distributions of the models that result from the Bayesian Monte Carlo inversion of Rayleigh and Love wave dispersion curves have been used to infer that (1) positive (Vsh>Vsv) mid-crustal radial anisotropy exists across the entirety of eastern Tibet with an average amplitude (γ) of about 4.8% (~35 km) and at much shallower depths (~15 km) beneath the Sichuan Basin with an average amplitude of about 5.4%, (2) weaker negative radial anisotropy (Vsh<Vsv) appears in the middle crust (~30 km) along the Longmenshan region (-2.8%) and in the shallow crust (~10 km) across the Songpan-Ganzi terrane (-1.03%) , and (3) the Voigt averaged shear wave speed in the middle crust (~35 km) averages about 3.427 km/s across eastern Tibet. From the geographical spread of the local means of the posterior distributions of these attributes we have inferred that these observations are characteristic of each region. Radial anisotropy in the lowermost crust is more poorly constrained than at shallower depths because of a trade-off with crustal thickness and radial anisotropy in the mantle.

Although the mean of the posterior distribution is interpreted as its maximum likelihood, the Bayesian Monte Carlo inversion delivers a distribution of models at each depth. For this reason, within a Bayesian framework, the probability that the model achieves a particular attribute can be computed. Here we address the following questions across the region of study: (1) What is the probability that positive (Vsh>Vsv) radial anisotropy exists in the shallow crust or in the middle crust? (2) Similarly, what is the probability for negative radial anisotropy? (3) What is the probability that the Voigt averaged shear wave speed lies below or above 3.4 km/s in the middle crust?

In computing these probabilities, we acknowledge that the posterior distribution represents a conditional probability in which the likelihood is conditioned on prior information that appears in the range of the model variables allowed, the constraints imposed, the parameterization chosen, the details of the search algorithm, and the assumptions made (e.g., ρ/Vs, Vp/Vs, Q). From a Bayesian perspective, the distribution represents the authors' degree of belief in the results, but if the prior information is wrong then the resulting distribution of models may be biased. In Section 5.4, we identify several potential sources for bias and discuss how these choices may affect the mean of the estimated posterior distribution of the selected model attributes.

5.1 Computing the probability of a model attribute from the posterior distribution

Figure 13a,b illustrates the computation of the probability for the existence of positive radial anisotropy in the middle crust. The probability that Vsh > Vsv (positive radial anisotropy) at 35 km depth is mapped in Figure 13a. It is computed at each point from the local posterior distribution, examples of which are shown for locations A, B, and D from Figure 1a in Figure 13b. For point A, a location that we interpret as isotropic in the crust, approximately half (54%) of the posterior distribution shows positive anisotropy and half negative. For point B, which we interpret as possessing strong positive mid-crustal anisotropy, 100% of the posterior distribution has Vsh>Vsv at 35 km depth. For point D, where we observe negative anisotropy on average, only ~0.12% of the models in the posterior distribution have Vsh>Vsv. Thus, at this point, more than 99.8% of the models in the posterior distribution display negative anisotropy in the middle crust.

The values mapped in Figure 13a are simply the percentage of models in the posterior distribution at each point with positive mid-crustal radial anisotropy. Examples of the probability of positive radial anisotropy at depths of 10 and 15 km are also shown in Figure 13c,d. Similarly, from the local posterior distributions of the isotropic Vs, the probabilities that Vs is greater than 3.4 km/s or less than 3.4 km/s are mapped in Figure 14.

In general, we consider a model attribute (e.g., Vsh > Vsv, Vs < 3.4 km/s) to be “highly probable” if it appears in more than 97.8% of the models in the posterior distribution. In this case, all or nearly all of the models in the posterior distribution possess the specified attribute. If the attribute appears in less than 2.2% of the accepted models, then the converse of the attribute (e.g., Vsh < Vsv, Vs > 3.4 km/s) would be deemed “highly probable”. One could introduce other grades of probability (e.g., probable, improbable, the converse is probable, etc.), but we do not do so here.

5.2 Regions with high probability of positive or negative radial anisotropy

High probability regions for positive radial anisotropy in the middle crust appear as red colors in Figure 13a and for negative mid-crustal anisotropy as dark blue regions. Red colors cover most of eastern Tibet, including the Qiangtang terrane, most of the Songpan-Ganzi terrane, and the northern Chuandian terrane. Another region strongly favoring positive mid-crustal radial anisotropy lies south of the Sichuan Basin, largely in Yunnan province. Mid-crustal radial anisotropy has a lower average probability there (orange colors, Figure 13a) than beneath Tibet, because the crust is thinner (~40 km) and at 35 km depth crustal radial anisotropy trades-off with crustal thickness and uppermost mantle radial anisotropy. Blue colors appear in the Longmenshan region near the border of Tibet and the Sichuan Basin, indicating the high probability of negative mid-crustal radial anisotropy there.

At shallower depths, the high probability zones of positive or negative radial anisotropy are smaller and more variable than in the middle crust. At 10 km depth (Figure 13c), highly probable negative radial anisotropy is mainly confined to the Songpan-Ganzi terrane but also extends into parts of the Qiangtang and Chuandian terranes. By 15 km (Figure 13d), neither positive nor negative radial anisotropy attains high probabilities pervasively across Tibet, but positive radial anisotropy is highly probable across most of the Sichuan Basin.

5.3 Probability of low shear wave speeds in the middle crust

Middle-to-lower crustal low velocity zones (LVZ) have been reported in several studies [e.g., *Yao et al.*, 2008; *Yang et al.*, 2012], but most of these considered Vsv alone. The existence of crustal radial anisotropy with Vsh>Vsv across most of eastern Tibet increases the Voigt-averaged shear wave speed relative to Vsv, and reduces the strength of a crustal LVZ. *Yang et al.* [2012] argued that 3.4 km/s is a reasonable speed below which partial melt may plausibly begin to occur at a depth of about 35 km depth, although this threshold is poorly known and is probably spatially variable. Other values could also be used. At this depth, the mean value of the Voigt average shear wave speed in the posterior distribution is shown in Figure 8c and the distribution of the mean values across eastern Tibet is presented in Figure 12e. Although shear wave speeds across eastern Tibet average 3.427 km/s, there is substantial spatial variability and the likelihood that Vs dips below 3.4 km/s in some locations is high.

In the attempt to quantify the likelihood of shear wave speeds less than 3.4 km/s in the middle crust, Figure 14 presents the percentage of models in the posterior distribution at each point with Vs > 3.4 km/s and Vs < 3.4 km/s at 35 km depth. As Figure 14a shows, Vs > 3.4 km/s is highly probable across most of the study region, but does not rise to the level of high probability across much of Tibet. Conversely, Figure 14b shows that Vs < 3.4 km/s at this depth is also not highly probable across most of the high plateau. Unfortunately, this means that we cannot infer with high confidence either that mid-crustal Vs is greater than or less than 3.4 km/s across much of Tibet. However, there are two disconnected regions where more than 97.8% of the accepted model have Vs < 3.4 km/s, such that we would infer the high probability of Vs < 3.4 km/s. These regions are in the northern Songpan-Ganzi terrane near the Kunlun fault and in the northern Chuandian terrane. A third region of low Vs that nearly rises to the level of high probability lies in the northern Qiangtang terrane.

5.4 Caveats: Quantifying the potential for bias in the posterior distribution

Measurements of mid-crustal radial anisotropy, particularly its amplitude, and of shear wave speed Vs, particularly the minimum value it attains in the middle crust, are affected by a variety of information introduced in the inversion, including the parameterization of crustal radial anisotropy, crustal thickness in the reference model, the fixed amplitude of radial anisotropy in the mantle, the fixed value of the Vp/Vs ratio in the crust, and the fixed zero amplitude of Vp radial anisotropy and $\eta = 1$ in the crust. Errors in these assumptions could bias the posterior distribution and introduce a systematic error that may bias the probability estimates presented in Sections 5.1 to 5.3. We discuss here the effects of these assumptions and also discuss and then dismiss the possibility of overtones, particularly from Love waves, interfering with the estimation of radial anisotropy using fundamental modes.

5.4.1 Relaxing constraints on radial anisotropy in the uppermost and lowermost crust

All results presented above include the constraint that Vsh=Vsv for the crustal B-splines 1 and 5 (Figure 5). Figure 15 shows the range of the means of the posterior distributions for radial anisotropy averaged across the high plateau with this constraint applied (blue bars). This is compared with a similar spatial average computed without the constraint (red bars), so that the number of unknowns increases from 16 to 18. The less constrained inversion approximately encompasses the more tightly constrained result. The relaxation of the constraint on radial anisotropy increases the variability of the model, particularly in the uppermost and lowermost crust and shifts the mean of the distribution in the lowermost crust to larger values. Between depths of 25 and 45 km, however, the means of the distributions are nearly indistinguishable, implying that this constraint does not bias estimates of mid-crustal radial anisotropy.

5.4.2 Crustal thickness and mantle radial anisotropy

The crustal thickness in the reference model (around which the Monte Carlo search occurs) and the fixed amplitude of radial anisotropy in the mantle do affect aspects of the posterior distribution in the middle crust, including the amplitude of radial anisotropy and the isotropic shear wave speed. The effects of these properties of the deeper parts of the model will be stronger, however, where the crust is thinner. This is reflected in the uncertainties in mid-crustal radial anisotropy shown in Figure 11b. Uncertainties are smaller across eastern Tibet (~1.75%) where the crust is thicker than in adjacent regions outside Tibet (2.0-3.0%). Indeed, we find that changes in crustal thickness in the reference model and in the fixed amplitude of radial anisotropy in the mantle do not strongly and systematically affect either the amplitude of radial anisotropy or isotropic Vs in the middle crust beneath eastern Tibet. However, these changes do have a systematic impact on these model attributes where the crust is thinner, for example in the Longmenshan region near the border of Tibet and the Sichuan Basin. For this reason, we present results here of the impact of changing crustal thickness in the reference model and the amplitude of mantle radial anisotropy at location D (Figure 1a) in the Longmenshan region.

Figure 16a,b present the estimates of depth averaged (±5 km around the middle crust) mid-crustal radial anisotropy as well as depth averaged mid-crustal Vs, which result by changing the fixed amplitude of mantle radial anisotropy averaged from Moho to 150 km depth. Error bars reflect the one standard deviation variation in the posterior distribution in each of the inversions, which are performed identically to the inversions used to produce the model described earlier in the paper (which is the middle error bar with a triangle in the center in Figure 16a,b). The effect of mantle radial anisotropy on Vs is very weak but increasing mantle radial anisotropy does systematically reduce crustal radial anisotropy. Changing the depth-averaged mantle radial anisotropy from about 4% to 0% or 10% changes the estimated depth-averaged crustal radial anisotropy by less than ±1%, however. Because we believe that mantle radial anisotropy is probably known better than this range, this possible systematic shift in crustal radial anisotropy is probably an overestimate. Still, it lies within the stated errors of crustal radial anisotropy in the Longmenshan region. If potential systematic errors lie within stated uncertainties, we consider them not to be the cause for concern.

Similarly, Figure 16c,d present estimates of depth averaged (±5 km around the middle crust) mid-crustal radial anisotropy and depth averaged mid-crustal Vs caused by changing crustal thickness in the reference model. Again, the middle error bar is the result of the inversion for the model presented earlier in this paper, so that in the Longmenshan region the crustal thickness of the reference model was about 50 km. Changing the crustal thickness in the reference model (around which the Monte Carlo inversion searches) from 40 to 60 km has a systematic affect both on crustal radial anisotropy and mid-crustal isotropic Vs. But, again, the effect is relatively small (±0.5% in mid-crustal radial anisotropy, ±25 m/s in mid-crustal Vs). Although the range of crustal thickness considered is considerably larger than what we consider physically plausible for this location, the effect on model characteristics is below the stated model uncertainty.

Therefore, both mid-crustal Vs and the mid-crustal radial anisotropy are affected by the fixed amplitude of mantle radial anisotropy and the crustal thickness in the reference model, but the effects are below estimated model uncertainties and could only become significant if the effects were correlated and would add constructively. Although this is possible, in principle, it is unlikely to occur systematically across the region. Tighter constraints on crustal thickness and mantle radial anisotropy would result from the joint interpretation of receiver functions and longer period dispersion measurements from earthquakes. Uncertainties in these quantities, therefore, are expected to reduce over time, but we believe that these improvements will not change the results presented here appreciably.

5.4.3 Vp/Vs in the crust

The strongest and also the most troubling parameter that may produce a systematic error in estimates of radial anisotropy is crustal Vp/Vs, which has been fixed in the crust at Vp/Vs = 1.75, the value for a Poisson solid which is generally considered to be typical of continental crust [*Zandt and Ammon*, 1995; *Christensen*, 1996]. Although normal Vp/Vs (~1.75) has been widely observed across much of eastern Tibet [*Vergne et al.*, 2002; *Xu et al.*, 2007; *Wang et al.*, 2010; *Mechie et al.*, 2011, 2012; *Yue et al.*, 2012], very low crustal Vp/Vs values also have been observed in the northern Songpan-Ganzi terrane [*Jiang et al.*, 2006], and very high crustal Vp/Vs has been observed near the Kunlun fault [*Vergne et al.*, 2002], the eastern margin of the plateau [*Xu et al.*, 2007; *Wang et al.*, 2010], as well as parts of the Qiangtang terrane [*Yue et al.*, 2012]. Thus, the assumption of a uniform Vp/Vs across all of Tibet may be inappropriate.

To test the effect of the assumption that crustal Vp/Vs=1.75 on the amplitude of mid-crustal radial anisotropy, we have inverted with different crustal Vp/Vs ratios and have plotted the resulting depth-averaged mid-crustal radial anisotropies for point B (Figure 1a) in Figure 17a. We apply these tests at a point in eastern Tibet, in contrast with the tests presented in Section 5.4.2, which were for the Longmenshan region. Positive correlation is observed between the applied crustal Vp/Vs and depth-averaged radial anisotropy, and mid-crustal radial anisotropy may become zero when Vp/Vs drops below 1.60. This extremely low Vp/Vs could exist at depths where the Alpha-Beta quartz transition (ABQT) occurs, namely in a thin layer that occurs somewhere between 20 to 30 km depth [*Mechie et al.*, 2011]. Also, a relatively low crustal Vp/Vs may be caused by crust with a felsic composition [*Mechie et al.*, 2011]. However, both alternatives are for a thin low Vp/Vs layer, not the whole crust, and it is physically unlikely to have an average crustal

Vp/Vs of 1.60. With values of Vp/Vs ranging from 1.70 to 1.80, the effect is to change the amplitude of radial anisotropy only by about ±1%. Although radial anisotropy is required across eastern Tibet, the reliability of estimates of its amplitude would be improved with better information about Vp/Vs across Tibet.

The value of crustal Vp/Vs not only affects the amplitude of crustal radial anisotropy, but also the shear wave speed (Vs). Figure 17b shows that crustal Vp/Vs and depth averaged mid-crustal Vs are anti-correlated, with Vs decreasing as crustal Vp/Vs increases. This result may seem counterintuitive. With a fixed Vp/Vs, increasing radial anisotropy will increase Vs. In addition, increasing Vp/Vs tends to increase radial anisotropy. Nevertheless, increasing Vp/Vs in the inversion reduces the inferred Vs because increasing Vp at a constant Vs increases the Rayleigh wave speed but not the Love wave speed. In this case, Vsv must be lowered to reduce the Rayleigh wave speed in order to fit the Rayleigh-Love discrepancy. The lowering of Vsv (caused by increasing Vp/Vs) thus lowers Vs. For Vp/Vs running between the physically more plausible range of 1.7 to 1.8, the effect on mid-crustal Vs is well within stated uncertainties, about ±9 m/s.

5.4.4 Vp radial anisotropy and η in the crust

As discussed in Section 3.1, our inversions are performed with the simplifying but nonphysical assumption that the elastic tensor possesses only Vs anisotropy with $\gamma = (Vsh - Vsv)/Vs \neq 0$, but $Vph = Vpv$ so that Vp radial anisotropy $\varepsilon = (Vph - Vpv)/Vp = 0$ and $\eta = 1$. More realistically, however, Vp anisotropy is expected to accompany Vs anisotropy so that $\varepsilon \neq 0$ and $\eta \neq 1$. We discuss the effect of the imposition of this simplification on the posterior distribution of Vs anisotropy.

Figure 18 presents the sensitivity of Rayleigh and Love wave phase speeds at 30 sec period to perturbations in Vsv, Vsh, Vpv, Vph, and η at different depths. Love waves are sensitive almost exclusively to Vsh, being only weakly sensitive to Vsv and completely insensitive to Vph, Vpv, or η. In contrast, Rayleigh waves are sensitive to all of the parameters except Vsh. In order to determine the effect of Vp anisotropy (ε) and η on our estimate of Vs anisotropy (γ) we concentrate on the Rayleigh wave.

Vph and Vpv have opposite effects on Rayleigh wave phase speeds. Thus, increasing Vph or decreasing Vpv (i.e., increasing ε) will have a similar effect to decreasing Vsv (Figure 18a). For an isotropic medium, the opposite signs of the Vph and Vpv kernels cause them to cancel approximately in the deeper parts of the kernel and restrict isotropic Vp sensitivity to a zone much shallower than primary Vs sensitivity. But for an anisotropic medium this is not true. Anisotropic Vp sensitivity extends as deeply as anisotropic Vs sensitivity. An increase in Vp radial anisotropy will decrease the Rayleigh wave phase speed just like an increase in Vs radial anisotropy. Therefore, as *Anderson and Dziewonski* [1982] point out, the existence of Vp radial anisotropy will tend to decrease the Vs radial anisotropy needed to resolve the Rayleigh-Love discrepancy. However, the fifth modulus η must also be taken into account. As shown in Figure 18a, the sensitivity of Rayleigh wave phase speeds to η is similar to that of Vph so that a decrease in η will increase the Rayleigh wave phase speed, increasing the Vs radial anisotropy needed to resolve the Rayleigh-Love discrepancy. Thus, an increase (decrease) in Vp radial anisotropy and a decrease (increase) in η may compensate each other. Whether an increase in Vp radial anisotropy is expected to correlate with a reduction in η needs to be explored by investigating the elastic tensor of real crustal rock samples.

For many different crustal and mantle rocks, Vp radial anisotropy and η can be scaled approximately to Vs radial anisotropy [*Gung et al.*, 2003; *Becker et al.*, 2008; *Takeo et al.*, 2013]. To obtain approximate scaling relationships, we use the elastic tensors of three crustal rock samples measured by *Erdman et al*. [2013] and provided to us by B. Hacker. Following the procedure described by *Montagner and Anderson* [1989], we rotate the elastic tensors to all possible orientations and compute the five corresponding Love coefficients (A, C, F, L, and N) for every elastic tensor at each orientation. We then analyze the variation of Vp radial anisotropy (ε) and η as a function of Vs radial anisotropy (γ) over all orientations. This analysis shows that the relationship between Vp and Vs radial anisotropy is nonlinear, particularly for negative Vs radial anisotropy ($\gamma < 0$), and ε may be non-zero when γ goes to zero. However, ignoring the possible offset between ε and γ, for weak anisotropy a linear relationship between γ and ε fits the data adequately and we find: $\varepsilon \approx 0.5\ \gamma$. The relationship between η and Vs radial anisotropy is much more linear with an average slope of about -4.2, and the offset between η and γ is negligible. As a result, based on the elastic tensor data of *Erdman et al*. [2013] we obtain the following approximate linear scaling relationships between Vs anisotropy (γ) with Vp anisotropy (ε) and η:

$$\varepsilon \approx 0.5\ \gamma \qquad\qquad \eta \approx 1.0 - 4.2\ \gamma \qquad\qquad (5)$$

Thus, an increase in Vs radial anisotropy is correlated with a smaller increase in Vp radial anisotropy but a larger decrease in η.

With the scaling relationships summarized by equation (5), we re-perform the inversions at four geographical points (A-D of Figure 1a) and present the results in Figure 19. On the vertical axis of Figure 19a are the estimates of Vs radial anisotropy (γ) with the realistic elastic tensor in which Vp anisotropy and η are scaled to Vs anisotropy via equation (5). The horizontal axis presents the estimates of Vs radial anisotropy with the simplified elastic tensor in which all anisotropy is in Vs so that $\varepsilon=0$ and $\eta=1$. In each case the results represent a depth average of Vs anisotropy, which is performed over the upper crust for location C and over the middle crust at the other locations. As expected, the scaling of Vp anisotropy and η to Vs anisotropy has almost no effect at location A where the crust is nearly isotropic, but does have an effect at the locations where there is significant crustal Vs anisotropy. Both the positive (location B) and negative (location D) mid-crustal Vs anisotropy tend to increase in amplitude in the inversion based on the more realistic elastic tensor, which means that the amplitude of mid-crustal Vs anisotropy presented in Section 4 may be slightly underestimated. However, for all four locations, differences between estimates of Vs anisotropy with the simplified or realistic models of radial anisotropy are small, generally lying within the 1σ uncertainty because the effects of Vp radial anisotropy and η compensate on another.

5.4.5 Possibility of overtone interference?

Levshin et al. [2005] discussed how higher modes observed across Central Asia can be used to improve crustal models in this region. The potential existence of higher modes, however, could complicate observations of fundamental mode Rayleigh and Love waves. In the Sichuan Basin, based on our 3D model the fundamental and first overtone modes for Love wave should be well separated with a difference between them of at least 350 m/s for periods above 8 sec, which is much larger than the observed Rayleigh-Love discrepancy (Figure 7c). Therefore, overtones cannot interfere with fundamental mode Love wave measurements in the Sichuan Basin. However, in Tibet where the crust is much thicker, the fundamental mode and overtone Love waves are closer. Figure 20a presents Love wave group and phase speeds for the fundamental and first overtone modes computed based on our 3D model at a point in eastern Tibet (point B of Figure 1a). The group speed of the first Love overtone closely approaches (and can overlap at some locations) the fundamental group speed at about 15 sec period. Higher overtones will approach the fundamental mode group speed curves at successive shorter periods. It is, therefore, important to consider if Love wave overtones could be mistaken for the fundamental mode and potentially bias the Love wave phase speed measurements in the period band of our study (≥ 8 sec). The relevance of this consideration is amplified by recent observation of *Poli et al.* [2013] of Love wave overtones at periods below about 8 sec using ambient noise in the Baltic shield.

In contrast with the observations obtained by *Levshin et al.* [2005] based on intermediate and deep earthquakes in Central Asia, we do not see obvious overtones on FTAN diagrams of ambient noise cross-correlations in the region at periods above 6 sec. This does not mean that the overtones do not exist because they could be obscured by the fundamental modes. But, the determination of the likelihood of overtone interference reduces to a consideration of the relative excitation of the fundamental and overtone modes. Figure 20b presents theoretical source spectra computed from a horizontal force for the fundamental and first Love overtone modes for source depths of 0 and 20 km (computed at the same location as in Figure 20a). For the surface source, the fundamental mode has much higher amplitude than the first overtone at all periods. However, for a mid-crustal source depth, the fundamental and overtone mode have similar amplitudes only below about 8 sec period. Figure 20c-d illustrate these amplitudes by separately plotting the fundamental and first overtone Green's functions for a horizontal force. Figure 20e-f shows the FTAN diagrams for these two Green's functions. For the surface source, the overtone does not interfere with measurements of the fundamental mode group or phase speeds across the entire period band of the synthetic seismogram (2 – 45 sec). For the mid-crustal source, FTAN picks up the first overtone only at periods below ~6 sec and measures an unbiased fundamental mode at all longer periods. Similar results are found for force couples and double couples.

Although the physical cause of Love waves in ambient noise remains enigmatic, it is likely that they arise from processes near earth's surface. In this case the fundamental mode would probably be much stronger than the overtones and overtone interference in measuring fundamental mode Love wave group and phase speeds would probably be minimal at all periods. Even in the unlikely event that ambient noise Love waves were somehow generated at mid-crustal depths or there were some other means to de-amplify the fundamental relative to the overtone modes so that the relative amplitude of overtones and fundamental Love waves would be more commensurate, these synthetic results presented here show that the fundamental mode group and phase speeds can be measured accurately at periods above about 6 sec.

Rayleigh wave overtones have been observed quite robustly in ambient noise cross-correlations in ocean seismograph data [*Harmon et al*., 2007; *Yao et al*., 2011] and in basin resonances for waves coming on the continents [*Savage et al., 2013*] but only at periods below about 5 sec and for the basin resonances predominantly on the radial (non-vertical) component. They are also commonly observed at frequencies above 1 Hz in exploration settings [e.g., *Ritzwoller and Levshin, 2002*]. The period band of these observations does not intersect the current study and Rayleigh wave overtones are also an unlikely cause of interference with our observations of fundamental mode radial anisotropy.

In conclusion, although the arguments presented here are not definitive, it is highly unlikely that overtones have interfered significantly with the measurement of fundamental mode Love or Rayleigh wave dispersion in the period band of our observations.

5.4.6 Conclusions about potential bias in the posterior distributions

We have tested how systematic changes to prior information and constraints imposed in the inversion affect the key model attributes that are interpreted in the paper; namely, the amplitude of mid-crustal Vs radial anisotropy and mid-crustal Voigt-averaged isotropic Vs. In particular, we tested the effect of changing the fixed amplitude of radial anisotropy in the upper mantle, the crustal thickness in the reference model, the Vp:Vs ratio in the crust, and the Vp radial anisotropy and η in the crust. In general, we find that the mid-crustal radial anisotropy will become more positive (i.e., Vsh will increase relative to Vsv) by reducing mantle radial anisotropy, increasing crustal thickness, increasing crustal Vp/Vs, and introducing a more realistic elastic tensor in the crust. Because crustal Vp radial anisotropy is expected to be anticorrelated with η [*Erdman et al.*, 2013], we show that the introduction of Vp radial anisotropy with η allowed to differ from unity has the effect of slightly increasing the estimate of mid-crustal Vs radial anisotropy. Similarly, isotropic shear wave speed Vs also depends to a certain extent on these choices, being inclined to increase with increasing crustal thickness and with decreasing Vp/Vs. The tests demonstrate, however, that the inference of both positive and negative mid-crustal radial anisotropy is robust and potential bias caused by physically realistic variations in prior information imposed in the inversion should lie within the stated uncertainties of the key model attributes. In addition, we have argued that interference from Love wave (and Rayleigh wave) overtones is expected to affect estimates of crustal Vs anisotropy negligibly.

Improved constraints on crustal thickness and radial anisotropy in the mantle can be achieved by introducing receiver functions and longer period surface wave dispersion information from earthquake tomography, which are planned for the future. Vp radial anisotropy and η can be constrained better with improved knowledge of the petrologic composition of the Tibetan crust as more accurate scaling relationships between Vs anisotropy, Vp anisotropy and η are obtained. The observation of higher mode surface waves after earthquakes is another possible direction for improvements in the model. Providing improved constraints on crustal Vp/Vs may prove to be more challenging, however.

6. Discussion

Taking into account the estimated probabilities and the likelihood of bias discussed in Section 5 we now address two final questions: What is the most likely cause (or causes) of the radial anisotropy observed beneath and bordering eastern Tibet? Is there evidence for pervasive partial melt in the middle crust beneath eastern Tibet?

6.1 On the cause of positive and negative radial anisotropy

Four robust radially anisotropic features are observed. In the middle crust, positive radial anisotropy is observed beneath essentially all of (1) eastern Tibet and (2) the Sichuan Basin and (3) negative anisotropy is found beneath the Longmenshan region bordering eastern Tibet and the Sichuan Basin. (4) In the upper crust, negative radial anisotropy is observed beneath the Songpan-Ganzi terrane and parts of the Qiangtang and Chuandian terranes. We consider the cause of the mid-crustal observations first.

Earlier studies [*Shapiro et al.*, 2004; *Huang et al.*, 2010] have interpreted the observation of mid-crustal positive radial anisotropy beneath Tibet as evidence for the existence of anisotropic crustal minerals in the middle crust. Recent experimental results, however, have shown that continental crustal minerals such as quartz and feldspars act to dilute the anisotropic response of mica rich rocks [*Ward et al.*, 2012]. This dilution effect may raise doubt into whether crystallographic preferred orientation (CPO) of continental crustal minerals alone can cause strong mid-crustal anisotropy. Open or filled fractures [*Leary et al.*, 1990; *Crampin and Chastin*, 2003; *Figueiredo et al.*, 2013], grain-scale effects [*Hall et al.*, 2008], sedimentary layering [*Valcke et al.*, 2006], other microstructural parameters [*Wendt et al.*, 2003], and sills or lenses of partial melt [*Takeuchi et al.*, 1968; *Kawakatsu et al.*, 2009] have all been discussed as mechanisms to produce seismic anisotropy under certain conditions. Amongst these mechanisms, partial melt may provide the most viable alternative to CPO to produce mid-crustal radial anisotropy, The anisotropic effect of partial melt is less well understood and its ability to produce substantial radial anisotropy is more speculative than CPO. Thus, the observation of crustal radial anisotropy is still best seen as a mapping of the distribution of aligned crustal minerals – albeit with the caveat that the relative fractions of mica, feldspars, quartz, and amphibole remain poorly understood. In the middle crust we believe that the chief contributor to strong anisotropy is a sheet silicate such as mica (biotite, muscovite).

Even though individual mica crystals exhibit monoclinic symmetry, their tendency to form sheets causes them in aggregate to approximate the much simpler hexagonal symmetry [*Godfrey et al.*, 2000; *Cholach et al.*, 2005; *Cholach and Schmitt*, 2006; *Erdman et al*., 2013]. There is a unique symmetry axis in a hexagonal system and we call the plane that is perpendicular to this axis the foliation plane. The amplitude and sign of radial anisotropy reflect the orientation of the symmetry axis (or foliation plane) along with the intrinsic strength of anisotropy, which is determined by mineral content and extent of alignment. The amplitude of azimuthal anisotropy is also affected by the orientation of the symmetry axis [*Levin and Park*, 1997; *Frederiksen and Bostock*, 2000]. Dipping or tilted symmetry axes are believed to be common in many geological settings [*Okaya and McEvilly*, 2003] and should produce a combination of radial and azimuthal anisotropy.

Figure 21 clarifies these expectations by rotating the elastic tensors measured from three crustal rock samples obtained at the Funeral Mountains, the East Humboldt Range, and the Ruby Mountains by *Erdman et al.* [2013] (and supplied by B. Hacker) through a set of orientations where the symmetry axis ranges from vertical ($\theta = 0°$, transverse isotropy) to horizontal ($\theta = 90°$). Similarly, the foliation plane ranges from horizontal to vertical. The result of this calculation is presented in Figure 21b and yields four general conclusions. Radial anisotropy (1) is positive (Vsh>Vsv) and its magnitude maximizes for a vertical symmetry axis ($\theta = 0°$), (2) falls to zero at an intermediate angle ~50^{o}, (3) becomes negative as the symmetry axis exceeds ~50^{o}, and (4) has its maximum negative magnitude between 60°-90° which is less than the maximum positive magnitude. Therefore, the observed amplitude of radial anisotropy is controlled by a combination of the intrinsic strength of anisotropy, which results from the density of anisotropic minerals and the constructive interference of their effects, and the angle that the symmetry axis makes relative to the local vertical direction. The observation of weaker radial anisotropy alone cannot be interpreted as evidence for a lower density of anisotropic minerals. However, the observation of strong radial anisotropy is evidence for the existence of anisotropic minerals aligned consistently to produce a substantial anisotropic effect. In addition, positive radial anisotropy indicates that the foliation plane is subhorizontal ($\theta <$ 10°) to shallowly dipping (10°-30°) and negative radial anisotropy implies that it is steeply dipping (60°-80°) to subvertical (80°-90°). Because the maximum negative amplitude of radial anisotropy is smaller than the maximum positive amplitude, negative anisotropy is a more difficult observation.

Based on these considerations, we conclude that the observations of positive mid-crustal radial anisotropy beneath eastern Tibet and beneath the Sichuan Basin imply the existence of planar mica sheets in the middle crust oriented systematically such that the foliation planes are shallowly dipping. We believe that the symmetry axes are not vertical because crustal azimuthal anisotropy is observed across Tibet [e.g., *Yao et al.,* 2010; *Xie et al.,* 2012]. Similarly, the observation of negative mid-crustal radial anisotropy along the Longmenshan region is taken as evidence for planar mica sheets oriented systematically such that the foliation plane is steeply dipping or subvertical. The orientation of the foliation plane (or symmetry axis) cannot be constrained accurately in the absence of information about azimuthal anisotropy, however.

The orientations of the mica sheets in the middle crust probably have dynamical causes. Other than to note that the micas probably orient in response to ductile deformation in the middle crust, we do not speculate on the nature of the deformation that produces this orientation. We do note that the dip angle of faults in the Longmenshan region between Tibet and the Sichuan Basin is high [*Chen and Wilson*, 1996] and that the 2008 Wenchuan earthquake ruptured a steep fault [*Zhang et al.*, 2010]. The change in orientation of the mid-crustal foliation plane from shallowly dipping in eastern Tibet to steeply dipping or subvertical in the Longmenshan region may result from the resistance force applied by the rigid lithosphere underlying the Sichuan Basin.

The negative anisotropy observed in the shallow crust (~10 km) across the Songpan-Ganzi terrane and some other parts of eastern Tibet may also result from the CPO of shallower micaceous rocks. However, earthquakes occur to a depth of about 15-20 km within Tibet [*Zhang et al.*, 2010; *Sloan et al.*, 2011], so the crust near 10 km depth where negative anisotropy is observed probably undergoes brittle deformation. Faults and cracks in the upper crust are associated with azimuthal anisotropy [*Sherrington et al.*, 2004] and may also cause radial anisotropy. Negative anisotropy would result from the plane of cracks or faults having a substantial vertical component. We believe this is the most likely source of the observations of negative radial anisotropy in the shallow crust beneath parts of eastern Tibet, particularly the Songpan-Ganzi terrane.

6.2 Existence of pervasive partial melt in the middle crust beneath Tibet?

Even under ideal observational circumstances in which Vs would be exceptionally well constrained, it is difficult to interpret Vs in terms of the likelihood of partial melt. Consistent with the analysis of *Caldwell et al.* [2009], *Yang et al.* [2012] present a plausibility argument for partial melt setting on below about 3.4 km/s, but this threshold is exceptionally poorly determined and would be expected to vary as a function of crustal composition, wet or dry conditions, and anelastic Q. The average of the means of the posterior distributions of mid-crustal shear wave speed taken across eastern Tibet is about 3.427 $\pm$ 0.050 km/s. Thus, using the 3.4 km/s threshold value, the mean value of shear wave speed challenges the existence of pervasive mid-crustal partial melts across the entirety of eastern Tibet. There are, however, several discrete regions that prefer particularly low mid-crustal Vs. Figure 14b identifies the regions in which the inference that Vs < 3.4 km/s is highly probable (or nearly so): the northern Songpan-Ganzi terrane, the northern Chuandian terrane, and part of the central-to-northern Qiangtang terrane. Most of these regions are coincident with high conductance areas from MT studies [*Wei et al.*, 2001; *Bai et al.*, 2010]. The INDEPTH MT profile [*Wei et al.*, 2001; *Unsworth et al.*, 2004] displays a conductive zone starting at about 25 km depth in the central Qiangtang terrane, and the conductor deepens both northward and southward. In the north Chuandian terrane, *Bai et al.* [2010] also observe a high conductive zone that begins at about 25 km depth.

Therefore, determining with certainty whether Vs lies either above or below 3.4 km/s is difficult using surface wave data alone. But, in summary, there is not compelling evidence that Vs is less than 3.4 km/s pervasively across all of eastern Tibet, although such low shear wave speeds are highly probable in three disjoint regions across the high plateau. Thus, assuming that Vs = 3.4 km/s is an appropriate proxy for the onset of partial melting, we would not expect partial melt to be a pervasive feature of eastern Tibet except in three disjoint regions (the northern Songpan-Ganzi terrane, the northern Chuandian terrane, and part of the central-to-northern Qiangtang terrane) where it should considered more probable. But this inference is highly uncertain due to the uncertainty of the threshold speed at which partial melt is likely to set on.

7. Conclusions

Based on Rayleigh (8 to 65 sec period) and Love (8 to 44 sec period) wave tomography using seismic ambient noise, we mapped phase velocities across eastern Tibet and surrounding regions using data recorded at PASSCAL and CEArray stations. A Bayesian Monte Carlo inversion method was applied to generate posterior distributions of the 3-D variation of Vsv and Vsh in the crust and uppermost mantle. Summarizing these distributions with their means and standard deviations at each depth and location, we showed that significant mid-crustal positive radial anisotropy (Vsh > Vsv) is observed across all of eastern Tibet with a spatially averaged amplitude of 4.8% $\pm$ 1.4% and terminates abruptly near the border of the high plateau. Weaker (-1.0% $\pm$ 1.4%) negative radial anisotropy (Vsh < Vsv) is observed in the shallow crust beneath the Songpan-Ganzi terrane and in the middle crust (-2.8% $\pm$ 0.9%) near the border of the Tibetan plateau and the Sichuan Basin. Positive mid-crustal radial anisotropy (5.4% $\pm$ 1.4%) is observed beneath the Sichuan Basin. Shear wave speed in the middle crust is 3.427 $\pm$ 0.050 km/s averaged across eastern Tibet.

We also queried the posterior distributions to determine which structural attributes are highly probable and showed the following. (1) Positive mid-crustal radial anisotropy is highly probable beneath the eastern high plateau. Lower crustal radial anisotropy is determined more poorly than anisotropy in the middle crust. (2) Isotropic shear wave speeds below 3.4 km/s are possible across most of the high plateau, but are highly probable only beneath the northern Songpan-Ganzi, the northern Chuandian, and part of the Qiangtang terranes. (3) The crustal Vp/Vs ratio is a parameter that is fixed in the inversion, and we set it in the crystalline crust to that of a Poisson solid: Vp/Vs = 1.75. If a lower (higher) value were chosen, then the amplitude of radial anisotropy would have decreased (increased) and mid-crustal Vs would have gone up (down). Vertically averaged crustal Vp/Vs below 1.7 or above 1.8, however, would be hard to justify over large areas of Tibet and if crustal Vp/Vs ranges between these values the resulting change to radial anisotropy falls within estimated uncertainties.

A piece of evidence for partial melt in the middle crust would be shear wave speeds at 35 km depth less than about 3.4 km/s [*Yang et al.*, 2012]. Although the maximum likelihood shear wave speed across Tibet at this depth is 3.43 km/s, Vs below 3.4 km/s cannot be formally ruled out particularly if the crystalline crustal Vp/Vs value is above 1.8. Such high values of Vp/Vs are characteristic of mafic mineralogy or partial melt, which are unlikely to extend vertically across the entire Tibetan crust, at least systematically over large areas. Therefore, in light of the uncertainty in the inference of partial melt from shear waves speeds, we do not find incontrovertible evidence for mid-crustal partial melt existing pervasively across all of eastern Tibet. However, we do conclude that partial melt is most likely to exist in several discrete regions, notably the northern Songpan-Ganzi, the northern Chuandian, and part of the Qiangtang terranes, where Vs < 3.4 km/s at 35 km depth is highly probable.

We interpret observations of positive mid-crustal radial anisotropy beneath eastern Tibet and beneath the Sichuan Basin as evidence for planar mica sheets in the middle crust oriented systematically such that their foliation planes are shallowly dipping (10°-30° from horizontal) on average. Similarly, the observation of negative mid-crustal radial anisotropy in the Longmenshan region along the border separating Tibet from the Sichuan Basin is taken as evidence for planar mica sheets oriented systematically such that their foliation planes are steeply dipping (60°-80°) or subvertical (80°-90°). We do not speculate on the nature of the deformation that produces this orientation of the mica sheets, but do argue that the change in orientation of the mid-crustal foliation plane near the eastern boundary of Tibet from shallowly dipping to steeply dipping or subvertical may result from the resistance force applied by the rigid lithosphere underlying the Sichuan Basin. Finally, the negative anisotropy observed in the shallow crust beneath the Songpan-Ganzi terrane and some other parts of eastern Tibet may be caused by faults and cracks in the upper crust that have a substantial vertical component.

Some of the uncertainty in the estimates of radial anisotropy and in Voigt-averaged shear wave speed Vs results from poor knowledge of the Vp/Vs ratio in the crystalline crust, of the crustal Vp radial anisotropy and η, of crustal thickness, and of radial anisotropy in the uppermost mantle. Future improvements in estimates of crustal radial anisotropy and Vs will depend on developing improved constraints on these structures. Earthquake surface wave tomography would improve knowledge of radial anisotropy in the mantle and in the lowermost crust. Receiver functions can be used to improve constraints on crustal thickness and perhaps also to provide information about the average Vp/Vs across the crust. Continued improvement in petrologic information about the the anisotropy of crustal rocks will provide tighter constraints on the scaling between Vp radial anisotropy, η, and Vs radial anisotropy.

Acknowledgments. The authors thank two anonymous reviewers and the Associate Editor for insightful comments that helped to improve this paper. They are particularly grateful to Peter Molnar and Anatoli Levshin for advice and support. They also thank Don Anderson, Misha Barmin, Bradley Hacker, David Okaya and Kevin Mahan for valuable conversations and information as well as the PIs and team members of the PASSCAL experiments, including the Hi-CLIMB, Namche Barwa, MIT-CHINA, Western Tibet, ASCENT/INDEPTH IV experiments, as well as staff members from the PASSCAL Instrument Center for collecting exceptionally valuable data in Tibet. The waveform data from the Chinese stations were provided by the Data Management Centre of the China National Seismic Network at the Institute of Geophysics, China Earthquake Administration. In addition, the facilities of the IRIS Data Management System were used to access some of the data used in this study. The IRIS DMS is funded through the US National Science Foundation under Cooperative Agreement EAR-0552316. This work was supported by US NSF-EAR award 0944022 and also was supported by a Macquarie University Start-up Grant and New Staff Grant to Y. Yang. Aspects of this research also were supported by Chinese Academy of Sciences open grant SKLGED2013-5-1-EZ at the University of Colorado at Boulder.

References:

Acton, C. E., K. Priestley, V. K. Gaur, and S. S. Rai (2010), Group velocity tomography of the Indo-Eurasian collision zone, *Journal of Geophysical Research: Solid Earth*, *115*(B12), B12335, doi:10.1029/2009JB007021.

Aki, K. and K. Kaminuma (1963), Phase velocity of Love waves in Japan, 1, Love wave from the Aleutian shock of March 9, 1957, *Bull. Earthquake Res. Inst. Univ. Tokyo*, 41, 243-260.

Aki, K. (1964), Study of Love and Rayleigh waves from earthquakes with fault plane solutions or with known faulting Part 2. Application of the phase difference method, *Bulletin of the Seismological Society of America*, *54*(2), 529–558.

Anderson, D. L., & Dziewonski, A. M. (1982), Upper mantle anisotropy: evidence from free oscillations, *Geophysical Journal of the Royal Astronomical Society*, *69*, 383–404.

Babuška, V. and M. Cara (1991), *Seismic Anisotropy in the Earth*, Modern approaches in geophysics v. 10, Kluwer Academic Publishers, Dordrecht, The Netherlands ; Boston.

Babuška, V., J.-P. Montagner, J. Plomerová, and N. Girardin (1998), Age-dependent Large-scale Fabric of the Mantle Lithosphere as Derived from Surface-wave Velocity Anisotropy, *Pure appl. geophys.*, *151*(2-4), 257–280, doi:10.1007/s000240050114.

Bai, D. et al. (2010), Crustal deformation of the eastern Tibetan plateau revealed by magnetotelluric imaging, *Nature Geoscience*, *3*(5), 358–362, doi:10.1038/ngeo830.

Barberini, V., L. Burlini, and A. Zappone (2007), Elastic properties, fabric and seismic anisotropy of amphibolites and their contribution to the lower crust reflectivity, *Tectonophysics*, *445*(3–4), 227–244, doi:10.1016/j.tecto.2007.08.017.

Barmin, M. P., M. H. Ritzwoller, and A. L. Levshin (2001), A fast and reliable method for surface wave tomography, *Pure and Applied Geophysics*, *158*(8), 1351–1375, doi:10.1007/PL00001225.

Barruol, G., and D. Mainprice (1993), 3-D seismic velocities calculated from lattice-preferred orientation and reflectivity of a lower crustal section: examples of the Val Sesia section (Ivrea zone, northern Italy), *Geophysical Journal International*, *115*(3), 1169–1188, doi:10.1111/j.1365-246X.1993.tb01519.x.

Becker, T., B. Kustowski, and G. Ekström (2008), Radial seismic anisotropy as a constraint for upper mantle rheology, *Earth Planet. Sci. Lett.*, *267*, 213–227.

Bensen, G. D., M. H. Ritzwoller, M. P. Barmin, A. L. Levshin, F. Lin, M. P. Moschetti, N. M. Shapiro, and Y. Yang (2007), Processing seismic ambient noise data to obtain reliable broad-band surface wave dispersion measurements, *Geophysical Journal International*, *169*(3), 1239–1260, doi:10.1111/j.1365-246X.2007.03374.x.

Bensen, G. D., M. H. Ritzwoller, and Y. Yang (2009), A 3-D shear velocity model of the crust and uppermost mantle beneath the United States from ambient seismic noise, *Geophysical Journal International*, *177*(3), 1177–1196, doi:10.1111/j.1365-246X.2009.04125.x.

Brocher, T. M. (2005), Empirical relations between elastic wavespeeds and density in the Earth's crust, *Bulletin of the Seismological Society of America*, *95*(6), 2081–2092, doi:10.1785/0120050077.

Caldwell, W. B., S. L. Klemperer, S. S. Rai, and J. F. Lawrence (2009), Partial melt in the upper-middle crust of the northwest Himalaya revealed by Rayleigh wave dispersion, *Tectonophysics*, *477*(1–2), 58–65, doi:10.1016/j.tecto.2009.01.013.

Champion, M.E, N.J. White, S.M. Jones, and K.F. Priestley (2006), Crustal velocity structure in the British Isles: a comparison of receiver functions and wide-angle seismic data, *Geophys. J. Int.,* 166, 795-813.

Chen, S. F., and C. J. L. Wilson (1996), Emplacement of the Longmen Shan Thrust—Nappe Belt along the eastern margin of the Tibetan Plateau, *Journal of Structural Geology*, *18*(4), 413–430, doi:10.1016/0191-8141(95)00096-V.

Chen, Y., J. Badal, and J. Hu (2010), Love and Rayleigh Wave Tomography of the Qinghai-Tibet Plateau and Surrounding Areas, *Pure Appl. Geophys.*, *167*(10), 1171–1203, doi:10.1007/s00024-009-0040-1.

Cholach, P. Y., and D. R. Schmitt (2006), Intrinsic elasticity of a textured transversely isotropic muscovite aggregate: Comparisons to the seismic anisotropy of schists and shales, *Journal of Geophysical Research: Solid Earth*, *111*(B9), 410–427, doi:10.1029/2005JB004158.

Cholach, P. Y., J. B. Molyneux, and D. R. Schmitt (2005), Flin Flon Belt seismic anisotropy: elastic symmetry, heterogeneity, and shear-wave splitting, *Canadian Journal of Earth Sciences*, *42*(4), 533–554.

Christensen, N. I. (1996), Poisson's ratio and crustal seismology, *J. Geophys. Res.*, *101*(B2), 3139–3156, doi:10.1029/95JB03446.

Christensen, N. I., and W. D. Mooney (1995), Seismic velocity structure and composition of the continental crust: A global view, *Journal of Geophysical Research: Solid Earth*, *100*(B6), 9761–9788, doi:10.1029/95JB00259.

Cotte, N., H. Pedersen, M. Campillo, J. Mars, J. F. Ni, R. Kind, E. Sandvol, and W. Zhao (1999), Determination of the crustal structure in southern Tibet by dispersion and amplitude analysis of Rayleigh waves, *Geophysical Journal International*, *138*(3), 809–819, doi:10.1046/j.1365-246x.1999.00927.x.

Crampin, S., and S. Chastin (2003), A review of shear wave splitting in the crack-critical crust, *Geophysical Journal International*, *155*(1), 221–240, doi:10.1046/j.1365-246X.2003.02037.x.

Duret, F., N. M. Shapiro, Z. Cao, V. Levin, P. Molnar, and S. Roecker (2010), Surface wave dispersion across Tibet: Direct evidence for radial anisotropy in the crust, *Geophys. Res. Lett.*, *37*(16), L16306, doi:10.1029/2010GL043811.

Erdman, M., B. Hacker, G. Zandt, and G. Seward (2013), Seismic anisotropy of the crust: Electron backscatter diffraction measurements from the Basin and Range, *Geophys. J. Int.*, in press.

Ekström, G., and A. M. Dziewonski (1998), The unique anisotropy of the Pacific upper mantle, *Nature*, *394*(6689), 168–172, doi:10.1038/28148.

Figueiredo, J. J. S. de, J. Schleicher, R. R. Stewart, N. Dayur, B. Omoboya, R. Wiley, and A. William (2013), Shear wave anisotropy from aligned inclusions: ultrasonic frequency dependence of velocity and attenuation, *Geophys. J. Int.*, doi:10.1093/gji/ggs130. [online] Available from: http://gji.oxfordjournals.org/content/early/2013/02/05/gji.ggs130 (Accessed 14 February 2013)

Frederiksen, A. W., and M. G. Bostock (2000), Modelling teleseismic waves in dipping anisotropic structures, *Geophysical Journal International*, *141*(2), 401–412, doi:10.1046/j.1365-246x.2000.00090.x.

Godfrey, N. J., N. I. Christensen, and D. A. Okaya (2000), Anisotropy of schists: Contribution of crustal anisotropy to active source seismic experiments and shear wave splitting observations, *Journal of Geophysical Research: Solid Earth*, *105*(B12), 27991–28007, doi:10.1029/2000JB900286.

Gung, Y., M. Panning, and B. Romanowicz (2003), Global anisotropy and the thickness of continents, *Nature*, *422*(6933), 707–711, doi:10.1038/nature01559.

Guo, Z., X. Gao, H. Yao, J. Li, and W. Wang (2009), Midcrustal low-velocity layer beneath the central Himalaya and southern Tibet revealed by ambient noise array tomography, *Geochemistry, Geophysics, Geosystems*, *10*(5), Q05007, doi:10.1029/2009GC002458.

Hall, S. A., J.-M. Kendall, J. Maddock, and Q. Fisher (2008), Crack density tensor inversion for analysis of changes in rock frame architecture, *Geophysical Journal International*, *173*(2), 577–592, doi:10.1111/j.1365-246X.2008.03748.x.

Harmon, N., Forsyth, D., & Webb, S. (2007), Using ambient seismic noise to determine short-period phase velocities and shallow shear velocities in young oceanic lithosphere, *Bulletin of the Seismological Society of America*, *97*(6), 2009–2023. doi:10.1785/0120070050.

Huang, H., H. Yao, and R. D. van der Hilst (2010), Radial anisotropy in the crust of SE Tibet and SW China from ambient noise interferometry, *Geophys. Res. Lett.*, *37*, 5 PP., doi:201010.1029/2010GL044981.

James, M. and M. Ritzwoller (1999), Feasibility of truncated perturbation expansions to approximate Rayleigh-wave eigenfrequencies and eigenfunctions in heterogeneous media, *Bull. Seismol. Soc. Amer., 89*(2), 433-441.

Jiang, M., A. Galve, A. Hirn, B. de Voogd, M. Laigle, H. P. Su, J. Diaz, J. C. Lepine, and Y. X. Wang (2006), Crustal thickening and variations in architecture from the Qaidam basin to the Qang Tang (North-Central Tibetan Plateau) from wide-angle reflection seismology, *Tectonophysics*, *412*(3-4), 121–140, doi:10.1016/j.tecto.2005.09.011.

Jiang, M., S. Zhou, E. Sandvol, X. Chen, X. Liang, Y. J. Chen, and W. Fan (2011), 3-D lithospheric structure beneath southern Tibet from Rayleigh-wave tomography with a 2-D seismic array, *Geophysical Journal International*, *185*(2), 593–608, doi:10.1111/j.1365-246X.2011.04979.x.

Kanamori, H., and D. L. Anderson (1977), Importance of physical dispersion in surface wave and free oscillation problems: Review, *Reviews of Geophysics*, *15*(1), 105–112, doi:10.1029/RG015i001p00105.

Karato, S. (1993), Importance of anelasticity in the interpretation of seismic tomography, *Geophysical Research Letters*, *20*(15), 1623–1626, doi:10.1029/93GL01767.

Kawakatsu, H., P. Kumar, Y. Takei, M. Shinohara, T. Kanazawa, E. Araki, and K. Suyehiro (2009), Seismic evidence for sharp lithosphere-asthenosphere boundaries of oceanic plates, *Science*, *324*(5926), 499–502, doi:10.1126/science.1169499.

Kennett, B. L. N., E. R. Engdahl, and R. Buland (1995), Constraints on seismic velocities in the Earth from traveltimes, *Geophysical Journal International*, *122*(1), 108–124, doi:10.1111/j.1365-246X.1995.tb03540.x.

Kitamura, K. (2006), Constraint of lattice-preferred orientation (LPO) on Vp anisotropy of amphibole-rich rocks, *Geophysical Journal International*, *165*(3), 1058–1065, doi:10.1111/j.1365-246X.2006.02961.x.

Laske, G. and G. Masters (1997), A global digital map of sediment thickness, EOS Trans. AGU, 78, F483.

Leary, P. C., S. Crampin, and T. V. McEvilly (1990), Seismic fracture anisotropy in the Earth's crust: An overview, *Journal of Geophysical Research: Solid Earth*, *95*(B7), 11105–11114, doi:10.1029/JB095iB07p11105.

Levin, V., and J. Park (1997), P-SH conversions in a flat-layered medium with anisotropy of arbitrary orientation, *Geophysical Journal International*, *131*(2), 253–266, doi:10.1111/j.1365-246X.1997.tb01220.x.

Levshin, A.L. and M.H. Ritzwoller (2001), Automated detection, extraction, and measurement of regional surface waves, *Pure Appl Geophys*, 158(8), 1531 - 1545.

Levshin, A. L., M. H. Ritzwoller, and L. I. Ratnikova (1994), The nature and cause of polarization anomalies of surface waves crossing northern and central Eurasia, *Geophysical Journal International*, *117*(3), 577–590, doi:10.1111/j.1365-246X.1994.tb02455.x.

Levshin, A. L., M. H. Ritzwoller, and N. M. Shapiro (2005), The use of crustal higher modes to constrain crustal structure across Central Asia, *Geophysical Journal International*, *160*(3), 961–972, doi:10.1111/j.1365-246X.2005.02535.x.

Levshin, A. L., X. Yang, M. P. Barmin, and M. H. Ritzwoller (2010), Midperiod Rayleigh wave attenuation model for Asia, *Geochemistry, Geophysics, Geosystems*, *11*(8), Q08017, doi:10.1029/2010GC003164.

Li, H., W. Su, C.-Y. Wang, and Z. Huang (2009), Ambient noise Rayleigh wave tomography in western Sichuan and eastern Tibet, *Earth and Planetary Science Letters*, *282*(1–4), 201–211, doi:10.1016/j.epsl.2009.03.021.

Lin, F.-C., M. P. Moschetti, and M. H. Ritzwoller (2008), Surface wave tomography of the western United States from ambient seismic noise: Rayleigh and Love wave phase velocity maps, *Geophysical Journal International*, *173*(1), 281–298, doi:10.1111/j.1365-246X.2008.03720.x.

Lin, F.-C., M. H. Ritzwoller, and R. Snieder (2009), Eikonal tomography: surface wave tomography by phase front tracking across a regional broad-band seismic array, *Geophysical Journal International*, *177*(3), 1091–1110, doi:10.1111/j.1365-246X.2009.04105.x.

Lin, F.C., M.H. Ritzwoller, Y. Yang, M.P. Moschetti, and M.J. Fouch (2011), Complex and variable crustal and uppermost mantle seismic anisotropy in the western United States , *Nature Geoscience*, Vol 4, Issue 1, 55-61.

Lloyd, G. E., R. W. H. Butler, M. Casey, and D. Mainprice (2009), Mica, deformation fabrics and the seismic properties of the continental crust, *Earth and Planetary Science Letters*, *288*(1–2), 320–328, doi:10.1016/j.epsl.2009.09.035.

Maceira, M., S. R. Taylor, C. J. Ammon, X. Yang, and A. A. Velasco (2005), High-resolution Rayleigh wave slowness tomography of central Asia, *Journal of*

Geophysical Research: Solid Earth, *110*(B6), B06304, doi:10.1029/2004JB003429.

Mahan, K. (2006), Retrograde mica in deep crustal granulites: Implications for crustal seismic anisotropy, *Geophys. Res. Lett.*, *33*(24), L24301, doi:10.1029/2006GL028130.

Mainprice, D. (2007), Seismic anisotropy of the deep Earth from a mineral and rock physics perspective, in *Treatise in Geophysics*, 2, 437-492, Schubert, G., ed. Elsevier, Oxford.

Masters, G., M. P. Barmine, and S. Kientz (2007), Mineos user's manual, in Computational Infrastructure for Geodynamics, Calif. Inst. of Technol., Pasadena

McEvilly, T. V. (1964), Central U.S. crust—Upper mantle structure from Love and Rayleigh wave phase velocity inversion, *Bulletin of the Seismological Society of America*, 54(6A), 1997–2015.

Mechie, J., R. Kind, and J. Saul (2011), The seismological structure of the Tibetan Plateau crust and mantle down to 700 km depth, *Geological Society, London, Special Publications*, *353*(1), 109–125, doi:10.1144/SP353.7.

Mechie, J. et al. (2012), Crustal shear (S) velocity and Poisson's ratio structure along the INDEPTH IV profile in northeast Tibet as derived from wide-angle seismic data, *Geophysical Journal International*, *191*(2), 369–384, doi:10.1111/j.1365-246X.2012.05616.x.

Montagner, J.-P. and H.-C. Nataf (1986), A simple method for inverting the azimuthal anisotropy of surface waves, *J. Geophys. Res.,* 91, B1, 511-520.

Montagner, J.-P., and D. L. Anderson (1989), Petrological constraints on seismic anisotropy, *Phys. Earth Planet. Inter.*, *54*(1–2), 82–105, doi:10.1016/0031-9201(89)90189-1.

Montagner, J.-P., and T. Tanimoto (1991), Global upper mantle tomography of seismic velocities and anisotropies, *Journal of Geophysical Research: Solid Earth*, *96*(B12), 20337–20351, doi:10.1029/91JB01890.

Moschetti, M. P., and M. H. R., F.-C. Lin, and Y. Yang (2010a), Crustal shear wave velocity structure of the western United States inferred from ambient seismic noise and earthquake data, *J. Geophys. Res.*, *115*, 20 PP., doi:2010 10.1029/2010JB007448.

Moschetti, M. P., M. H. Ritzwoller, F. Lin, and Y. Yang (2010b), Seismic evidence for widespread western-US deep-crustal deformation caused by extension, *Nature*, *464*(7290), 885–889, doi:10.1038/nature08951.

Nettles, M., and A. M. Dziewoński (2008), Radially anisotropic shear velocity structure of the upper mantle globally and beneath North America, *J. Geophys. Res.*, *113*, 27 PP., doi:200810.1029/2006JB004819.

Nishizawa, O., and T. Yoshino (2001), Seismic velocity anisotropy in mica-rich rocks: an inclusion model, *Geophysical Journal International*, *145*(1), 19–32, doi:10.1111/j.1365-246X.2001.00331.x.

Okaya, D. A., and T. V. McEvilly (2003), Elastic wave propagation in anisotropic crustal material possessing arbitrary internal tilt, *Geophysical Journal International*, *153*(2), 344–358, doi:10.1046/j.1365-246X.2003.01896.x.

Okaya, D.A., N. Christensen, D. Stanley, and T. Stern (1995), Crustal anisotropy in the vicinity of the Alpine Fault Zone, South Island, N.Z*., J. Geol. Geophys.,* 38, 579-583.

Ozacar, A.A. and G. Zandt (2004), Crustal seismic anisotropy in central Tibet: implications for deformation style and flow in the crust, *Geophys. Res. Lett.,* 31, L23601, doi:10:1029/2004GL021096.

Poli, P., H.A. Pedersen, M. Campillo, and the POLENET/LAPNET Working Group (2013), Noise directivity and group velocity tomography in a region with small velocity contrasts: the northern Baltic shield, *Geophys. J. Int.*, *192*(1), 413–424, doi:10.1093/gji/ggs034.

Rapine, R., F. Tilmann, M. West, J. Ni, and A. Rodgers (2003), Crustal structure of northern and southern Tibet from surface wave dispersion analysis, *Journal of Geophysical Research: Solid Earth*, *108*(B2), 2120, doi:10.1029/2001JB000445.

Readman, P.W., F. Hauser, B.M. O'Reilly, and V.C. Do (2009), Crustal anisotropy in southwest Ireland from analysis of controlled source shear-wave data, *Tectonophysics*, 474, 571-583.

Ritzwoller, M.H. and A.L. Levshin (2002), Estimating shallow shear velocities with marine multi-component seismic data, *Geophysics*, 67 (6), 1991-2004.

Ritzwoller, M.H., A.L. Levshin, L.I. Ratnikova, and A.A. Egorkin (1998), Intermediate period group velocity maps across Central Asia, Western China, and parts of the Middle East, *Geophys. J. Int.*, 134, 315-328.

Savage, M.K., F.C. Lin, and J. Towend (2013), Ambient noise cross-correlation observations of fundamental and higher-mode Rayleigh wave propagation governed by basement resonance, *Geophys. Res. Lett*, doi:10.1002/grl.50678.

Schlue, J.W., and L. Knopoff (1977), Shear wave polarization anisotropy in the Pacific basin, *Geophys. J. Roy. Astron. Soc.*,49, 145-165.

Shapiro, N. M., and M. H. Ritzwoller (2002), Monte-Carlo inversion for a global shear-velocity model of the crust and upper mantle, *Geophysical Journal International*, *151*(1), 88–105, doi:10.1046/j.1365-246X.2002.01742.x.

Shapiro, N. M., M. H. Ritzwoller, P. Molnar, and V. Levin (2004), Thinning and flow of Tibetan crust constrained by seismic anisotropy, *Science*, *305*(5681), 233–236, doi:10.1126/science.1098276.

Shen, W., M. H. Ritzwoller, and V. Schulte-Pelkum (2013a), A 3-D model of the crust and uppermost mantle beneath the Central and Western US by joint inversion of receiver functions and surface wave dispersion, *Journal of Geophysical Research: Solid Earth*, *118*(1), 262-276, doi:10.1029/2012JB009602.

Shen, W., M. H. Ritzwoller, V. Schulte-Pelkum, and F.-C. Lin (2013b), Joint inversion of surface wave dispersion and receiver functions: a Bayesian Monte-Carlo approach, *Geophys. J. Int.*, *192*(2), 807–836, doi:10.1093/gji/ggs050.

Sherrington, H. F., G. Zandt, and A. Frederiksen (2004), Crustal fabric in the Tibetan Plateau based on waveform inversions for seismic anisotropy parameters, *Journal of Geophysical Research: Solid Earth*, *109*(B2), B02312, doi:10.1029/2002JB002345.

Sloan, R. A., J. A. Jackson, D. McKenzie, and K. Priestley (2011), Earthquake depth distributions in central Asia, and their relations with lithosphere thickness, shortening and extension, *Geophys. J. Int.*, *185*(1), 1–29, doi:10.1111/j.1365-246X.2010.04882.x.

Takeo, A., K. Nishida, T. Isse, H. Kawakatsu, H. Shiobara, H. Sugioka, and T. Kanazawa (2013), Radially anisotropic structure beneath the Shikoku Basin from broadband surface wave analysis of ocean bottom seismometer records, *J. Geophys. Res. Solid Earth*, *118*, doi:10.1002/jgrb.50219.

Takeuchi, H., Y. Hamano, and Y. Hasegawa (1968), Rayleigh- and Love-wave discrepancy and the existence of magma pockets in the upper mantle, *Journal of Geophysical Research*, *73*(10), 3349–3350, doi:10.1029/JB073i010p03349.

Tatham, D. J., G. E. Lloyd, R. W. H. Butler, and M. Casey (2008), Amphibole and lower crustal seismic properties, *Earth and Planetary Science Letters*, *267*(1–2), 118–128, doi:10.1016/j.epsl.2007.11.042.

Trampert, J., and J. H. Woodhouse (1995), Global phase velocity maps of Love and Rayleigh waves between 40 and 150 seconds, *Geophysical Journal International*, *122*(2), 675–690, doi:10.1111/j.1365-246X.1995.tb07019.x.

Unsworth, M., W. Wenbo, A. G. Jones, S. Li, P. Bedrosian, J. Booker, J. Sheng, D. Ming, and T. Handong (2004), Crustal and upper mantle structure of northern Tibet imaged with magnetotelluric data, *Journal of Geophysical Research: Solid Earth*, *109*(B2), B02403, doi:10.1029/2002JB002305.

Valcke, S. L. A., M. Casey, G. E. Lloyd, J.-M. Kendall, and Q. J. Fisher (2006), Lattice preferred orientation and seismic anisotropy in sedimentary rocks, *Geophysical Journal International*, *166*(2), 652–666, doi:10.1111/j.1365-246X.2006.02987.x.

Vergne, J., G. Wittlinger, Q. Hui, P. Tapponnier, G. Poupinet, J. Mei, G. Herquel, and A. Paul (2002), Seismic evidence for stepwise thickening of the crust across the NE Tibetan plateau, *Earth and Planetary Science Letters*, *203*(1), 25–33, doi:10.1016/S0012-821X(02)00853-1.

Vergne, J., G. Wittlinger, V. Farra, and H. Su (2003), Evidence for upper crustal anisotropy in the Songpan-Ganze (northeastern Tibet) terrane, *Geophys. Res. Lett.*, 30, 1552, doi:10.1029/2002GL016847.

Villaseñor, A., M. H. Ritzwoller, A. L. Levshin, M. P. Barmin, E. R. Engdahl, W. Spakman, and J. Trampert (2001), Shear velocity structure of central Eurasia from inversion of surface wave velocities, *Physics of the Earth and Planetary Interiors*, *123*(2-4), 169–184, doi:10.1016/S0031-9201(00)00208-9.

Wang, C.-Y., L. Zhu, H. Lou, B.-S. Huang, Z. Yao, and X. Luo (2010), Crustal thicknesses and Poisson's ratios in the eastern Tibetan Plateau and their tectonic implications, *J. Geophys. Res.*, *115*(B11), B11301, doi:10.1029/2010JB007527.

Ward, D., K. Mahan, and V. Schulte-Pelkum (2012), Roles of quartz and mica in seismic anisotropy of mylonites, *Geophysical Journal International*, *190*(2), 1123–1134, doi:10.1111/j.1365-246X.2012.05528.x.

Wei, W. et al. (2001), Detection of widespread fluids in the Tibetan crust by magnetotelluric studies, *Science*, *292*(5517), 716–719, doi:10.1126/science.1010580.

Wendt, A. S., I. O. Bayuk, S. J. Covey-Crump, R. Wirth, and G. E. Lloyd (2003), An experimental and numerical study of the microstructural parameters contributing to the seismic anisotropy of rocks, *Journal of Geophysical Research: Solid Earth*, *108*(B8), 2365, doi:10.1029/2002JB001915.

Xie, J., W. Shen, M.H. Ritzwoller, Y. Yang, L. Zhou, Y. Zheng (2012), Imaging crustal anisotropy in eastern Tibet and South China using ambient noise and earthquake data, *AGU fall meeting*, 2012, T33D-2683.

Xu, L., S. Rondenay, and R. D. van der Hilst (2007), Structure of the crust beneath the southeastern Tibetan Plateau from teleseismic receiver functions, *Physics of the Earth and Planetary Interiors*, *165*(3–4), 176–193, doi:10.1016/j.pepi.2007.09.002.

Xu, Y., Z. Li, and S.W. Roecker (2007), Uppermost mantle structure and its relation with seismic activity in the central Tian Shan, *Geophys. Res. Lett.,* 34, L10304, doi:10.1029/2007GL029708.

Yang, Y. and M.H. Ritzwoller (2008), Characteristics of ambient seismic noise as a source for surface wave tomography, *Geochemistry, Geophysics, Geosystems*, 9(2), Q02008, doi:10.1029/2007GC001814.

Yang, Y. et al. (2010), Rayleigh wave phase velocity maps of Tibet and the surrounding regions from ambient seismic noise tomography, *Geochemistry, Geophysics, Geosystems*, *11*(8), Q08010, doi:10.1029/2010GC003119.

Yang, Y., M. H. Ritzwoller, Y. Zheng, W. Shen, A. L. Levshin, and Z. Xie (2012), A synoptic view of the distribution and connectivity of the mid-crustal low velocity zone beneath Tibet, *J. Geophys. Res.*, *117*, 20 pp., doi:201210.1029/2011JB008810.

Yao, H., C. Beghein, and R. D. van der Hilst (2008), Surface-wave array tomography in SE Tibet from ambient seismic noise and two-station analysis - II. Crustal and upper-mantle structure, *Geophysical Journal International*, *173*, 205–219.

Yao, H., R. D. van der Hilst, and J.-P. Montagner (2010), Heterogeneity and anisotropy of the lithosphere of SE Tibet from surface wave array tomography, *J. Geophys. Res.*, *115*(B12), B12307, doi:10.1029/2009JB007142.

Yao, H., Gouédard, P., Collins, J. a., McGuire, J. J., & Van der Hilst, R. D. (2011), Structure of young East Pacific Rise lithosphere from ambient noise correlation analysis of fundamental- and higher-mode Scholte-Rayleigh waves, *Comptes Rendus Geoscience*, *343*(8-9), 571–583. doi:10.1016/j.crte.2011.04.004.

Yue, H., et al. (2012), Lithospheric and upper mantle structure of the northeastern Tibetan Plateau, *J. Geophys. Res.*, *117*(B5), B05307, doi:10.1029/2011JB008545.

Zandt, G., and C. J. Ammon (1995), Continental crust composition constrained by measurements of crustal Poisson's ratio, *Nature*, *374*(6518), 152–154, doi:10.1038/374152a0.

Zhang, Z. M., J. G. Liou, and R. G. Coleman (1984), An outline of the plate tectonics of China, *Geological Society of America Bulletin*, *95*(3), 295–312, doi:10.1130/0016-7606(1984)95<295:AOOTPT>2.0.CO;2.

Zhang, P., Q. Deng, G. Zhang, J. Ma, W. Gan, W. Min, F. Mao, and Q. Wang (2003), Active tectonic blocks and strong earthquakes in the continent of China, *Sci. China Ser. D-Earth Sci.*, *46*(2), 13–24, doi:10.1360/03dz0002.

Zhang, P.-Z., X. Wen, Z.-K. Shen, and J. Chen (2010), Oblique, High-Angle, Listric-reverse faulting and associated development of strain: The Wenchuan Earthquake of May 12, 2008, Sichuan, China, *Annual Review of Earth and Planetary Sciences*, *38*(1), 353–382, doi:10.1146/annurev-earth-040809-152602.

Zheng, X.-F., Z.-X. Yao, J.-H. Liang, and J. Zheng (2010), The role played and opportunities provided by IGP DMC of China National Seismic Network in

Wenchuan Earthquake disaster relief and researches, *Bulletin of the Seismological Society of America*, *100*(5B), 2866–2872, doi:10.1785/0120090257.

Zheng, S., X. Sun, X. Song, Y. Yang, and M. H. Ritzwoller (2008), Surface wave tomography of China from ambient seismic noise correlation, *Geochem. Geophys. Geosyst.*, 9, Q0502, doi:10.1029/2008GC001981.

Zhou, L., J. Xie, W. Shen, Y. Zheng, Y. Yang, H. Shi, and M. H. Ritzwoller (2012), The structure of the crust and uppermost mantle beneath South China from ambient noise and earthquake tomography, *Geophysical Journal International*, *189*(3), 1565–1583, doi:10.1111/j.1365-246X.2012.05423.x.

Table 1. Model parameter constraints

	Model parameter	Perturbation	Reference model
Sedimentary layer	Sediment thickness Vsv in sediment Vsh in sediment	+/- 100% +/- 1.0 km/s equals to Vsv	*Laske & Masters* [1997]
Crystalline crustal layer	Crustal thickness 5 Vsv B-splines* 5 Vsh B-splines*	+/- 10% +/- 20% +/- 20%	*Shapiro & Ritzwoller* [2002]
Mantle layer to 150 km	5 Vsv B-splines Anisotropy	+/- 20% 0	*Shapiro & Ritzwoller* [2002]

* $\Delta v/\Delta h \geq 0$ or $-1/70\ s^{-1} \leq \Delta v/\Delta h < 0$

Figure Captions

Figure 1. (a) Reference map of the study region in which red lines indicate the boundaries of major geological units and basins [*Zhang et al.*, 1984, 2003]. The white contour outlines what we refer to as the Longmenshan region. The blue line is the path between stations X4.F17 and X4.D26 referenced in Fig. 2. Points A, B, C, and D indicate sample points referenced in Figs. 6, 7, 13, 16, 17, and 19. (b) Locations of seismic stations used in this study. Red and black triangles are stations used to measure Love wave dispersion, while blue and black triangles indicate stations used for Rayleigh wave measurements.

Figure 2. (a) Example of Rayleigh wave (blue, vertical-vertical, Z-Z) and Love wave (red, transverse-transverse, T-T) cross-correlations for a pair of stations (X4.F17, X4.D26) located in the Qiangtang terrane (Fig. 1a), band pass filtered between 5 and 100 sec period. (b) Observed Rayleigh and Love wave phase speed curves measured from the cross-correlations are presented as 1 standard deviation (1σ) error bars (red-Love, blue-Rayleigh). Inverting these data for an isotropic model (Vs = Vsh = Vsv) produces the best fitting green curves, which demonstrates a systematic misfit to the data (predominantly the Love waves) and a Rayleigh-Love discrepancy. Allowing crustal anisotropy (Vsh $\neq$ Vsv), produces the blue and red dispersion curves that fit the data.

Figure 3. Example estimated Rayleigh (a,b) and Love (c,d) wave phase speed maps at 10 (a,c) and 40 sec (b,d) period determined from ambient noise cross-correlations.

Figure 4. Uncertainties (1σ) in the Rayleigh and Love wave phase speed maps averaged across the study region estimated using the eikonal tomography method of *Lin et al.*[2009].

Figure 5. Representation of the parameterization used across the study region. In the crust, five B-splines (1-5) are used to represent Vsv, but three B-splines (2-4) are used to represent Vsh. In the mantle, five B-splines are estimated for Vsv but Vsh is derived from the strength of radial anisotropy in the model of *Shapiro and Ritzwoller* [2002]. A total of 16 parameters represent the model at each spatial location.

Figure 6. Prior (white histograms) and posterior distributions for Vsv (blue), Vsh (red) and Vs radial anisotropy (green, γ in percent) at 20, 35, and 50 km depth for point B in the Qiangtang terrane (Fig. 1a). The mean and standard deviation for each posterior distribution are shown in each panel.

Figure 7. Examples of dispersion curves and estimated radially anisotropy for four spatial locations (A, B, C, D) identified in Fig. 1a. (a) Point A (98.5, 36.0) near the eastern edge of the Qaidam Basin. Local Rayleigh and Love wave phase speed curves presented as one standard deviation (1σ) error bars. Predictions from the average of the anisotropic model distribution in (b) are shown as solid lines and green lines are predictions from the Voigt-averaged isotropic Vs model. Misfits (defined as $\chi = \sqrt{S/N}$ where S is defined in eq. (3)) correlated with anisotropic and isotropic models are shown at the upper left corner. (b) Point A (cont.). Inversion result in which the one standard deviation (1σ) model distributions are shown with the grey corridors for Vsh and Vsv, with the average of each ensemble plotted with bold blue (Vsv) and red (Vsh) lines. The model ensembles are nearly coincident in the crust, consistent with an isotropic crust. (c) & (d) Point B (96.5, 32.5) in the Qiangtang terrane where the central crust has strong positive radial anisotropy between 20 and 50 km depth and weak negative anisotropy above about 15 km depth. (e) & (f) Point C (105.0, 30.0) in the Sichuan Basin where the central crust has strong positive radial anisotropy between depths of 10 and 25 km. (g) & (h) Point D (102.5, 30.0) between Tibet and the Sichuan Basin where the central crust has strong negative radial anisotropy between 20 and 50 km depth.

Figure 8. The average of the posterior distributions of (a) Vsv, (b) Vsh, and (c) Vs at 35 km depth in km/s, which is in the middle crust beneath the Tibetan Plateau. Regions with very low velocities (<3.4 km/s) are encircled by white contours. (d) The average of the posterior distribution of crustal thickness in km.

Figure 9. Maps of the mean of the posterior distribution for estimates of radial anisotropy at (a) 10 km depth, (b) 35 km depth, and (c) 90% of the depth to Moho in the lowermost crust. Radial anisotropy is the percent difference between Vsh and Vsv at each location and depth (γ) and Vs is the Voigt-averaged shear wave speed. Blue lines in (a) identify the locations of the vertical cross-sections in Fig. 10**.**

Figure 10. Vertical cross-sections of (upper left) Vsv, (middle left) Vsh, and (lower left) Vs radial anisotropy γ along profile A (Fig. 9a), taken from the mean of the posterior distribution at each location and depth**.** Topography is shown at the top of each panel as are locations of geological-block boundaries (SG: Songpan-Ganzi terrane, CD: Chuandian terrane, LS: Lhasa terrane, QL: Qilian terrane, SCB: Sichuan Basin, SYN: South Yunnan region, YZ: Yangtze craton). Crustal shear velocities are presented in absolute units (km/s), Vs radial anisotropy is presented as the percent difference between Vsh and Vsv (γ), and mantle velocities are percentage perturbations relative to 4.4 km/s. (Right) Vs radial anisotropy is presented beneath profiles B, C, and D (Fig. 9a).

Figure 11. Maps of the one standard deviation (i.e., error) of the posterior distribution for estimates of Vs radial anisotropy at (a) 10 km depth, (b) 35 km depth, and (c) 90% of the depth to Moho. Results are in the same units as radial anisotropy, not in the percentage of radial anisotropy at each point.

Figure 12. Plots of the spatial distribution of the mean of the posterior distributions of Vs radial anisotropy across (a) the Songpan-Ganzi terrane between depths of 5 and 15 km, (b) eastern Tibet at depths between 30 and 40 km, (c) the Sichuan Basin at depths between 5 and 20 km, and (d) the Longmenshan region between eastern Tibet and the Sichuan Basin between 25 and 35 km. (e) The distribution of the mean of the posterior distribution for Voigt-averaged shear wave speed Vs across eastern Tibet between depths of 30 and 40 km.

Figure 13. (a) Percent of accepted models at each location with positive Vs radial anisotropy γ (Vsh > Vsv) at 35 km depth. Values of 2.2%, 15.8%, 84.2%, and 97.8% are contoured by black lines, which are correlated with the position of $\pm 1\ \sigma$ and $\pm 2\ \sigma$ for a Gaussian distribution. (b) Prior (white histogram in the background) and posterior (colored histogram) distributions of Vs radial anisotropy in percent at 35 km depth for locations A, B, and D of Fig. 1a. The red line indicates the position of zero radial anisotropy. The percent of models with positive radial anisotropy is indicated to the right of each panel. (c) Same as (a), but for positive Vs radial anisotropy at 10 km depth. (d) Same as (a), but for positive Vs radial anisotropy at 15 km depth.

Figure 14. (a) Similar to Fig. 13a, but this figure is the percentage of accepted models at each location with Voigt-averaged Vs > 3.4 km/s at 35 km depth. (b) Same as (a), but for Vs < 3.4 km/s at 35 km depth.

Figure 15. The spatially averaged effect of crustal parameterization of radial anisotropy on the mean and standard deviation of Vs radial anisotropy averaged across the Tibetan crust. Crustal radial anisotropy and uncertainty are presented as error bars as a function of (a) absolute depth and (b) depth measured as a ratio of crustal thickness, averaged over the study region where surface elevation is more than 3 km (black contour in Fig. 1a). The middle of each error bar is the average amplitude of Vs radial anisotropy in percent and the half-width of the error bar is the average one-standard deviation uncertainty. Blue bars result from the more tightly constrained inversion (uppermost and lowermost crust are approximately isotropic, Vsh=Vsv for crustal B-splines 1 and 5 in Fig. 5, but Vsh and Vsv can differ for splines 2 to 4). Red bars are results from the less constrained inversion (radial anisotropy is allowed across the entire crust, Vsv may differ from Vsh for all five crustal B-splines).

Figure 16. Trade-off between the depth-averaged (from Moho to 150 km) mantle Vs radial anisotropy used in the inversion and (a) the depth-averaged (±5 km around the middle crust) mid-crustal Vs radial anisotropy and (b) the depth-averaged (±5 km around the middle crust) mid-crustal Voigt-averaged Vs. Each dot is the depth-averaged value and half-widths of the error bars are the depth-averaged one-standard deviation uncertainty. Both come from the inversion with the given mantle radial anisotropy at location D identified in Fig. 1a. The triangles are the values in our final model. (c)&(d) Similar to (a)&(b), but showing the trade-off between the crustal thickness and (c) the depth-averaged mid-crustal Vs radial anisotropy and (d) the depth-averaged mid-crustal Voigt-averaged Vs.

Figure 17. Similar to Fig. 16, but shows the trade-off between the fixed value of the crustal Vp/Vs used in the inversion and (a) the depth-averaged (from 30 to 40 km) crustal Vs radial anisotropy and (b) the depth-averaged (from 30 to 40 km) mid-crustal Voigt-averaged Vs. Values are from inversion with the given crustal Vp/Vs at location B identified in Fig. 1a.

Figure 18. Example sensitivity kernels for Rayleigh and Love wave phase speeds at 30 sec period to perturbations in Vsv, Vsh, Vpv, Vph, and η at different depths.

Figure 19. Comparison of the inversion results between the simple model of Vs radial anisotropy (γ-simple, red error-bars; $\varepsilon = 0$, $\eta = 1$) and the realistic model (γ-realistic, blue error-bars; $\varepsilon = 0.5\gamma$, $\eta = 1-4.2\gamma$) for (a) crustal Vs radial anisotropy and (b) crustal Voigt-averaged Vs. Both plots are for the four locations (A-D) identified in Fig. 1a. The results at locations A, B, and D are depth-averaged over the middle crust, while results at location C is depth-averaged over the upper crust. The half-widths of the error bars are the depth-averaged uncertainty (1σ). Green lines are the locus of points for identical results from the simple and realistic models of Vs radial anisotropy and all error bars overlap this line.

Figure 20. Synthetic results for the fundamental and higher mode Love waves. (a) Dispersion curves computed from an isotropic model based on the structure at location B in Fig. 1a. Red lines represent phase- and group- velocity dispersion curves of the fundamental model Love wave (L0) and dashed blue lines represent that of the first higher mode Love wave (L1). (b) Spectral amplitudes computed for a horizontal force at the surface (bold lines) or at 20 km depth (thin lines) for the fundamental Love wave (red lines) and first overtone Love wave (blue lines). (c) Green's function computed from the same model in (a) with a single horizontal force located at the surface (0-km depth). Red line indicates the fundamental Love wave; the dashed blue line is the first overtone Love wave. (d) Similar to (c), but computed with a single horizontal force located at 20-km depth. (e)-(f) Frequency-time analysis (FTAN) diagram for the superposition of the Green's functions shown in (c) and (d), respectively. Red and blue lines are the dispersion curves shown in (a) and black lines are the phase and group velocity dispersion curves measured using FTAN.

Figure 21. (a) Pictorial definition of the rotation angle θ for a hexagonally symmetric system. (b) Vs radial anisotropies, γ = (Vsh-Vsv)/Vs, plotted as a function of rotation angle θ, computed by re-orientating the elastic tensors of the crustal rock samples of *Erdman et al.* [2013]. Samples locations are identified by line color as indicated.

1668

Figure 1

(a)

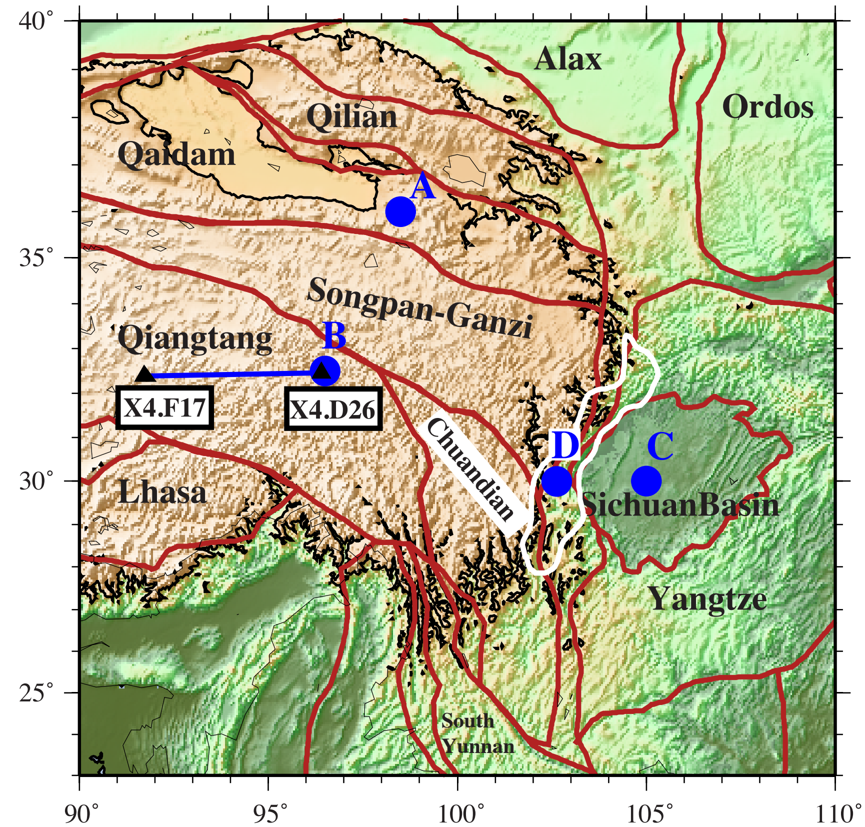
40°
35°
30°
25°
90°
95°
100°
105°
110°
Alax
Ordos
Qilian
Qaidam
A
Songpan-Ganzi
Qiangtang
B
X4.F17
X4.D26
Chuandian
D
C
Lhasa
SichuanBasin
Yangtze
South
Yunnan

(b)

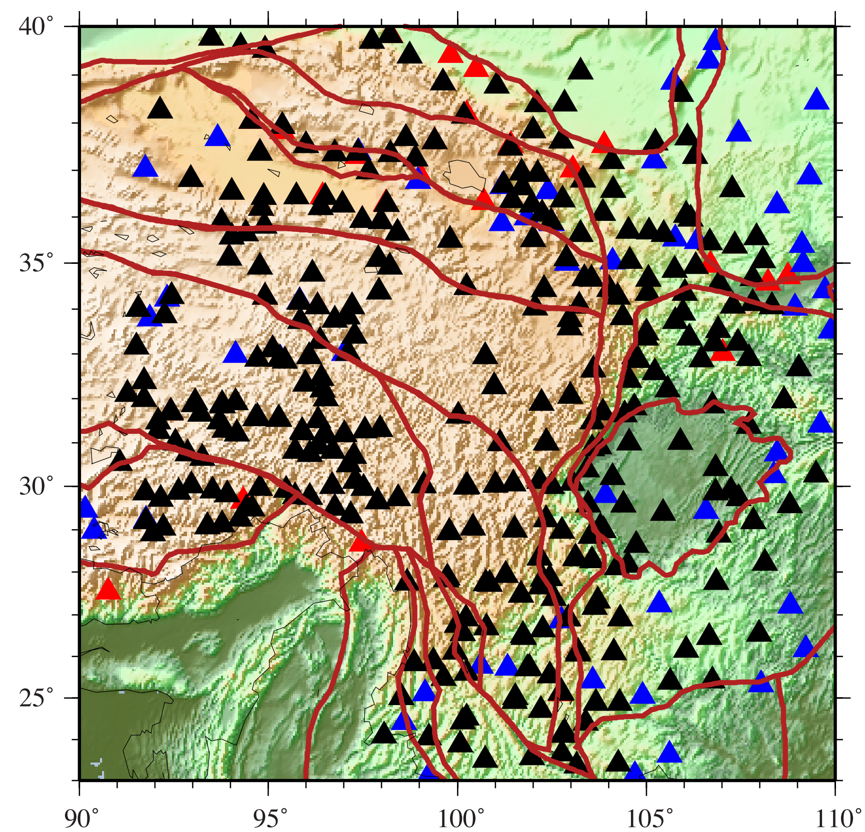
40°
35°
30°
25°
90°
95°
100°
105°
110°

Figure 2

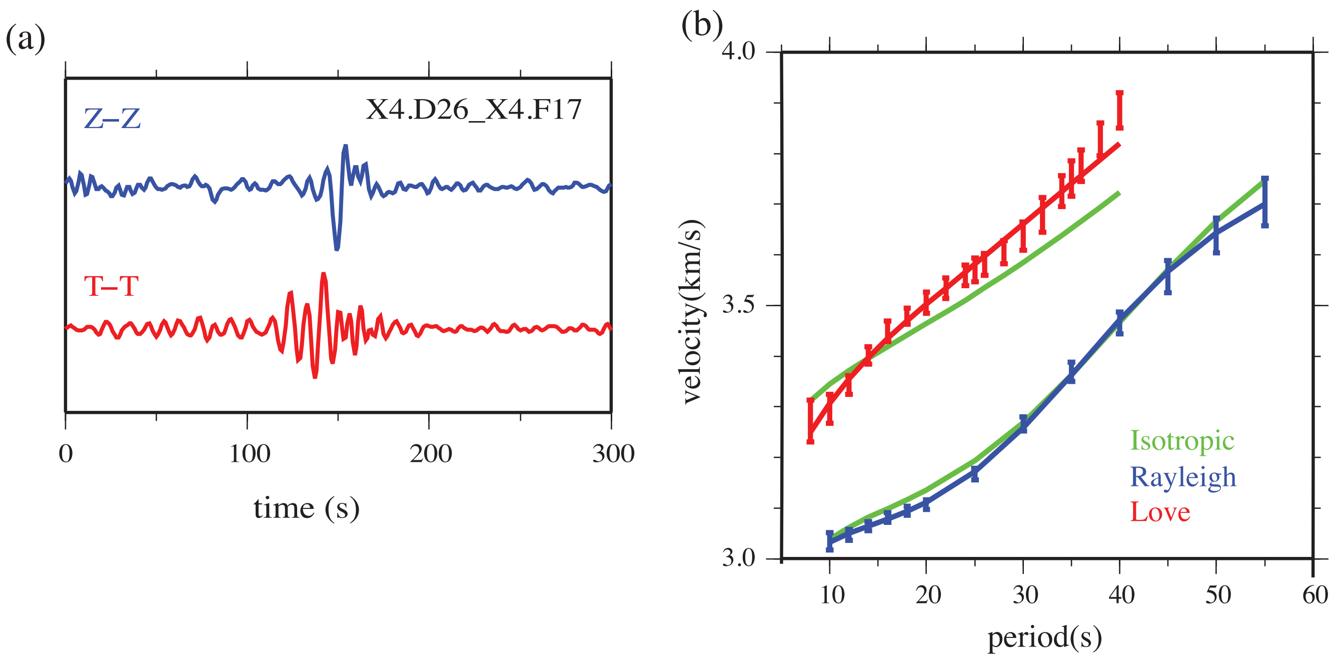

(a)
Z–Z
X4.D26_X4.F17
T–T
0
100
200
300
time (s)
(b)
4.0
3.5
3.0
velocity(km/s)
10
20
30
40
50
60
period(s)
Isotropic
Rayleigh
Love

Figure 3

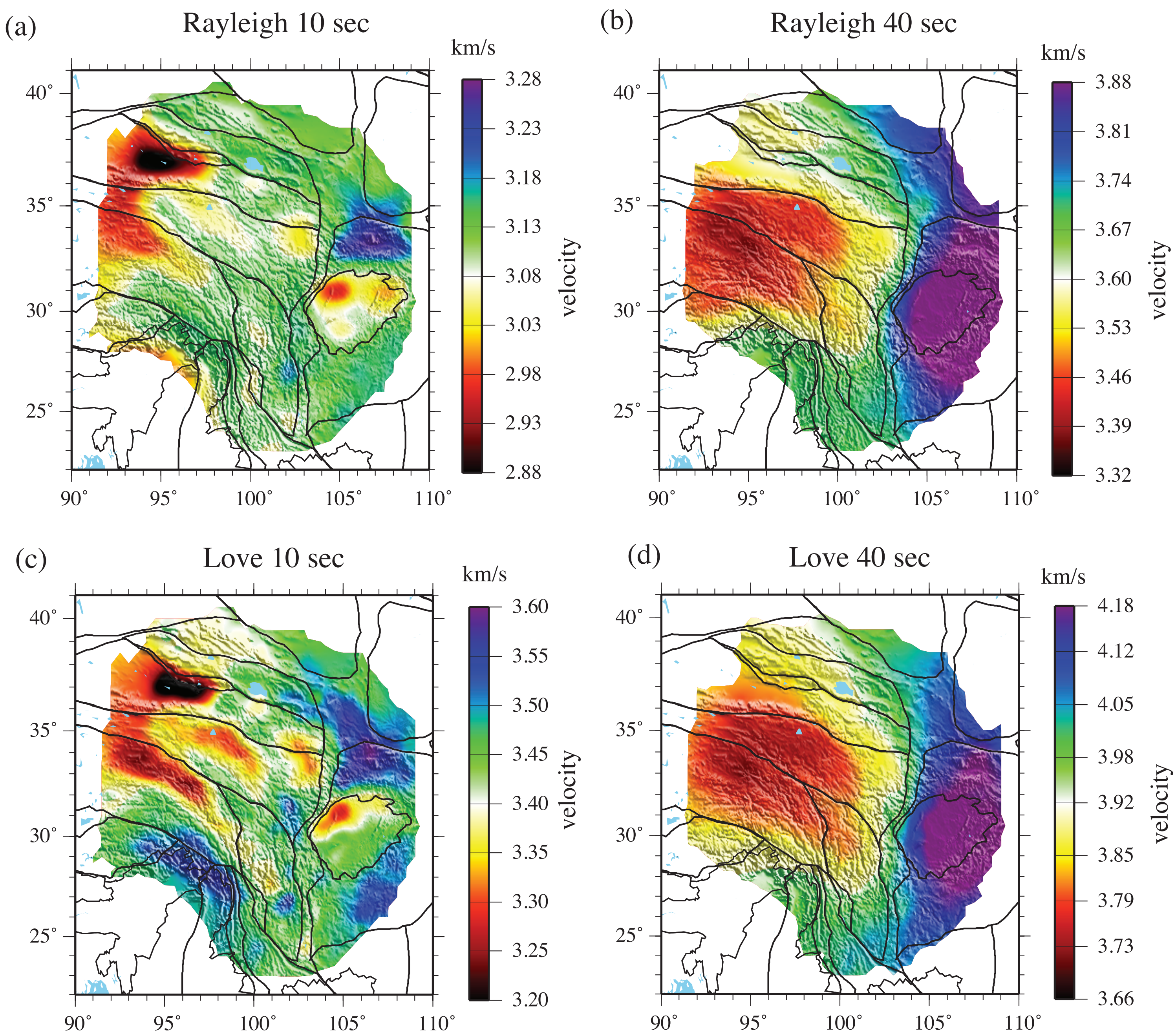
(a)
Rayleigh 10 sec
km/s
3.28
3.23
3.18
3.13
3.08
3.03
2.98
2.93
2.88
velocity
(b)
Rayleigh 40 sec
km/s
3.88
3.81
3.74
3.67
3.60
3.53
3.46
3.39
3.32
velocity
(c)
Love 10 sec
km/s
3.60
3.55
3.50
3.45
3.40
3.35
3.30
3.25
3.20
velocity
(d)
Love 40 sec
km/s
4.18
4.12
4.05
3.98
3.92
3.85
3.79
3.73
3.66
velocity
40°
35°
30°
25°
90°
95°
100°
105°
110°

Figure 4

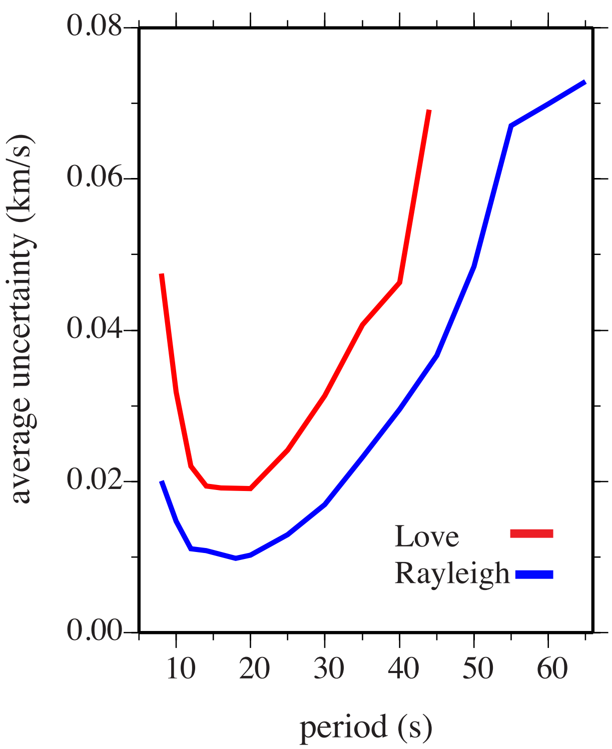
0.08
0.06
0.04
0.02
0.00
average uncertainty (km/s)
10
20
30
40
50
60
period (s)
Love
Rayleigh

Figure 5

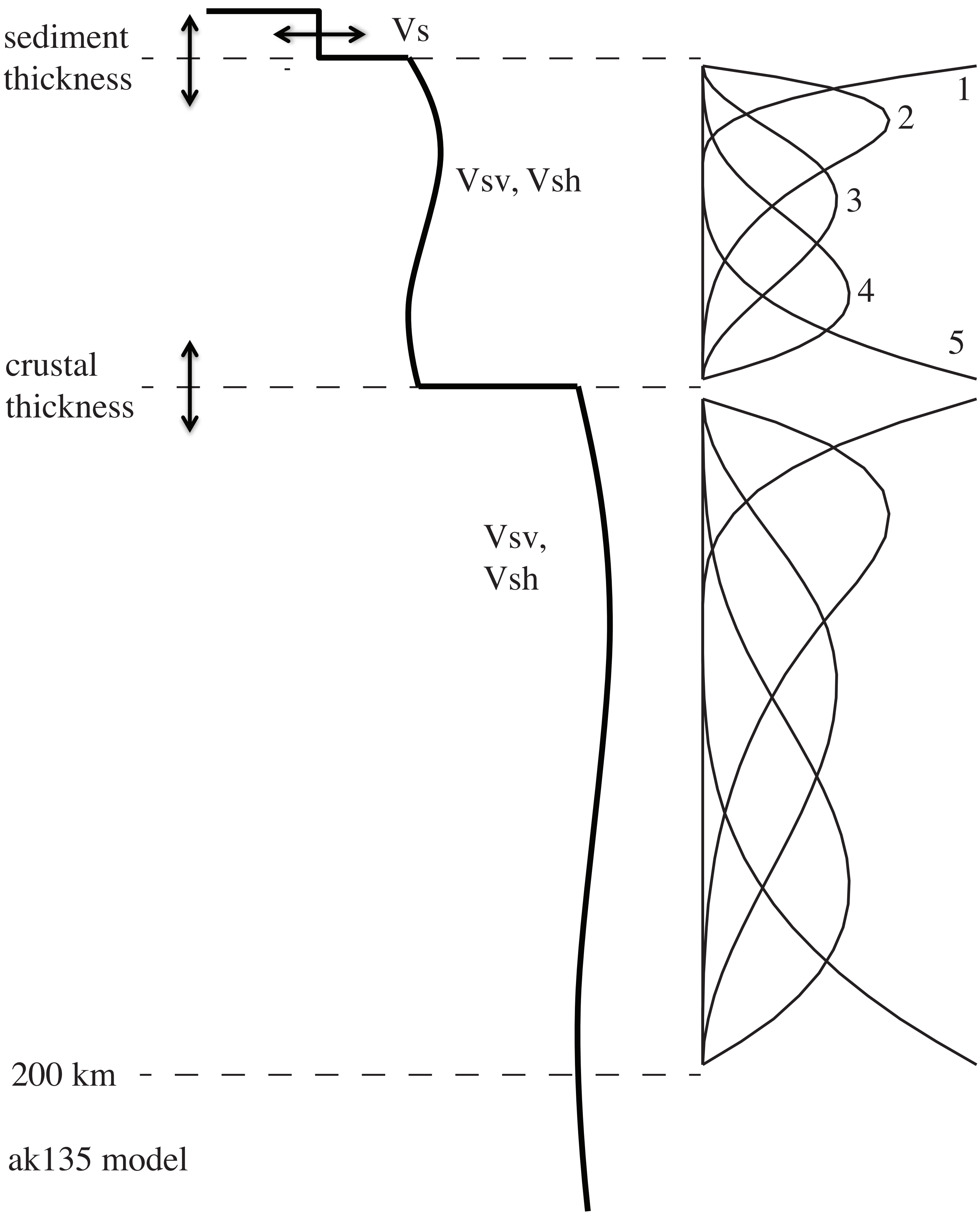

sediment thickness
Vs
Vsv, Vsh
1
2
3
4
5
crustal thickness
Vsv,
Vsh
200 km
ak135 model

Figure 6

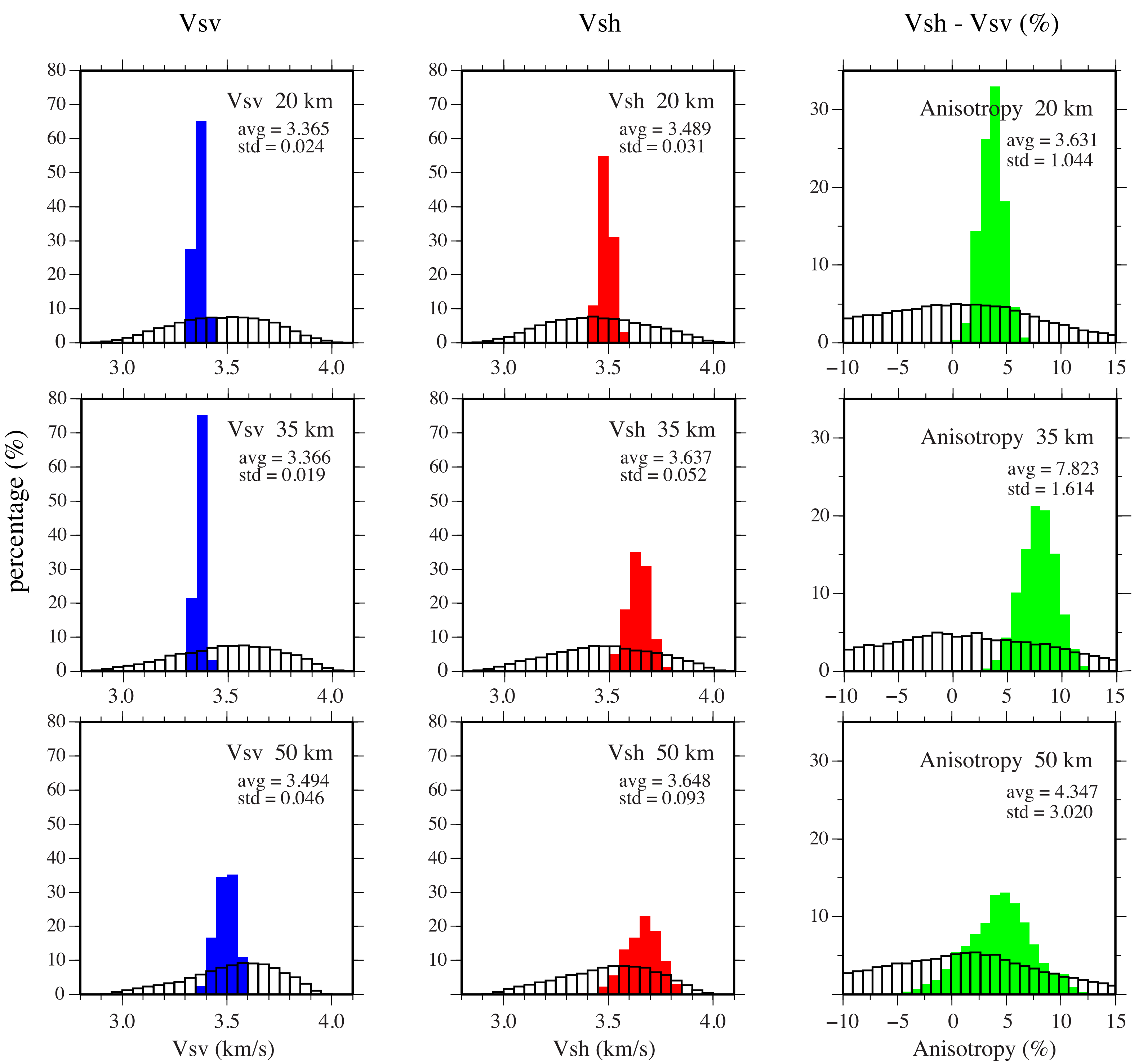

Vsv
Vsh
Vsh - Vsv (%)
Vsv 20 km
avg = 3.365
std = 0.024
Vsh 20 km
avg = 3.489
std = 0.031
Anisotropy 20 km
avg = 3.631
std = 1.044
Vsv 35 km
avg = 3.366
std = 0.019
Vsh 35 km
avg = 3.637
std = 0.052
Anisotropy 35 km
avg = 7.823
std = 1.614
Vsv 50 km
avg = 3.494
std = 0.046
Vsh 50 km
avg = 3.648
std = 0.093
Anisotropy 50 km
avg = 4.347
std = 3.020
percentage (%)
Vsv (km/s)
Vsh (km/s)
Anisotropy (%)

Figure 7

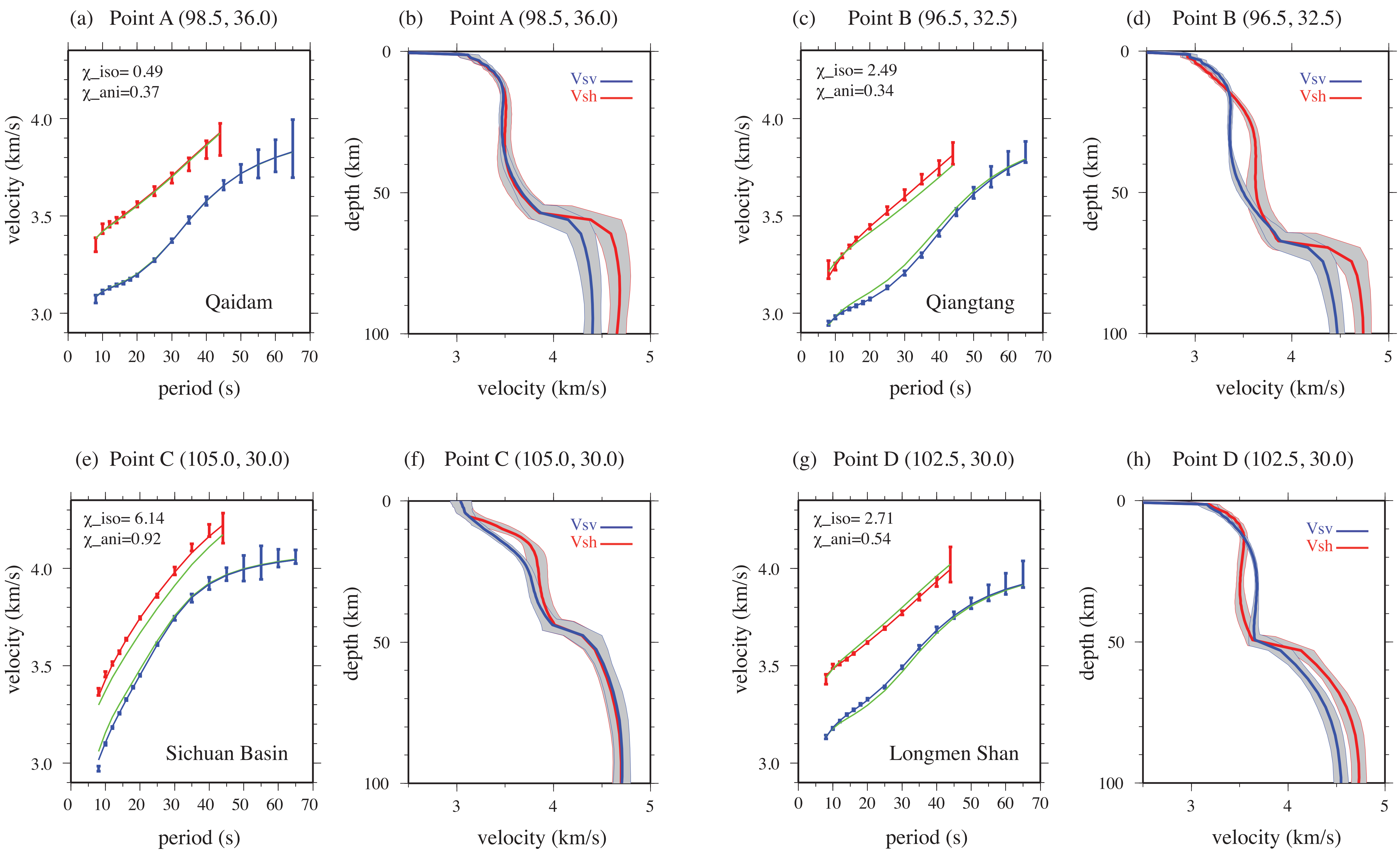
(a) Point A (98.5, 36.0)
χ_iso= 0.49
χ_ani=0.37
Qaidam
velocity (km/s)
period (s)
(b) Point A (98.5, 36.0)
Vsv
Vsh
depth (km)
velocity (km/s)
(c) Point B (96.5, 32.5)
χ_iso= 2.49
χ_ani=0.34
Qiangtang
velocity (km/s)
period (s)
(d) Point B (96.5, 32.5)
Vsv
Vsh
depth (km)
velocity (km/s)
(e) Point C (105.0, 30.0)
χ_iso= 6.14
χ_ani=0.92
Sichuan Basin
velocity (km/s)
period (s)
(f) Point C (105.0, 30.0)
Vsv
Vsh
depth (km)
velocity (km/s)
(g) Point D (102.5, 30.0)
χ_iso= 2.71
χ_ani=0.54
Longmen Shan
velocity (km/s)
period (s)
(h) Point D (102.5, 30.0)
Vsv
Vsh
depth (km)
velocity (km/s)

Figure 8

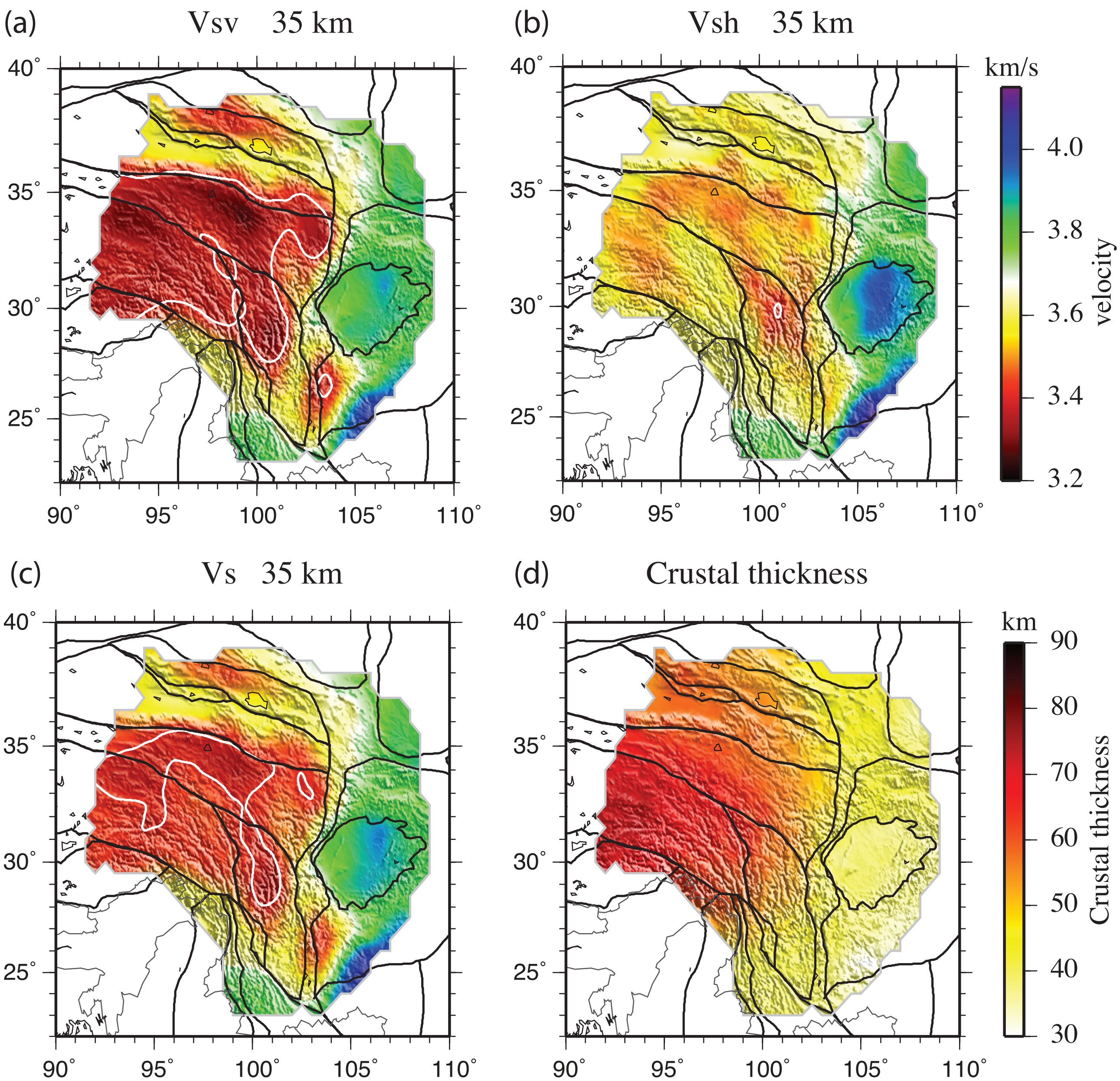

(a)
Vsv 35 km
(b)
Vsh 35 km
(c)
Vs 35 km
(d)
Crustal thickness
40°
35°
30°
25°
90°
95°
100°
105°
110°
km/s
4.0
3.8
3.6
3.4
3.2
velocity
km
90
80
70
60
50
40
30
Crustal thickness

Figure 9

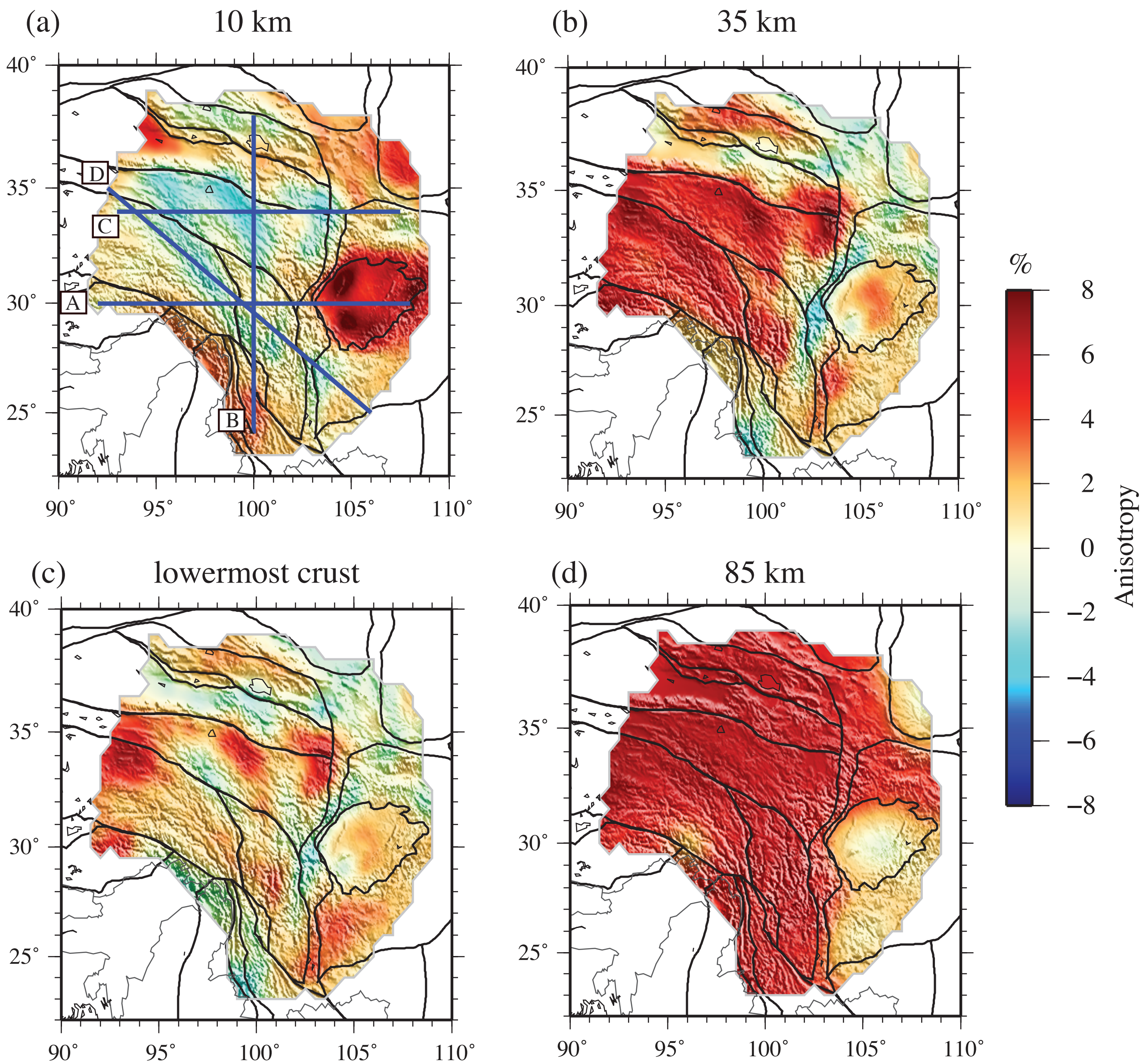

(a)
10 km
(b)
35 km
(c)
lowermost crust
(d)
85 km
A
B
C
D
40˚
35˚
30˚
25˚
90˚
95˚
100˚
105˚
110˚
%
8
6
4
2
0
−2
−4
−6
−8
Anisotropy

Figure 10

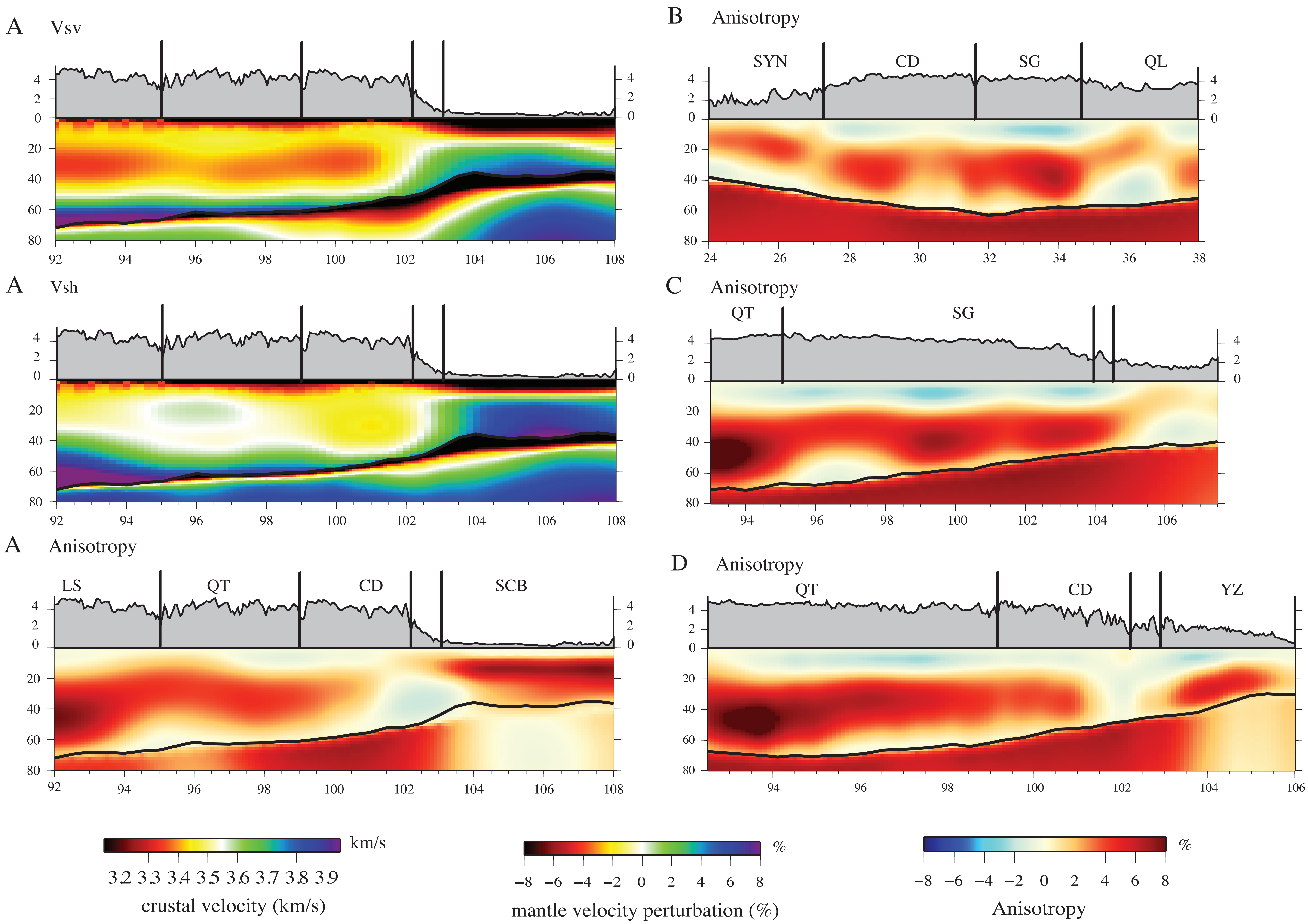

A Vsv
B Anisotropy
SYN
CD
SG
QL
A Vsh
C Anisotropy
QT
SG
A Anisotropy
LS
QT
CD
SCB
D Anisotropy
QT
CD
YZ
km/s
3.2 3.3 3.4 3.5 3.6 3.7 3.8 3.9
crustal velocity (km/s)
%
−8 −6 −4 −2 0 2 4 6 8
mantle velocity perturbation (%)
%
−8 −6 −4 −2 0 2 4 6 8
Anisotropy

Figure 11

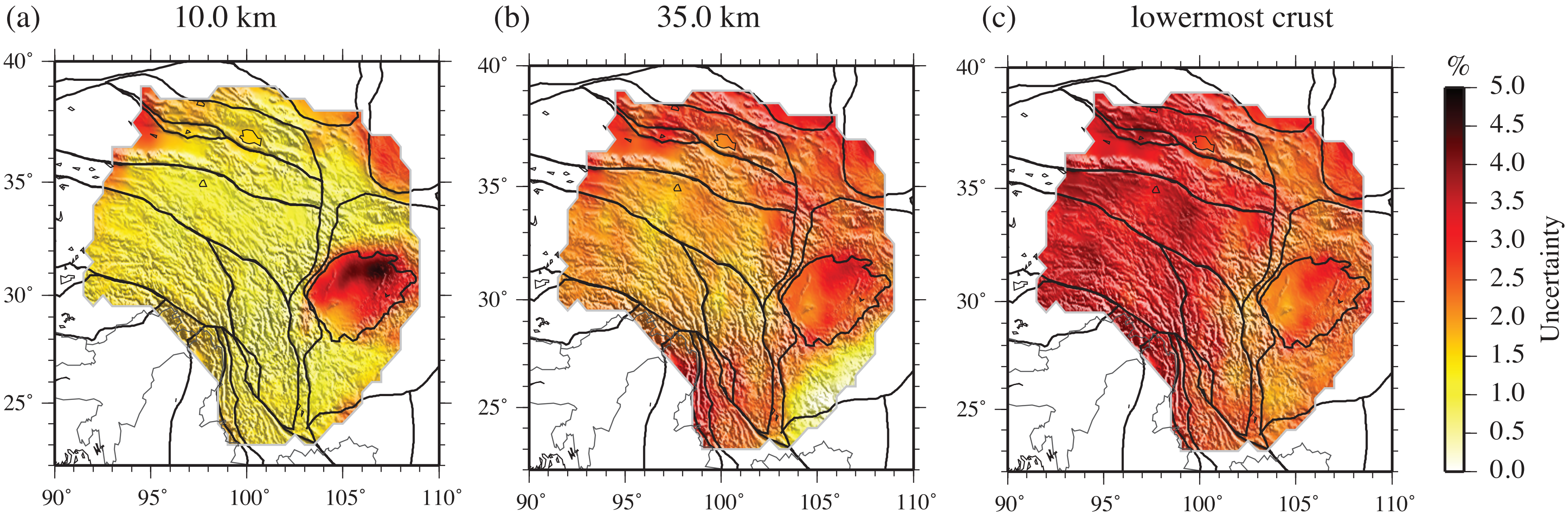

(a)
10.0 km
(b)
35.0 km
(c)
lowermost crust
40°
35°
30°
25°
90°
95°
100°
105°
110°
%
5.0
4.5
4.0
3.5
3.0
2.5
2.0
1.5
1.0
0.5
0.0
Uncertainty

Figure 12

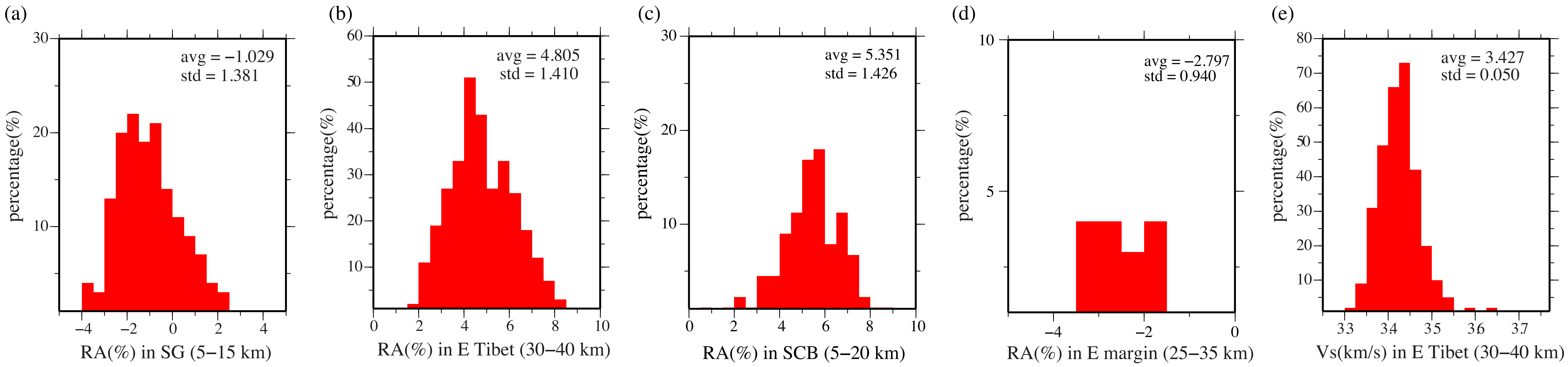

(a)
avg = −1.029
std = 1.381
percentage(%)
RA(%) in SG (5−15 km)
(b)
avg = 4.805
std = 1.410
percentage(%)
RA(%) in E Tibet (30−40 km)
(c)
avg = 5.351
std = 1.426
percentage(%)
RA(%) in SCB (5−20 km)
(d)
avg = −2.797
std = 0.940
percentage(%)
RA(%) in E margin (25−35 km)
(e)
avg = 3.427
std = 0.050
percentage(%)
Vs(km/s) in E Tibet (30−40 km)

Figure 13

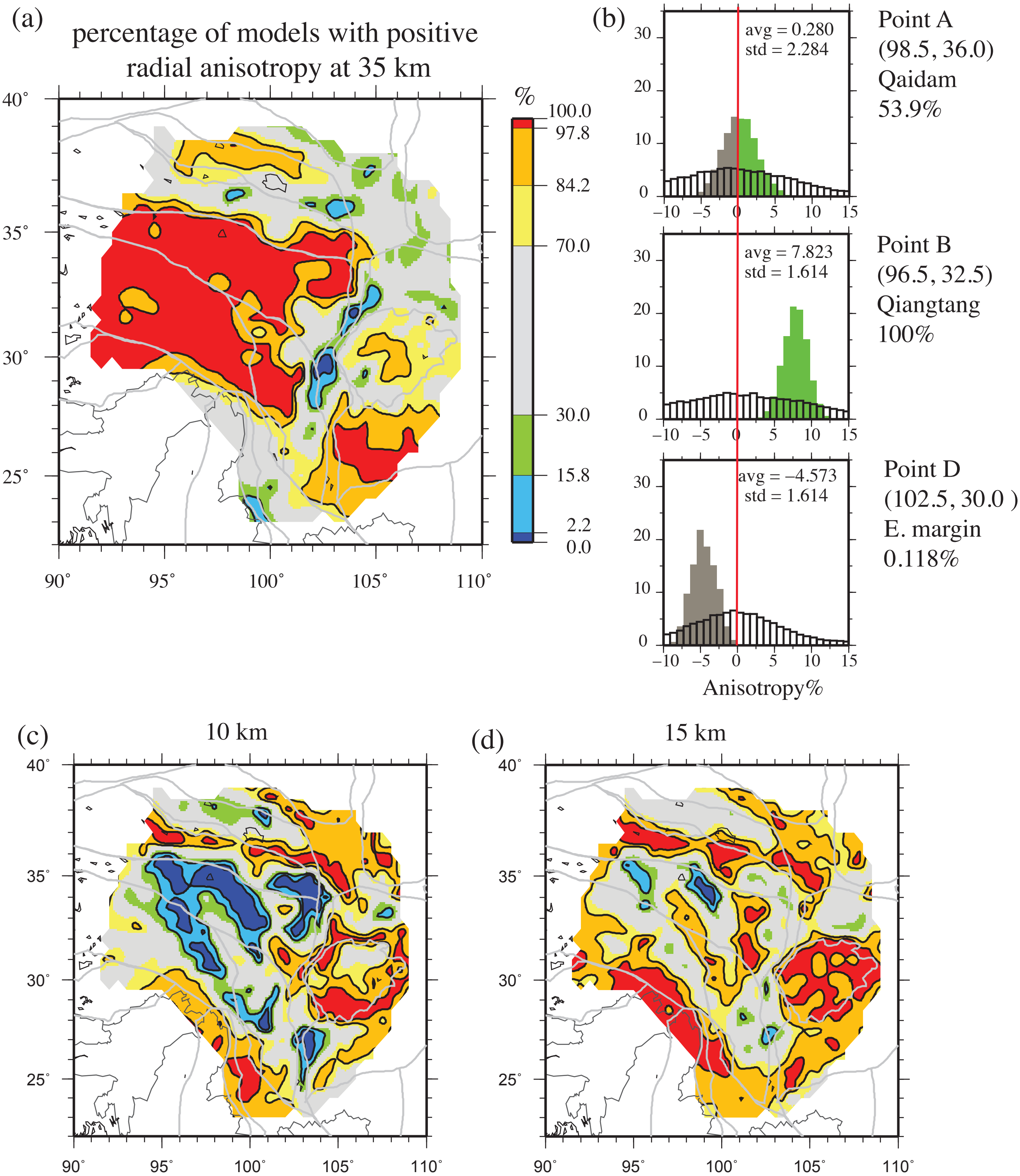

(a)
percentage of models with positive radial anisotropy at 35 km
%
100.0
97.8
84.2
70.0
30.0
15.8
2.2
0.0
40°
35°
30°
25°
90°
95°
100°
105°
110°
(b)
avg = 0.280
std = 2.284
Point A
(98.5, 36.0)
Qaidam
53.9%
avg = 7.823
std = 1.614
Point B
(96.5, 32.5)
Qiangtang
100%
avg = −4.573
std = 1.614
Point D
(102.5, 30.0)
E. margin
0.118%
Anisotropy%
(c)
10 km
(d)
15 km

Figure 14

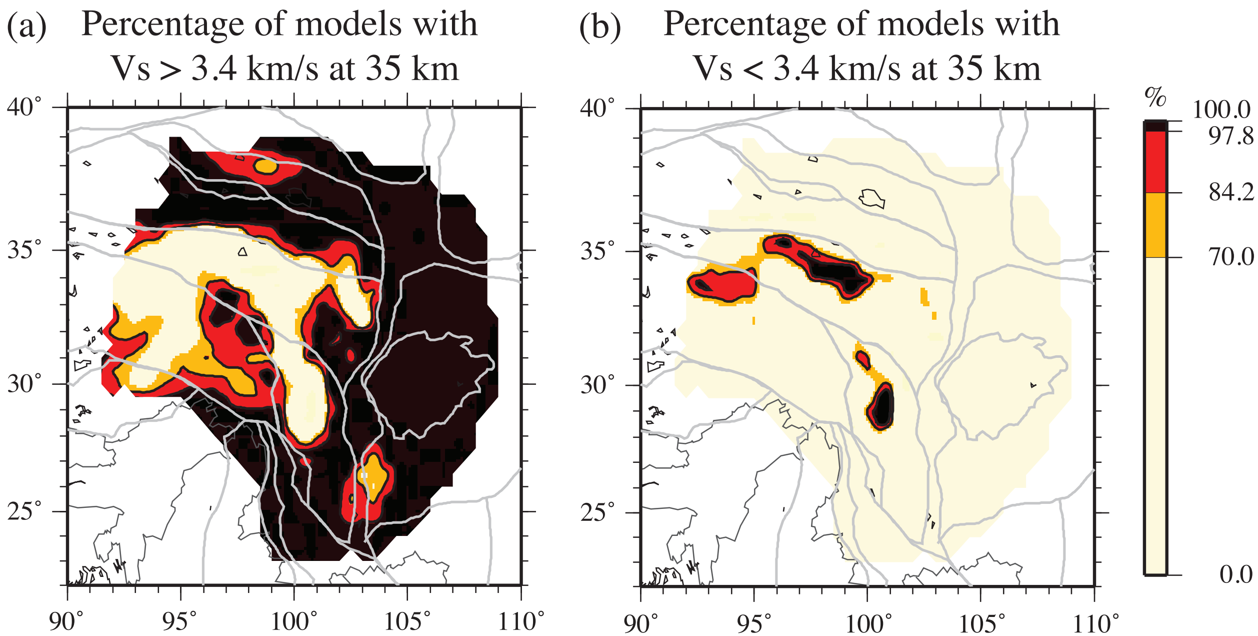

(a) Percentage of models with
Vs > 3.4 km/s at 35 km
(b) Percentage of models with
Vs < 3.4 km/s at 35 km
40°
35°
30°
25°
90°
95°
100°
105°
110°
%
100.0
97.8
84.2
70.0
0.0

Figure 15

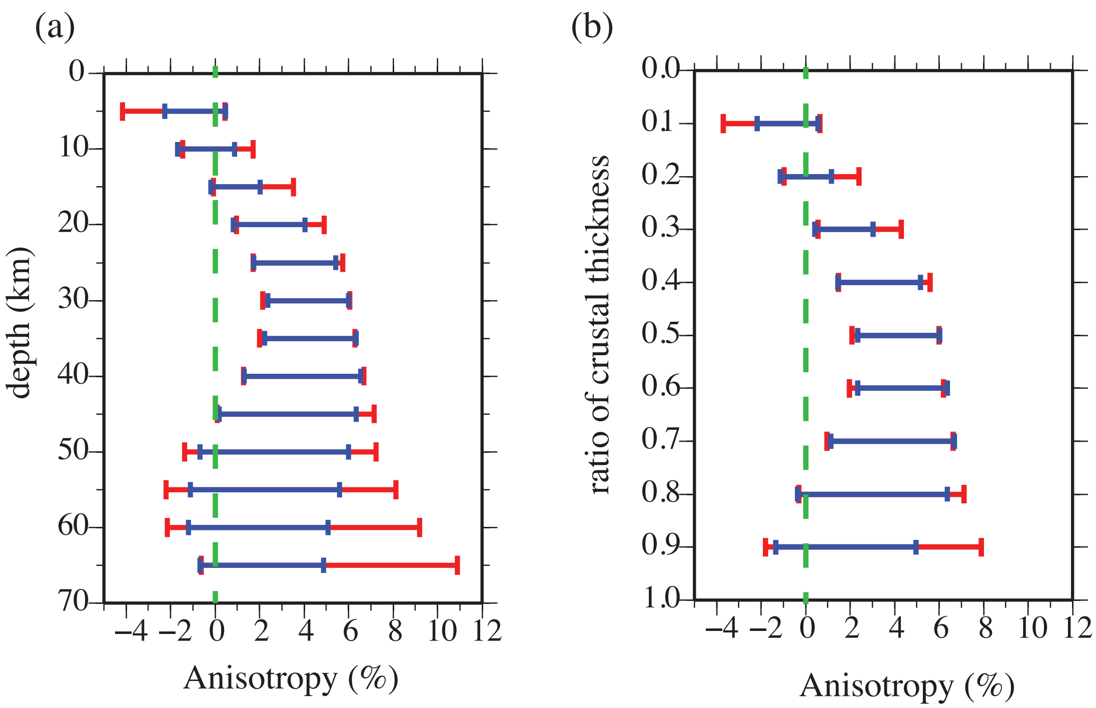
(a)
0
10
20
30
40
50
60
70
depth (km)
−4 −2 0 2 4 6 8 10 12
Anisotropy (%)
(b)
0.0
0.1
0.2
0.3
0.4
0.5
0.6
0.7
0.8
0.9
1.0
ratio of crustal thickness
−4 −2 0 2 4 6 8 10 12
Anisotropy (%)

Figure 16

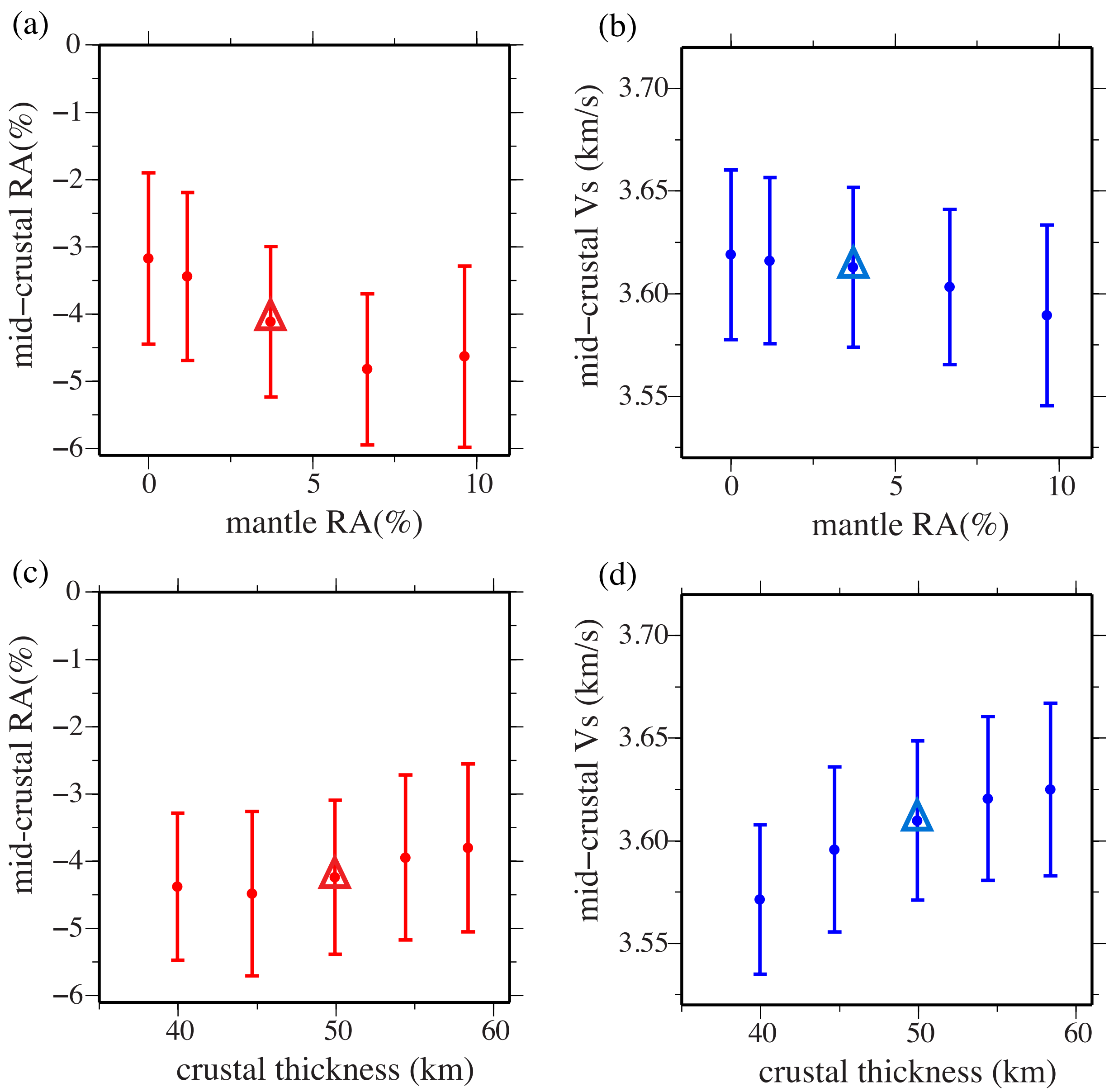

(a)
mid−crustal RA(%)
0
−1
−2
−3
−4
−5
−6
0
5
10
mantle RA(%)
(b)
mid−crustal Vs (km/s)
3.70
3.65
3.60
3.55
0
5
10
mantle RA(%)
(c)
mid−crustal RA(%)
0
−1
−2
−3
−4
−5
−6
40
50
60
crustal thickness (km)
(d)
mid−crustal Vs (km/s)
3.70
3.65
3.60
3.55
40
50
60
crustal thickness (km)

Figure 17

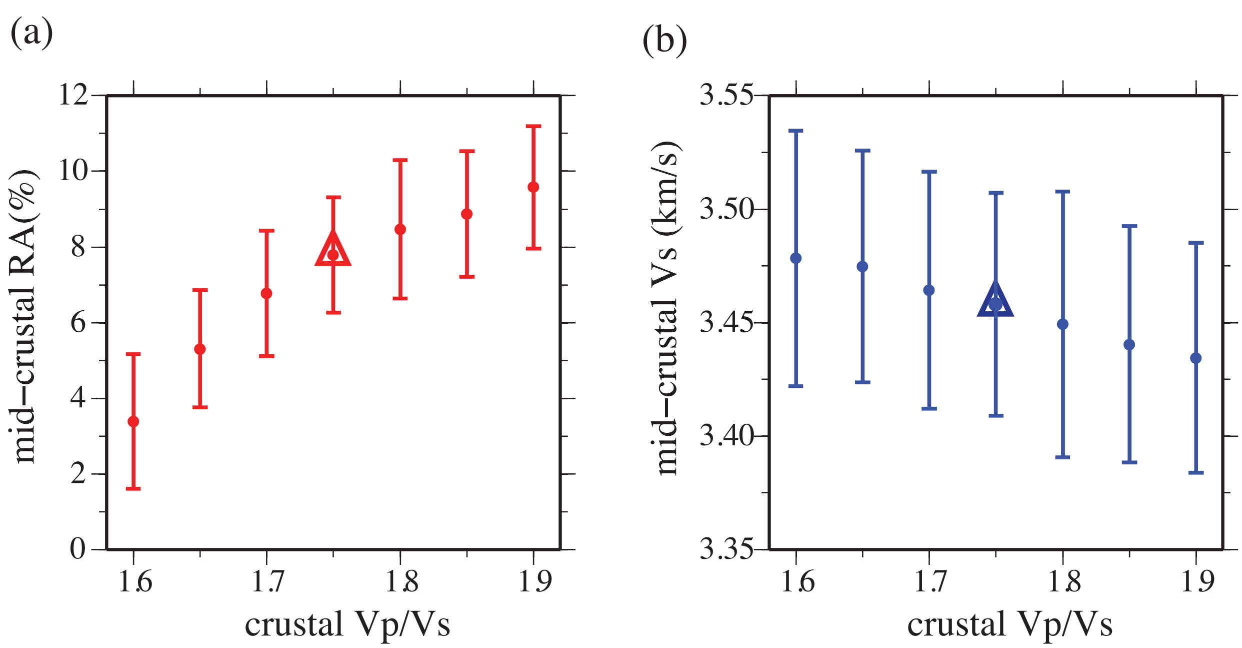

(a)
12
10
8
6
4
2
0
mid−crustal RA(%)
1.6
1.7
1.8
1.9
crustal Vp/Vs
(b)
3.55
3.50
3.45
3.40
3.35
mid−crustal Vs (km/s)
1.6
1.7
1.8
1.9
crustal Vp/Vs

Figure 18

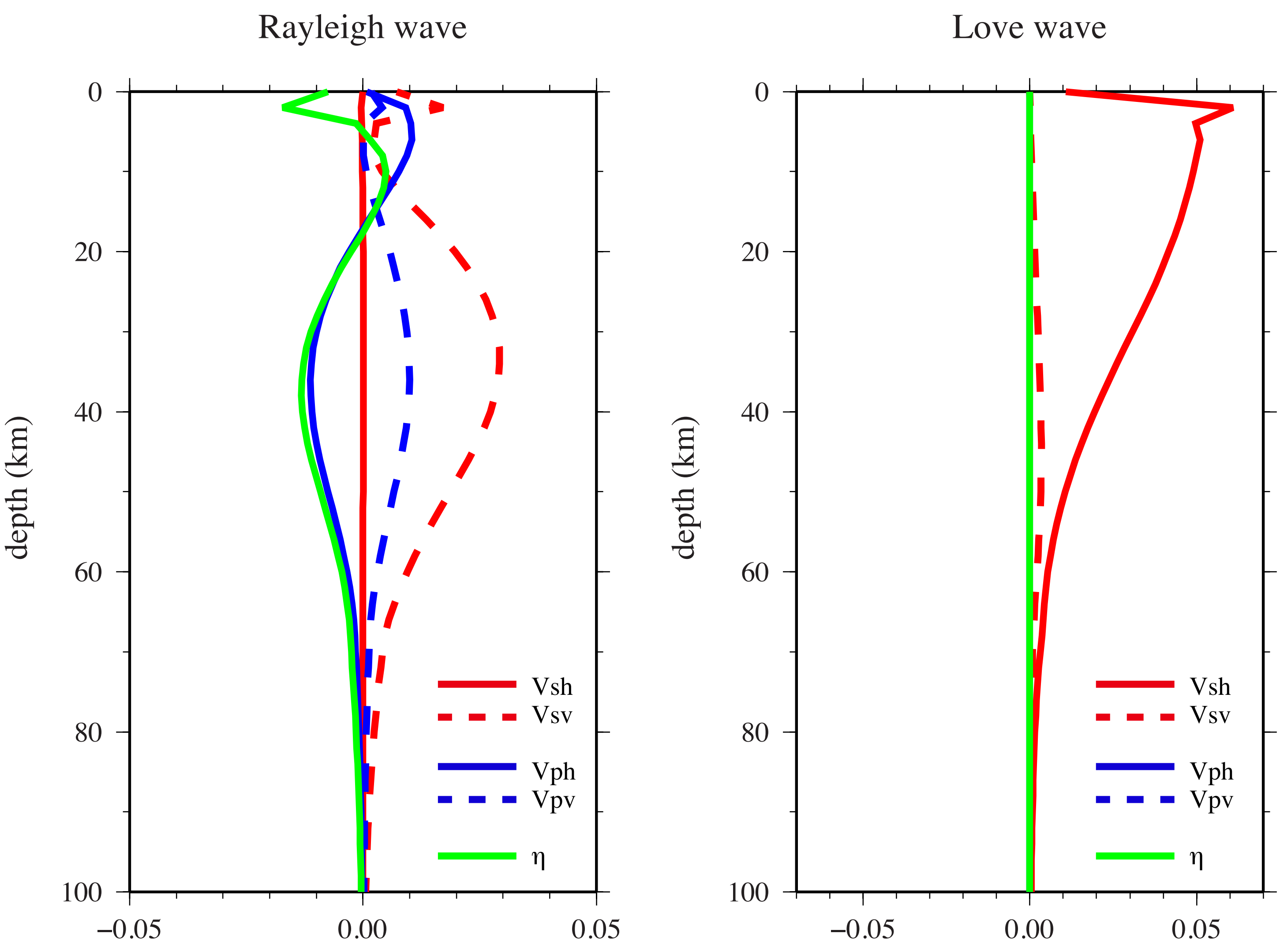
Rayleigh wave
Love wave
depth (km)
0
20
40
60
80
100
−0.05
0.00
0.05
Vsh
Vsv
Vph
Vpv
η

Figure 19

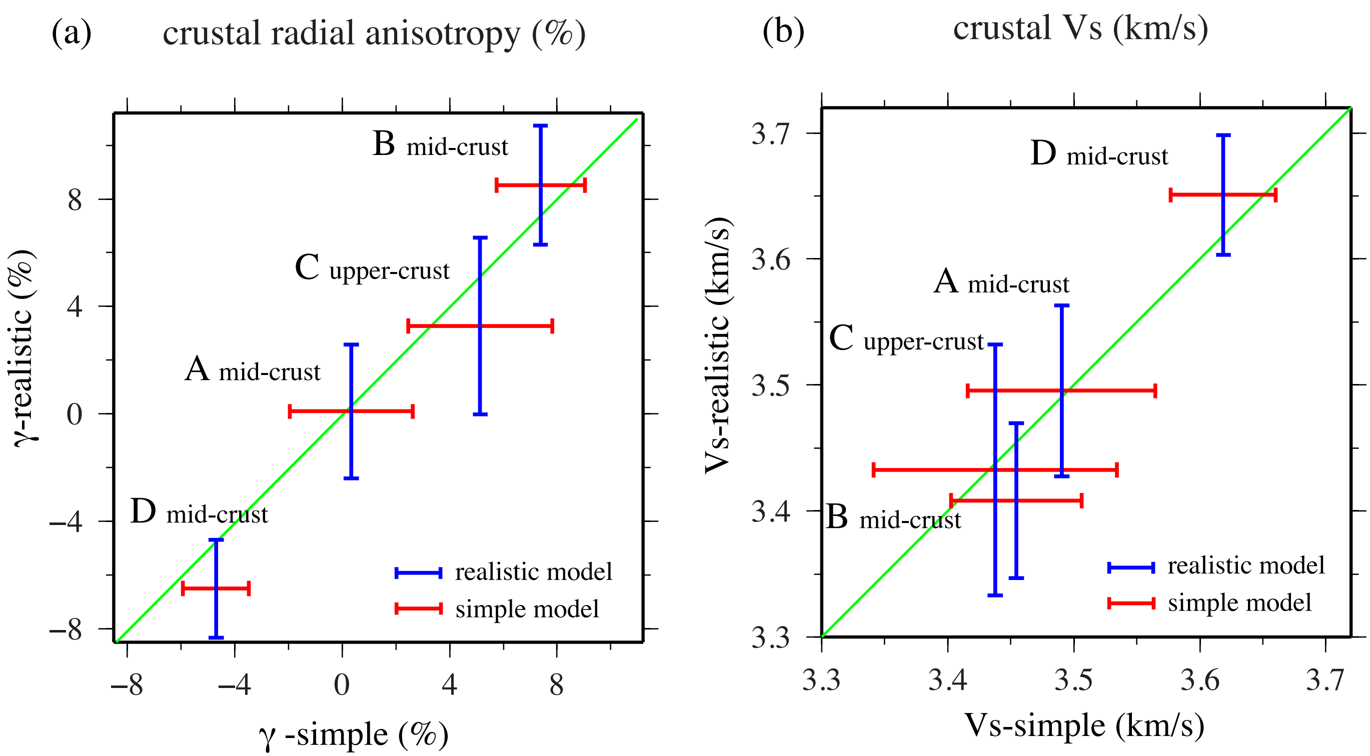
(a)
crustal radial anisotropy (%)
B mid-crust
C upper-crust
A mid-crust
D mid-crust
realistic model
simple model
γ-realistic (%)
γ -simple (%)
8
4
0
−4
−8
(b)
crustal Vs (km/s)
D mid-crust
A mid-crust
C upper-crust
B mid-crust
realistic model
simple model
Vs-realistic (km/s)
Vs-simple (km/s)
3.3
3.4
3.5
3.6
3.7

Figure 20

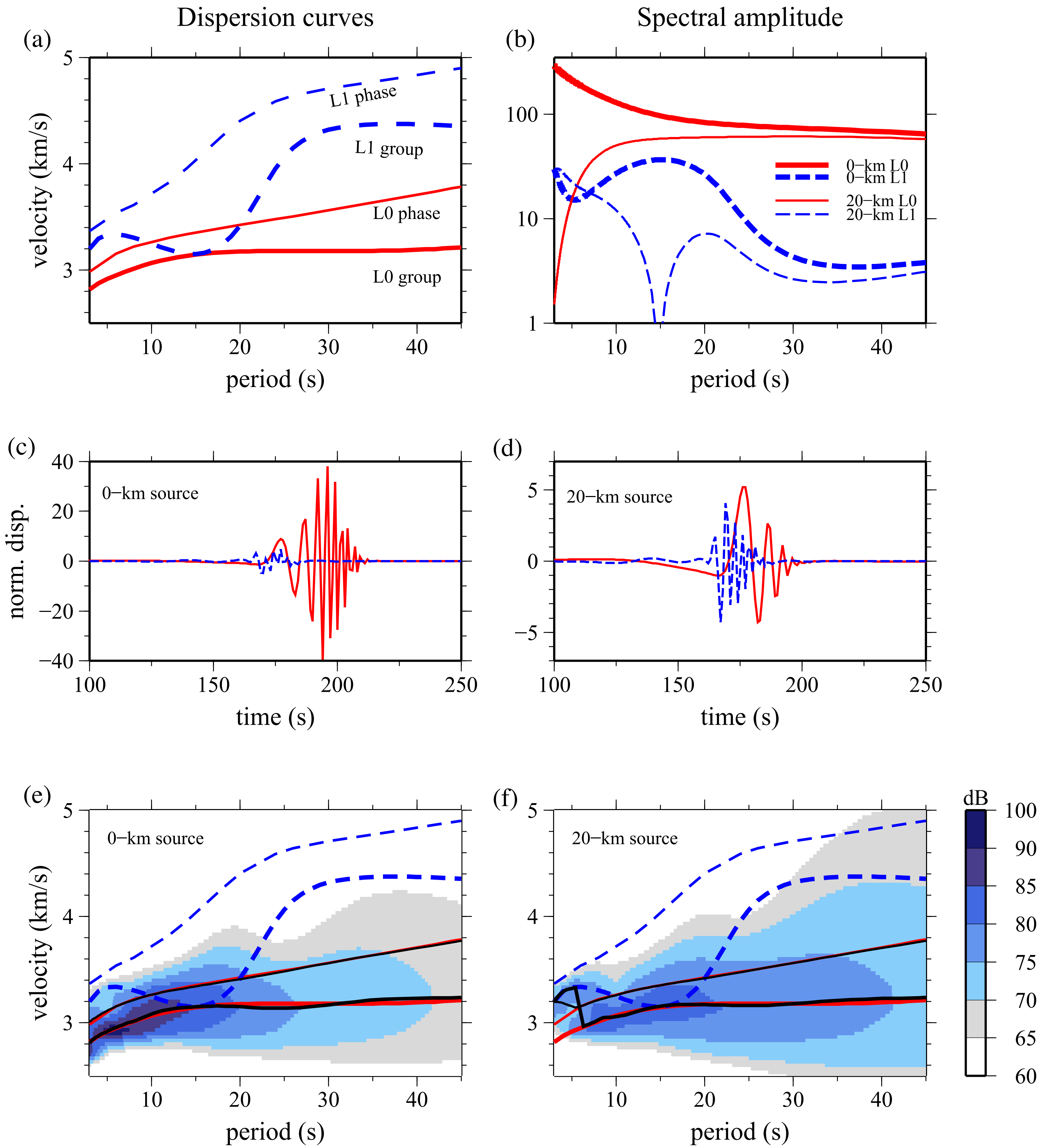

Dispersion curves
Spectral amplitude
(a)
(b)
velocity (km/s)
L1 phase
L1 group
L0 phase
L0 group
period (s)
0−km L0
0−km L1
20−km L0
20−km L1
(c)
(d)
norm. disp.
0−km source
20−km source
time (s)
(e)
(f)
velocity (km/s)
0−km source
20−km source
period (s)
dB

Figure 21

(a)

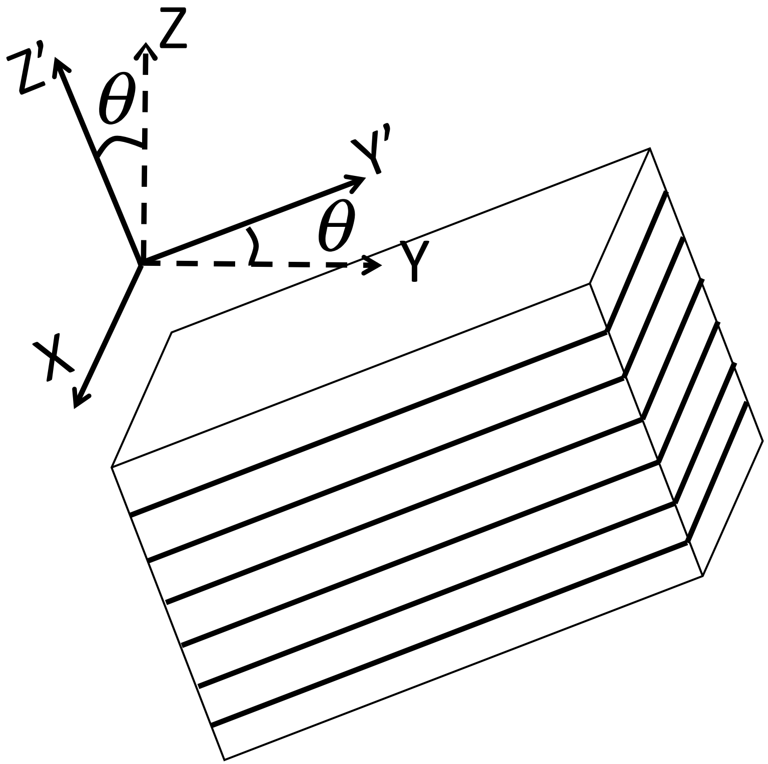

Z'
Z
θ
Y'
θ
Y
X

(b)

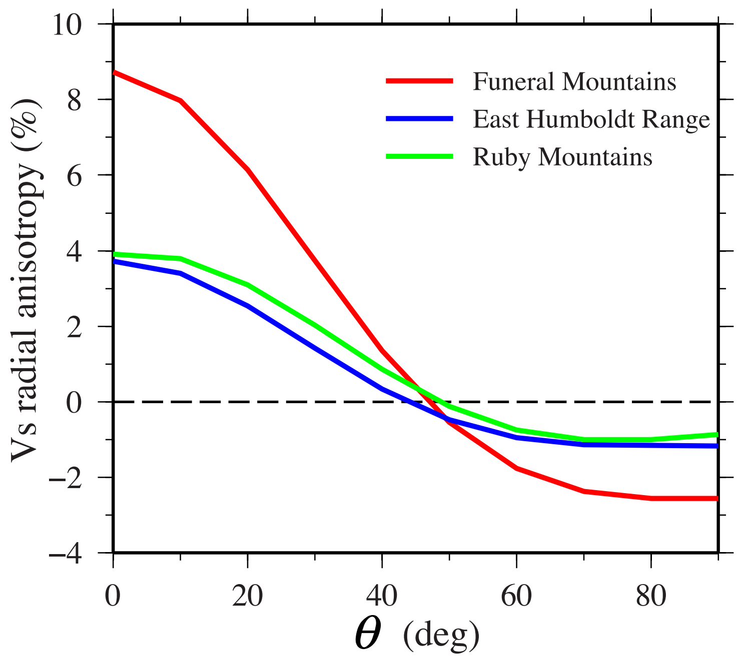

Funeral Mountains
East Humboldt Range
Ruby Mountains
Vs radial anisotropy (%)
θ (deg)
10
8
6
4
2
0
−2
−4
0
20
40
60
80

Figure 1

(a)

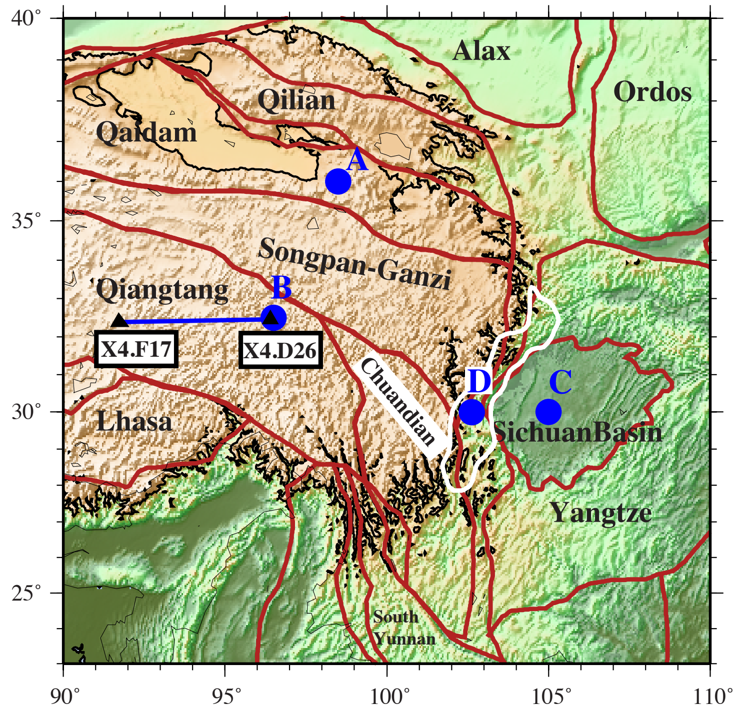

(b)

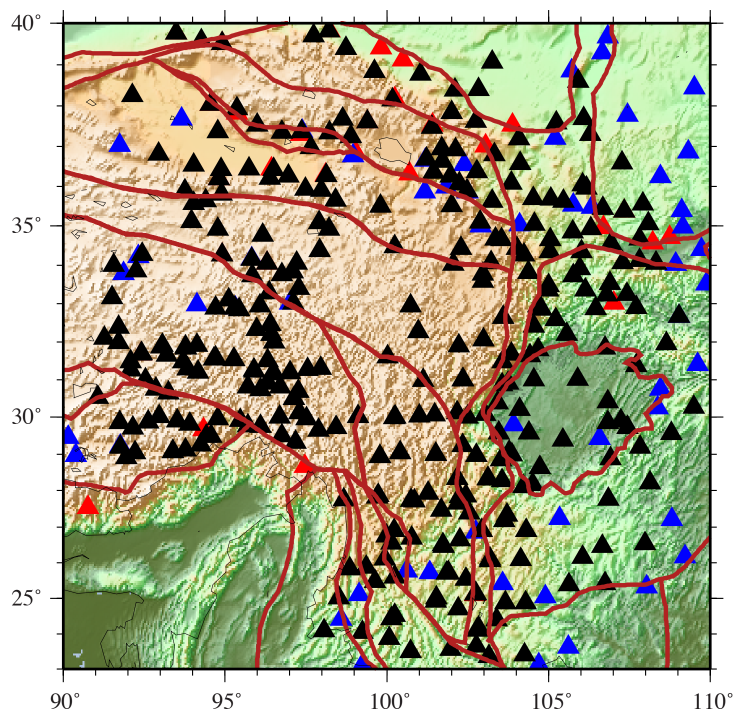

Figure 1. (a) Reference map of the study region in which red lines indicate the boundaries of major geological units and basins [*Zhang et al*., 1984, 2003]. The white contour outlines what we refer to as the Longmenshan region. The blue line is the path between stations X4.F17 and X4.D26 referenced in Fig. 2. Points A, B, C, and D indicate sample points referenced in Figs. 6, 7, 13, 16, and 17. (b) Locations of seismic stations used in this study. Red and black triangles are stations used to measure Love wave dispersion, while blue and black triangles indicate stations used for Rayleigh wave measurements.

Figure 2

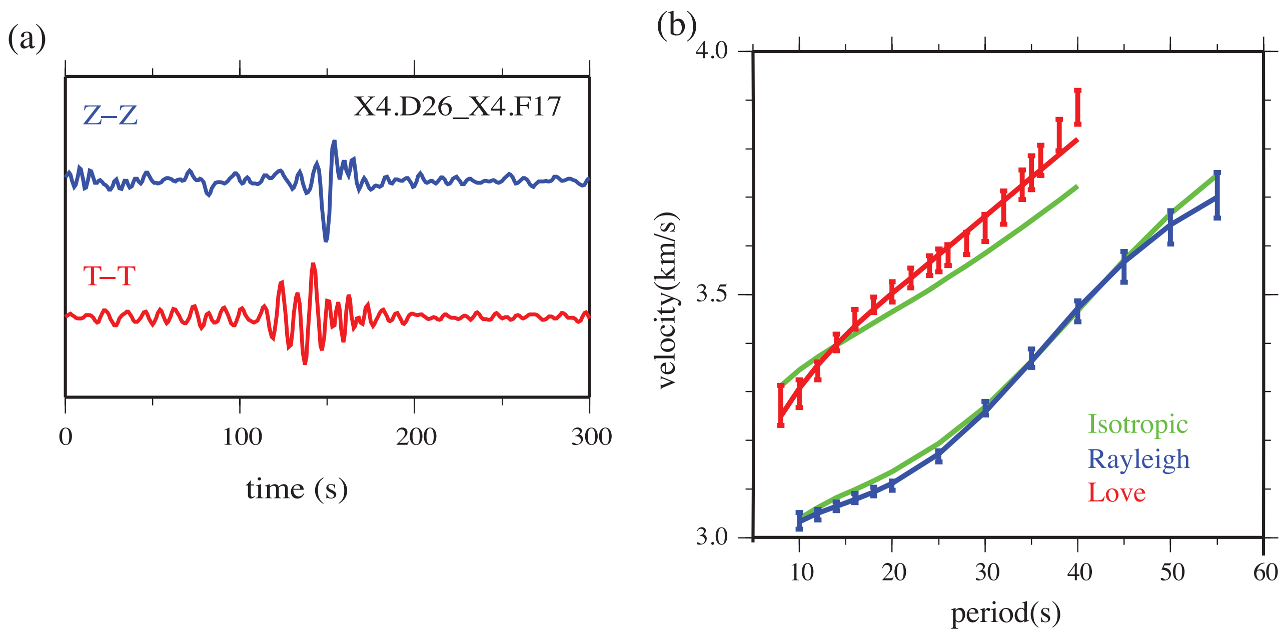

Figure 2. (a) Example of Rayleigh wave (blue, vertical-vertical, Z-Z) and Love wave (red, transverse-transverse, T-T) cross-correlations for a pair of stations (X4.F17, X4.D26) located in the Qiangtang terrane (Fig. 1a), band pass filtered between 5 and 100 sec period. (b) Observed Rayleigh and Love wave phase speed curves measured from the cross-correlations are presented as 1 standard deviation (1σ) error bars (red-Love, blue-Rayleigh). Inverting these data for an isotropic model (Vs = Vsh = Vsv) produces the best fitting green curves, which demonstrates a systematic misfit to the data (predominantly the Love waves) and a Rayleigh-Love discrepancy. Allowing crustal anisotropy (Vsh ≠ Vsv), produces the blue and red dispersion curves that fit the data.

Figure 3

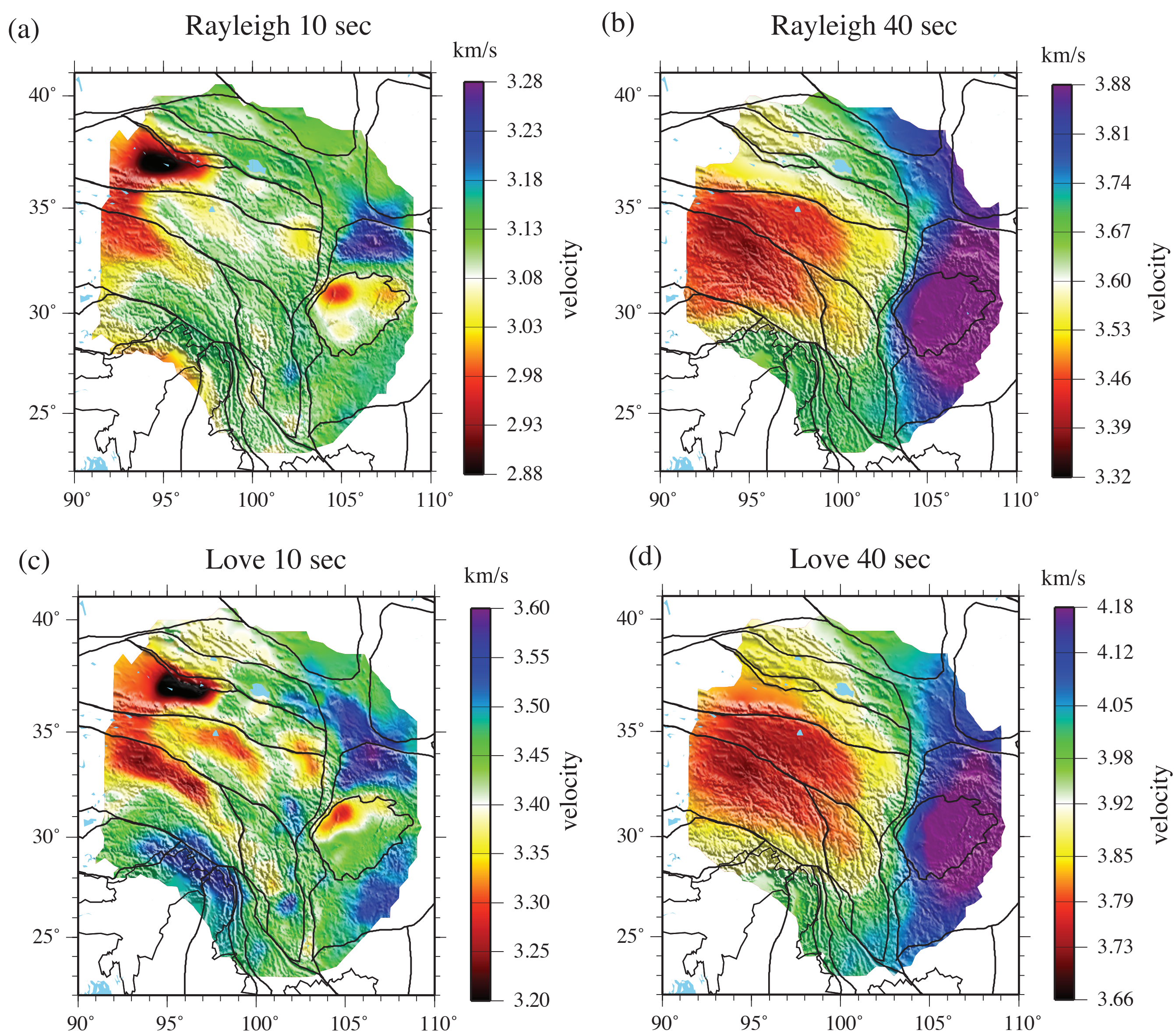

Figure 3. Example estimated Rayleigh (a,b) and Love (c,d) wave phase speed maps at 10 (a,c) and 40 sec (b,d) period determined from ambient noise cross-correlations.

Figure 4

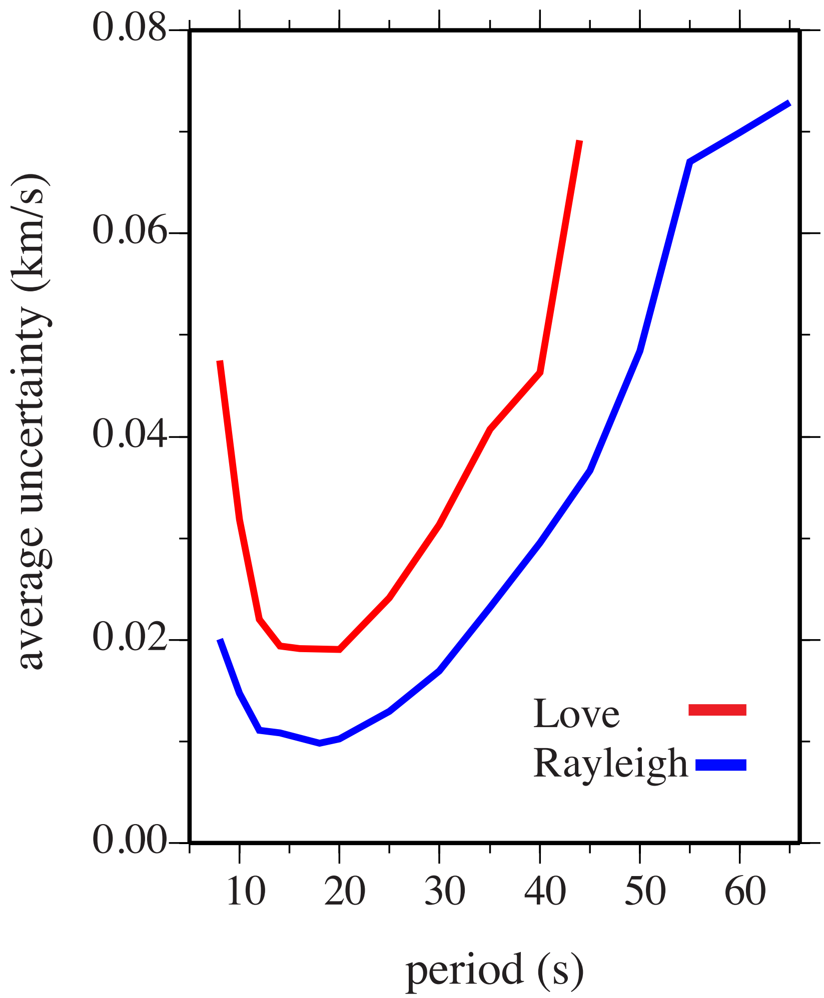

Figure 4. Uncertainties (1σ) in the Rayleigh and Love wave phase speed maps averaged across the study region estimated using the eikonal tomography method of *Lin et al*.[2009].

Figure 5

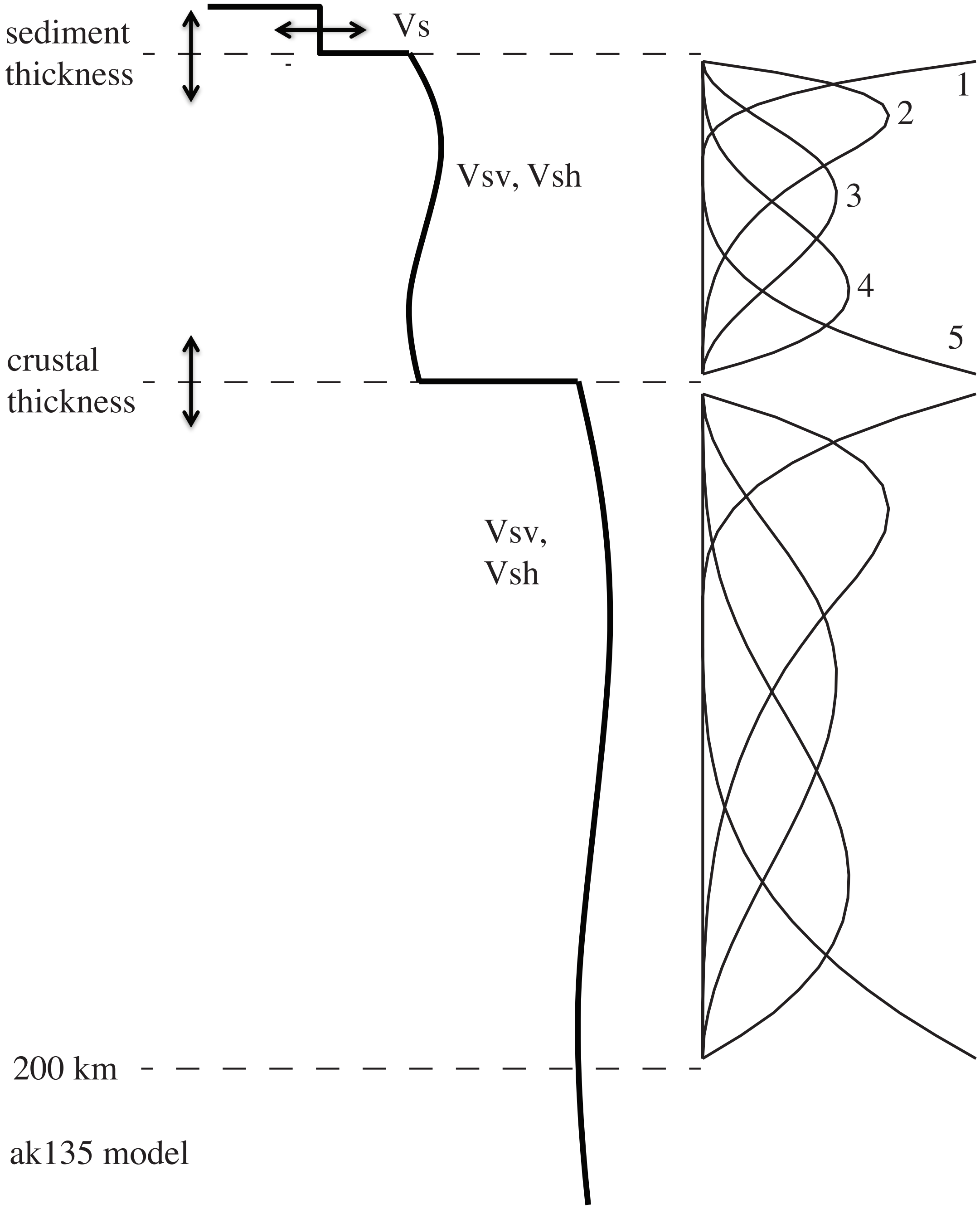

Figure 5. Representation of the parameterization used across the study region. In the crust, five B-splines (1-5) are used to represent Vsv, but three B-splines (2-4) are used to represent Vsh. In the mantle, five B-splines are estimated for Vsv but Vsh is derived from the strength of radial anisotropy in the model of *Shapiro and Ritzwolle*r [2002]. A total of 16 parameters represent the model at each spatial location.

Figure 6

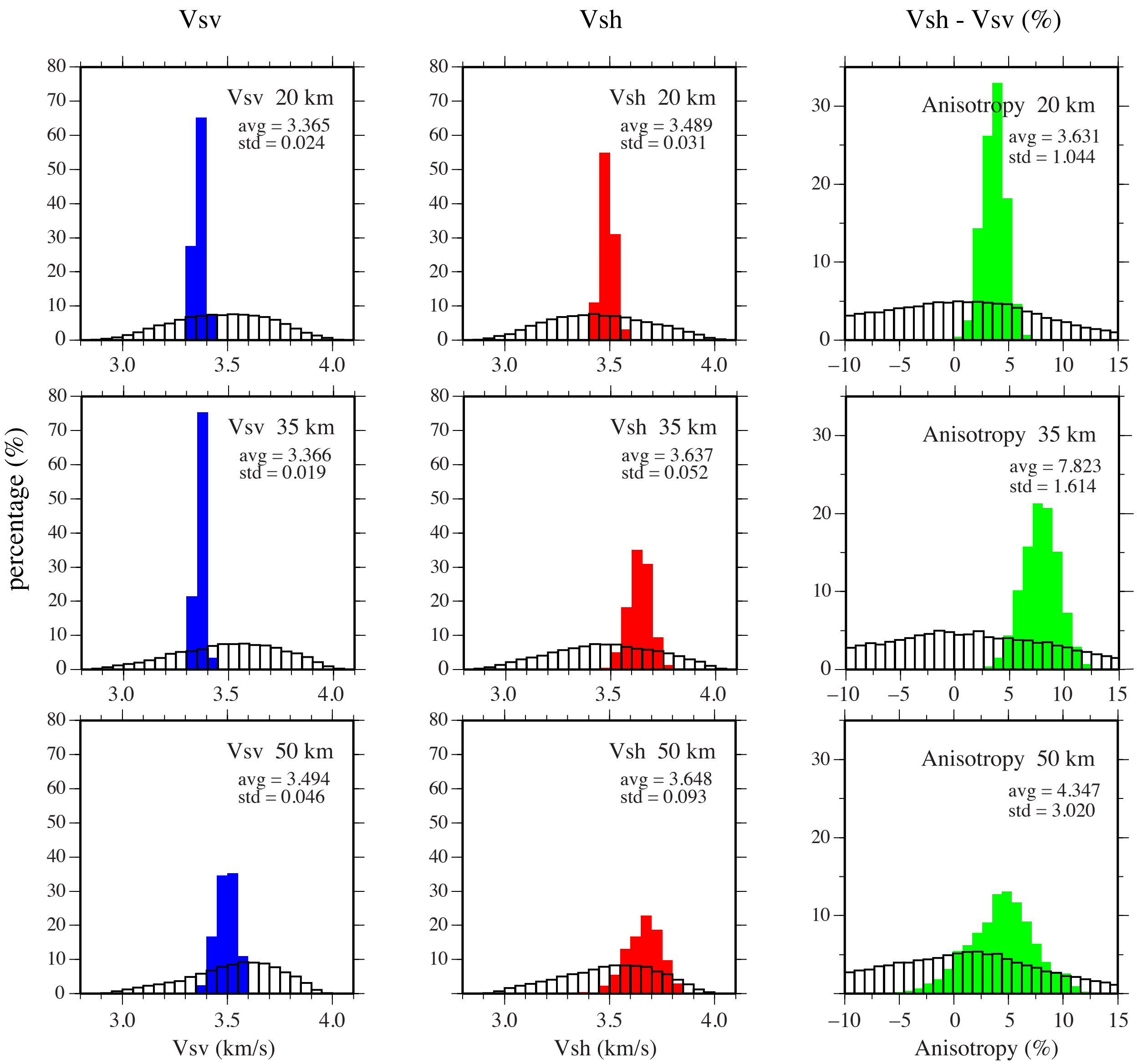

Figure 6. Prior (white histograms) and posterior distributions for Vsv (blue), Vsh (red) and radial anisotropy (green, (Vsh-Vsv)/Vs, in percent) at 20, 35, and 50 km depth for point B in the Qiangtang terrane (Fig. 1a). The mean and standard deviation for each posterior distribution are shown in each panel.

Figure 7

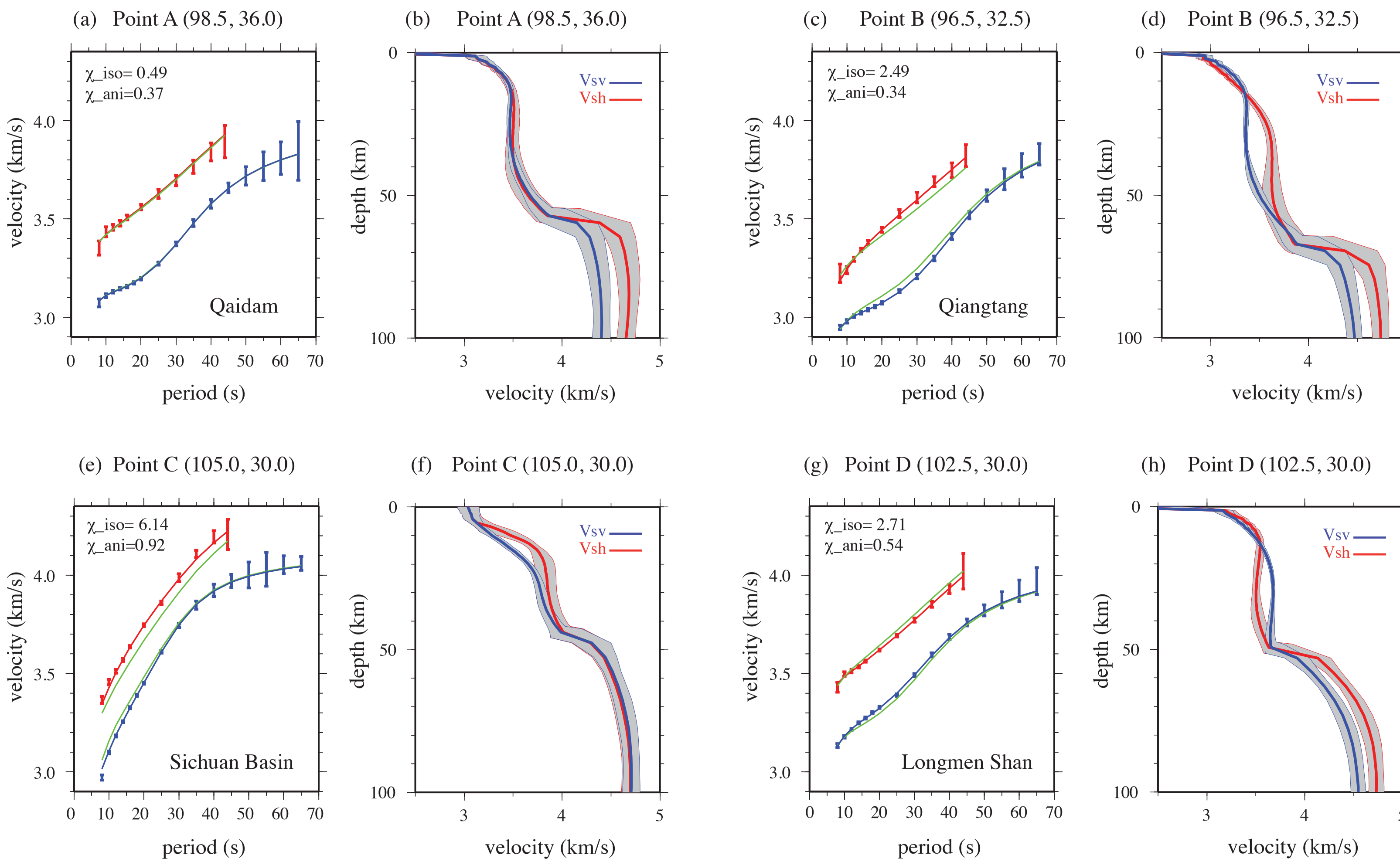

Figure 7. Examples of dispersion curves and estimated radially anisotropy for four spatial locations (A, B, C, D) identified in Fig. 1a. (a) Point A (98.5, 36.0) near the eastern edge of the Qaidam Basin. Local Rayleigh and Love wave phase speed curves presented as one standard deviation (1σ) error bars. Predictions from the average of the anisotropic model distribution in (b) are shown as solid lines and green lines are predictions from the Voigt-averaged isotropic Vs model. Misfits (defined as $\chi=\sqrt{(S/N)}$ where S is defined in Eq. 3) correlated with anisotropic and isotropic models are shown at the upper left corner. (b) Point A (cont.). Inversion result in which the one standard deviation (1σ) model distributions are shown with the grey corridors for Vsh and Vsv, with the average of each ensemble plotted with bold blue (Vsv) and red (Vsh) lines. The model ensembles are nearly coincident in the crust, consistent with an isotropic crust. (c) & (d) Point B (96.5, 32.5) in the Qiangtang terrane where the central crust has strong positive radial anisotropy between 20 and 50 km depth and weak negative anisotropy above about 15 km depth. (e) & (f) Point C (105.0, 30.0) in the Sichuan Basin where the central crust has strong positive radial anisotropy between depths of 10 and 25 km. (g) & (h) Point D (102.5, 30.0) between Tibet and the Sichuan Basin where the central crust has strong negative radial anisotropy between 20 and 50 km depth.

Figure 8

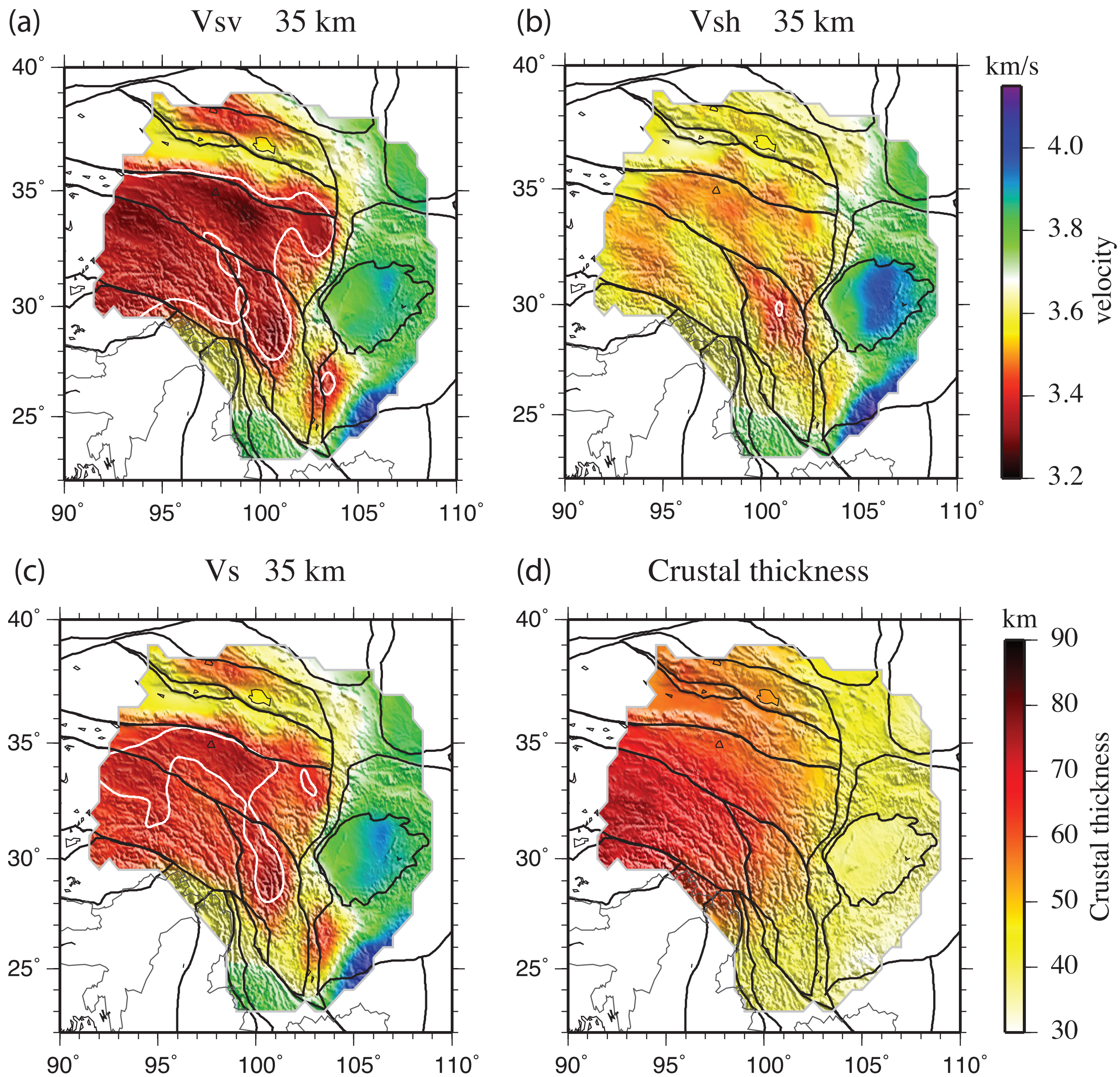

Figure 8. The average of the posterior distributions of (a) Vsv, (b) Vsh, and (c) Vs at 35 km depth in km/s, which is in the middle crust beneath the Tibetan Plateau. Regions with very low velocities (<3.4 km/s) are encircled by white contours. (d) The average of the posterior distribution of crustal thickness in km.

Figure 9

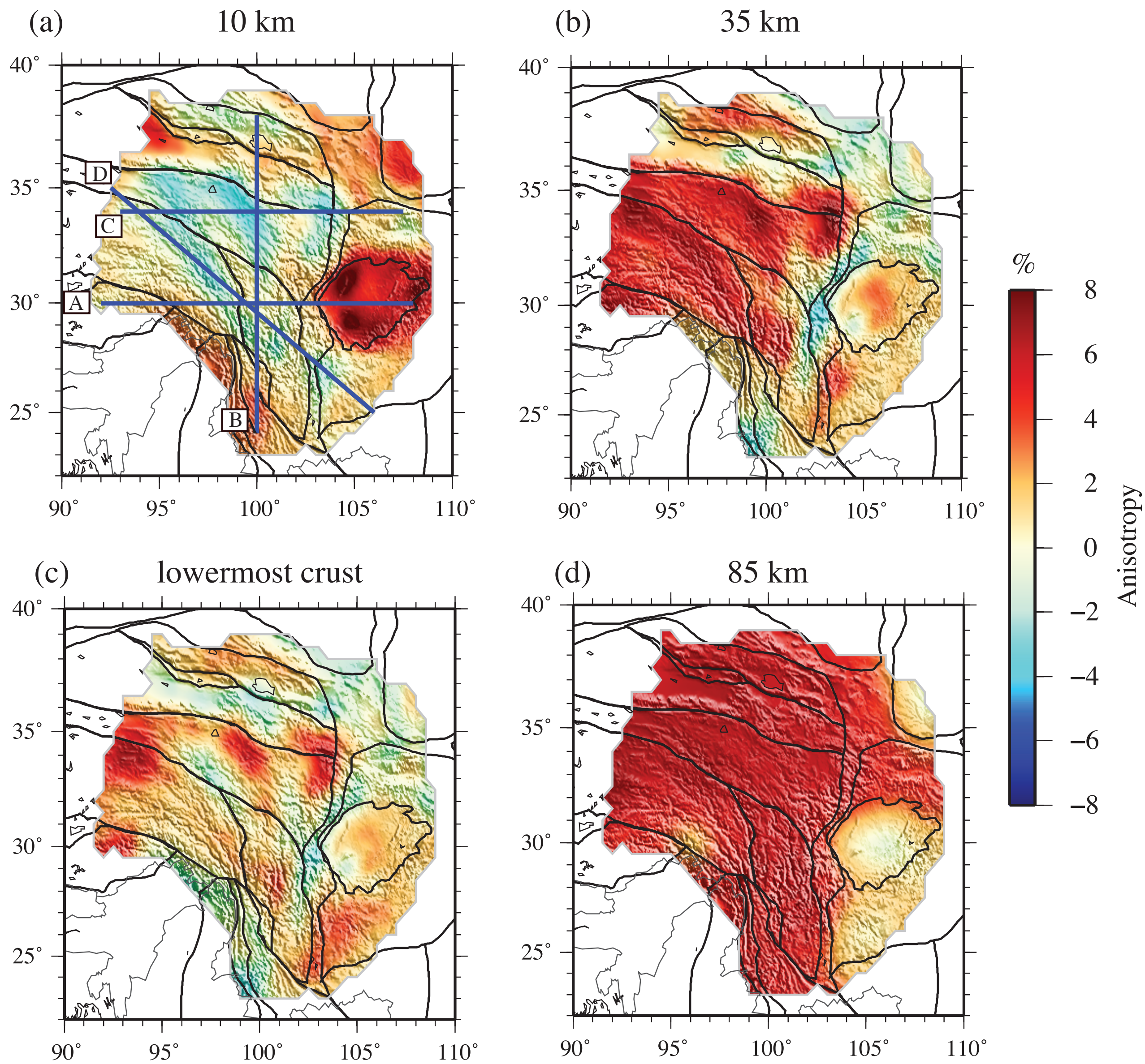

Figure 9. Maps of the mean of the posterior distribution for estimates of radial anisotropy at (a) 10 km depth, (b) 35 km depth, and (c) 90% of the depth to Moho in the lowermost crust. Radial anisotropy units are the percent difference between Vsh and Vsv at each location and depth: (Vsh-Vsv)/Vs, where Vs is the Voigt-averaged shear wave speed. Blue lines in (a) identify the locations of the vertical cross-sections in Fig. 10.

Figure 10

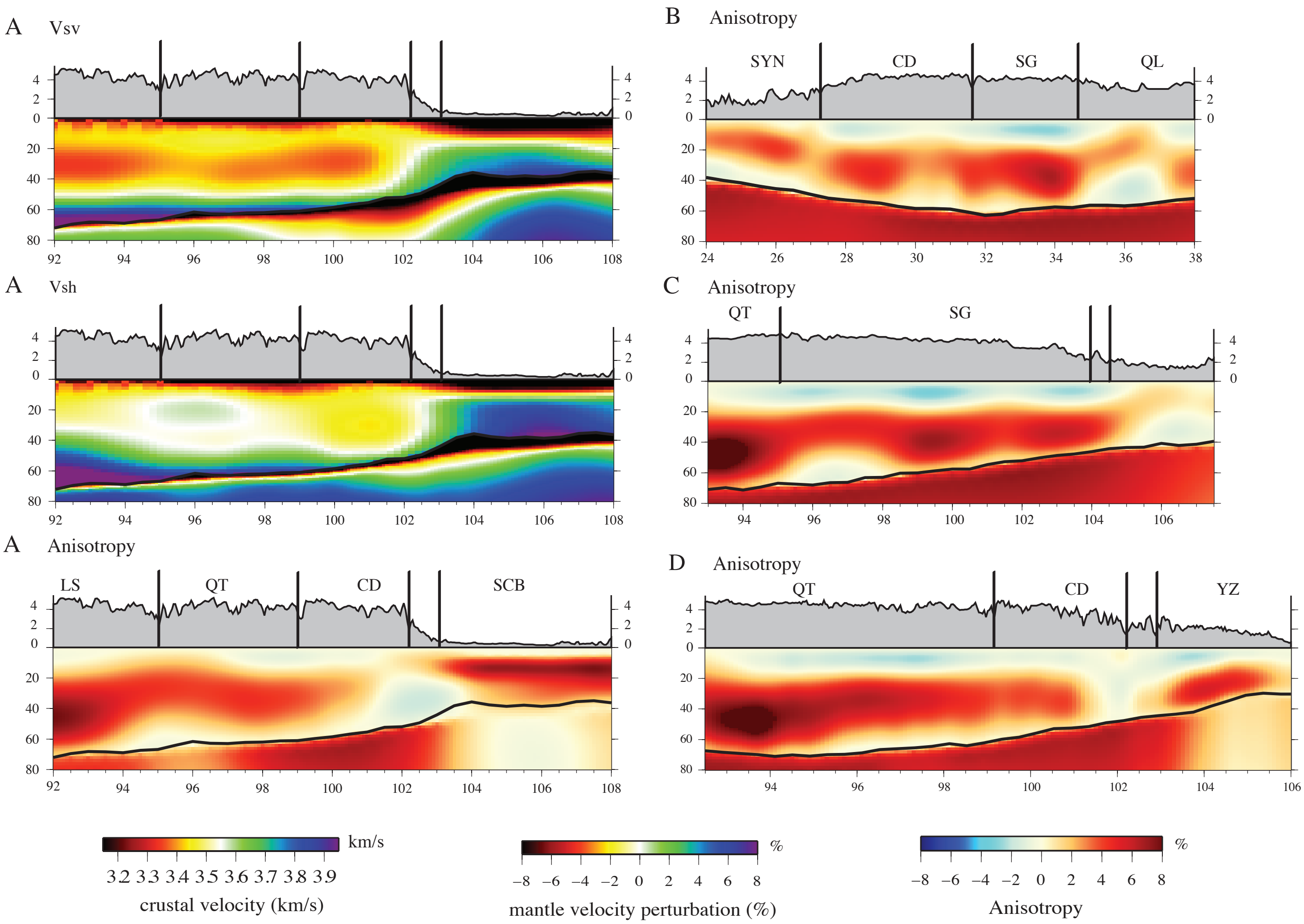

Figure 10. Vertical cross-sections of (upper left) Vsv, (middle left) Vsh, and (lower left) radial anisotropy along profile A (Fig. 9a), taken from the mean of the posterior distribution at each location and depth. Topography is shown at the top of each panel as are locations of geological-block boundaries (SG: Songpan-Ganzi terrane, CD: Chuandian terrane, LS: Lhasa terrane, QL: Qilian terrane, SCB: Sichuan Basin, SYN: South Yunnan region, YZ: Yangtze craton). Crustal shear velocities are presented in absolute units (km/s), radial anisotropy is presented as the percent difference between Vsh and Vsv ((Vsh-Vsv)/Vs), and mantle velocities are percentage perturbations relative to 4.4 km/s. (Right) Radial anisotropy is presented beneath profiles B, C, and D (Fig. 9a).

Figure 11

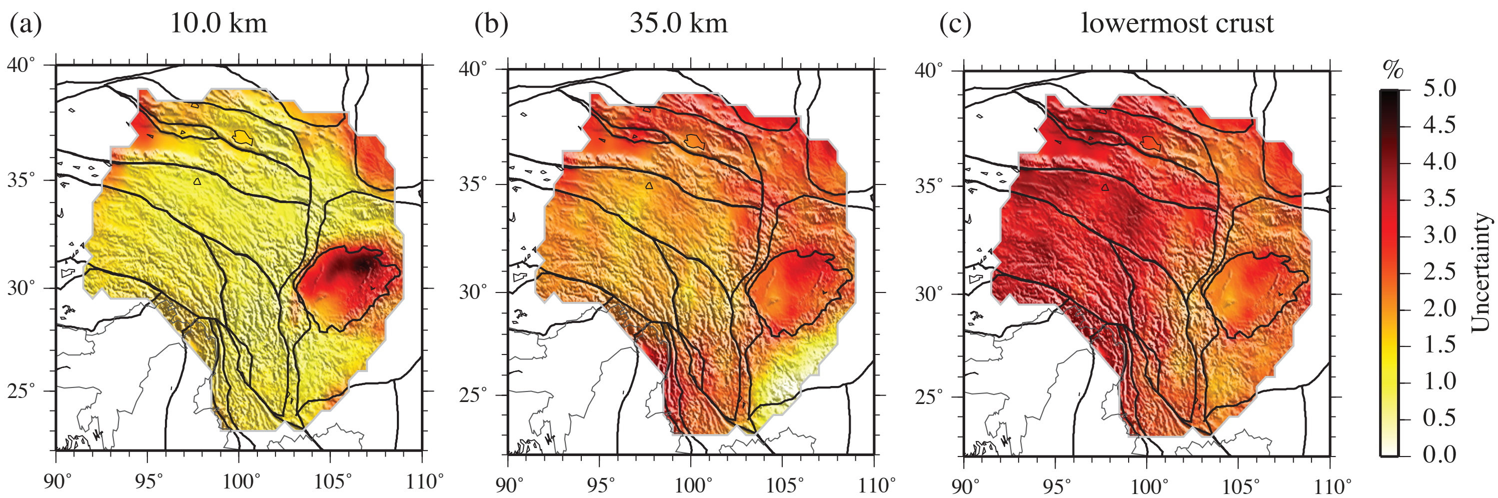

Figure 11. Maps of the one standard deviation (i.e., error) of the posterior distribution for estimates of radial anisotropy at (a) 10 km depth, (b) 35 km depth, and (c) 90% of the depth to Moho. Results are in the same units as radial anisotropy, not in the percentage of radial anisotropy at each point.

Figure 12

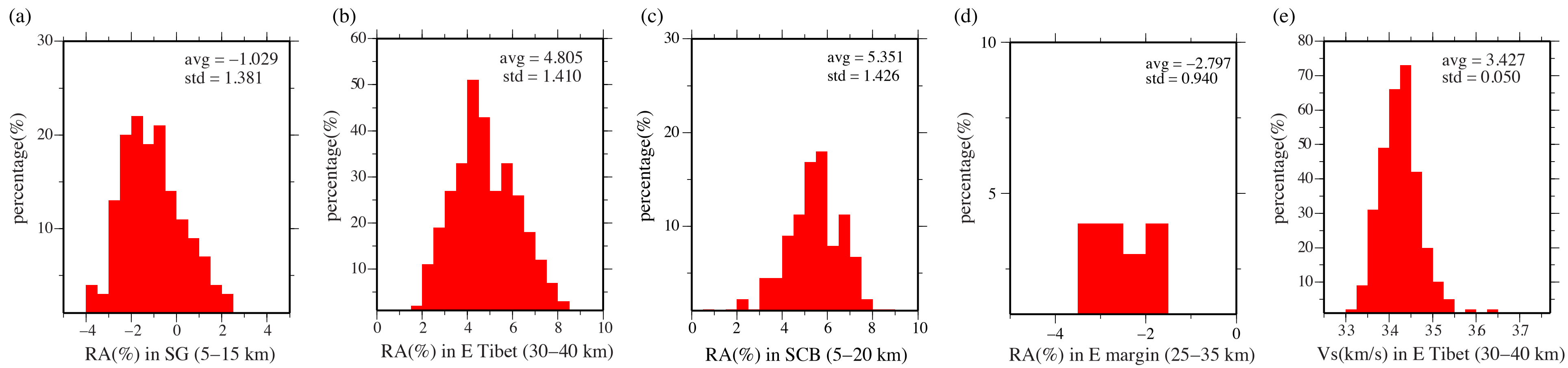

Figure 12. Plots of the spatial distribution of the mean of the posterior distributions of radial anisotropy across (a) the Songpan-Gonzi terrane between depths of 5 and 15 km, (b) eastern Tibet at depths between 30 and 40 km, (c) the Sichuan Basin at depths between 5 and 20 km, and (d) the Longmenshan region between eastern Tibet and the Sichuan Basin between 25 and 35 km. (e) The distribution of the mean of the posterior distribution for Voigt-averaged shear wave speed Vs across eastern Tibet between depths of 30 and 40 km.

Figure 13

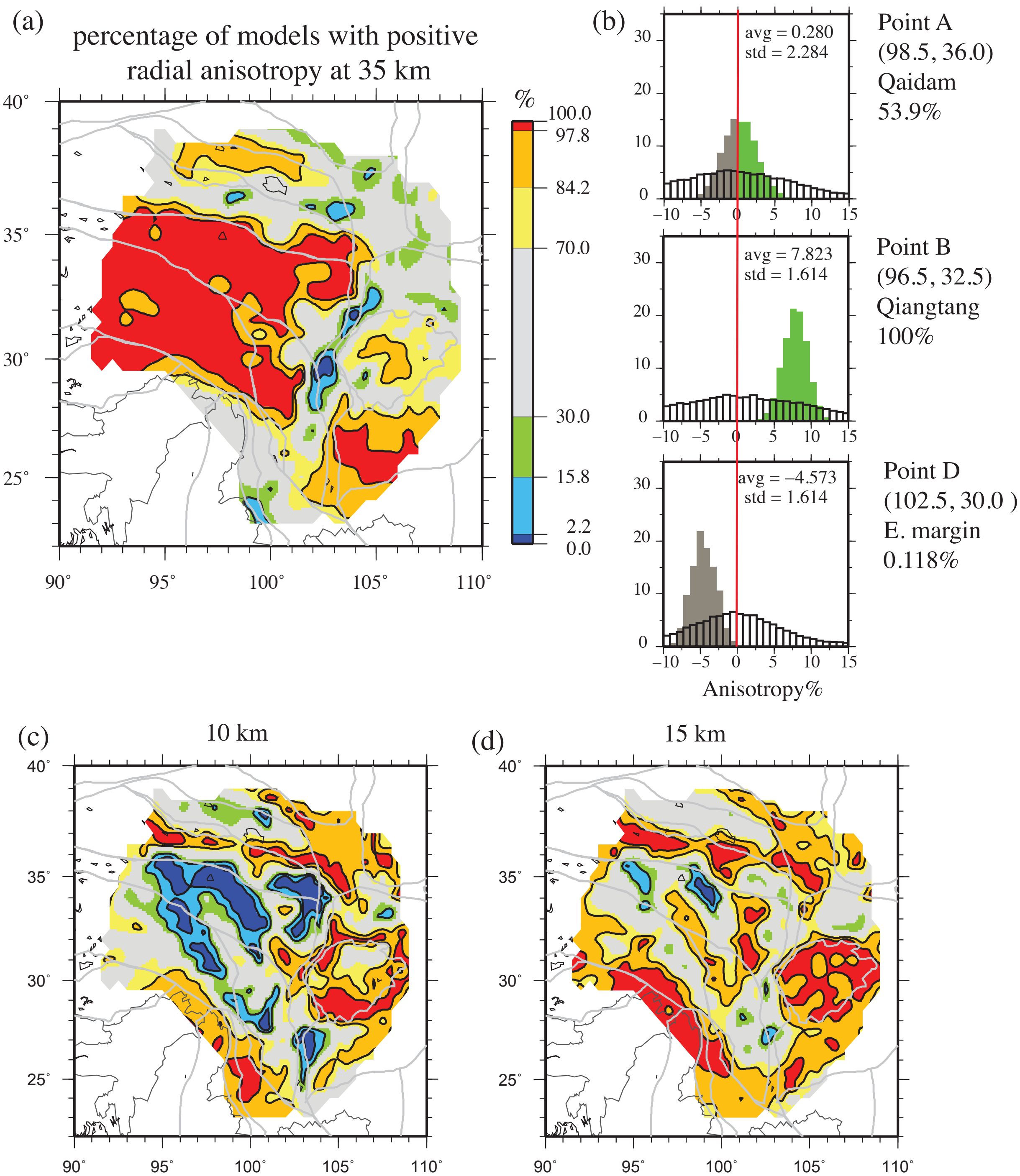

Figure 13. (a) Percent of accepted models at each location with positive radial anisotropy (Vsh > Vsv) at 35 km depth. Values of 2.2%, 15.8%, 84.2%, and 97.8% are contoured by black lines, which are correlated with the position of ±1 σ and ±2 σ in a Gaussian distribution. (b) Prior (white histogram in the background) and posterior (colored histogram) distributions of radial anisotropy ((Vsh-Vsv)/Vs, in percent) at 35 km depth for locations A, B, and D of Fig. 1a. The red line indicates the position of zero radial anisotropy. The percent of models with positive radial anisotropy is indicated to the right of each panel. (c) Same as (a), but for positive radial anisotropy at 10 km depth. (d) Same as (a), but for positive radial anisotropy at 15 km depth.

Figure 14

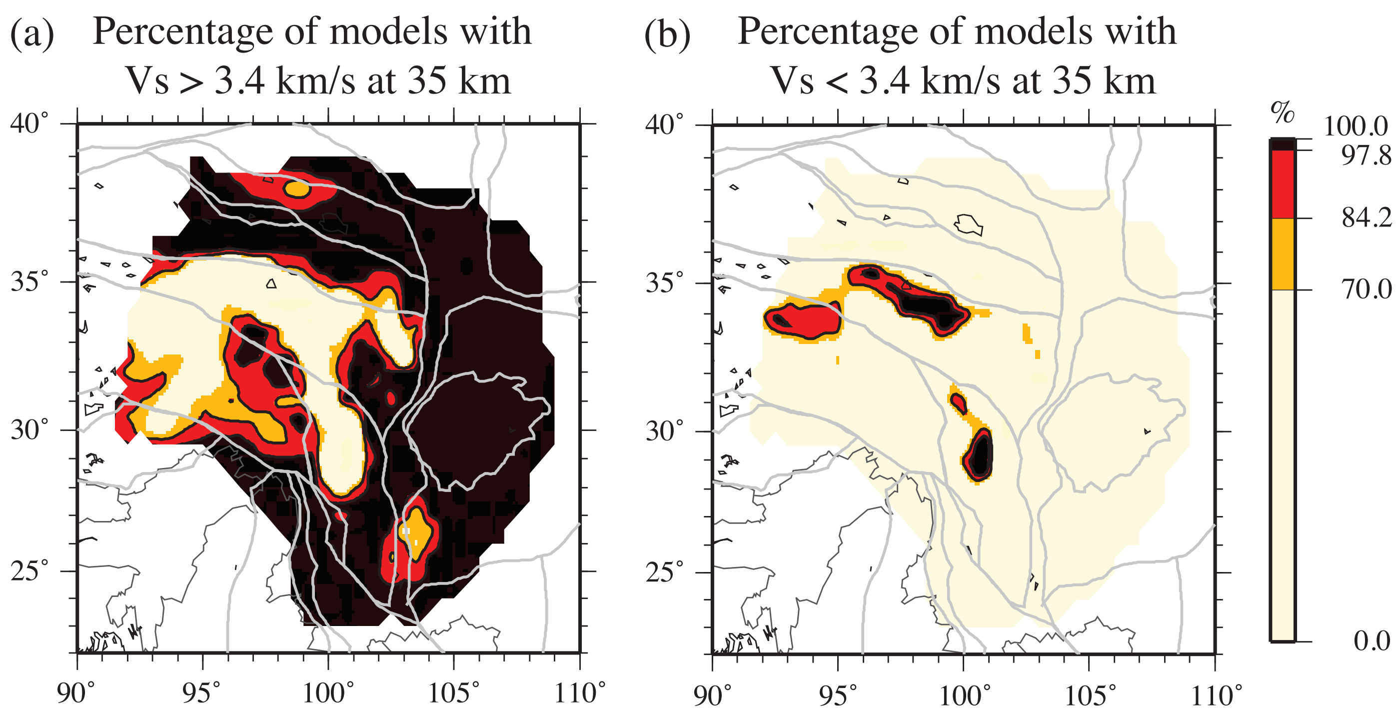

Figure 14. Similar to Fig. 13a, but this figure is the percentage of accepted models at each location with Voigt-averaged Vs > 3.4 km/s at 35 km depth. (b) Same as (a), but for Vs < 3.4 km/s at 35 km depth.

Figure 15

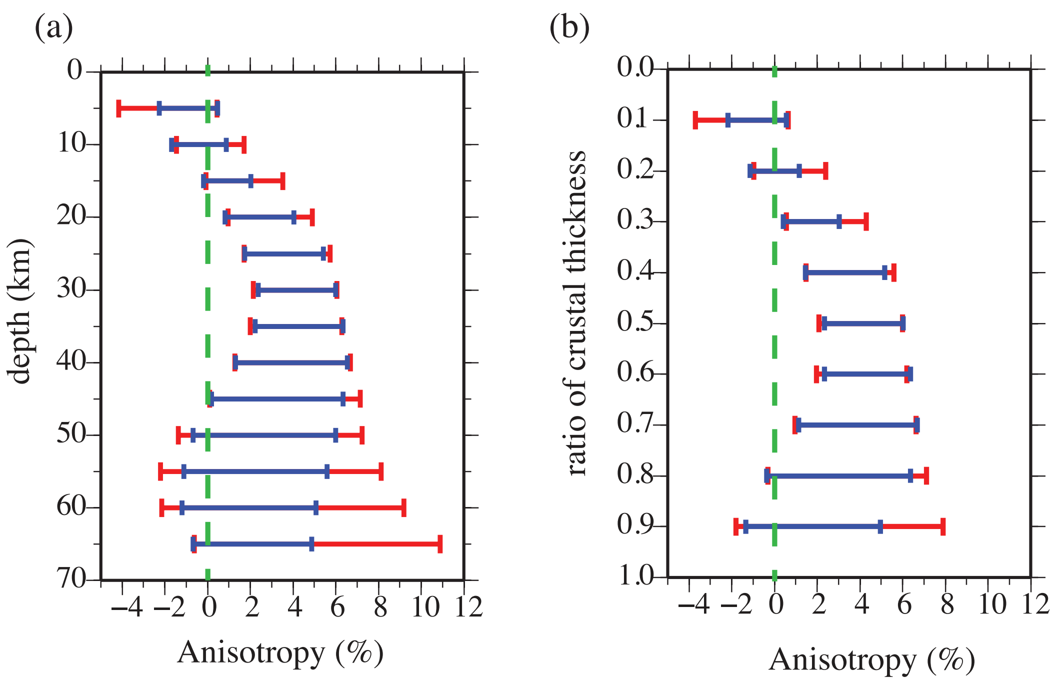

Figure 15. The spatially averaged effect of crustal parameterization of radial anisotropy on the mean and standard deviation of radial anisotropy averaged across the Tibetan crust. Crustal radial anisotropy and uncertainty are presented as error bars as a function of (a) absolute depth and (b) depth measured as a ratio of crustal thickness, averaged over the study region where surface elevation is more than 3 km (black contour in Fig. 1a). The middle of each error bar is the average amplitude of radial anisotropy ((Vsh-Vsv)/Vs, in percent) and the half-width of the error bar is the average one-standard deviation uncertainty. Blue bars result from the more tightly constrained inversion (uppermost and lowermost crust are approximately isotropic, Vsh=Vsv for crustal B-splines 1 and 5 in Fig. 5, but Vsh and Vsv can differ for splines 2 to 4). Red bars are results from the less constrained inversion (radial anisotropy is allowed across the entire crust, Vsv may differ from Vsh for all five crustal B-splines).

Figure 16

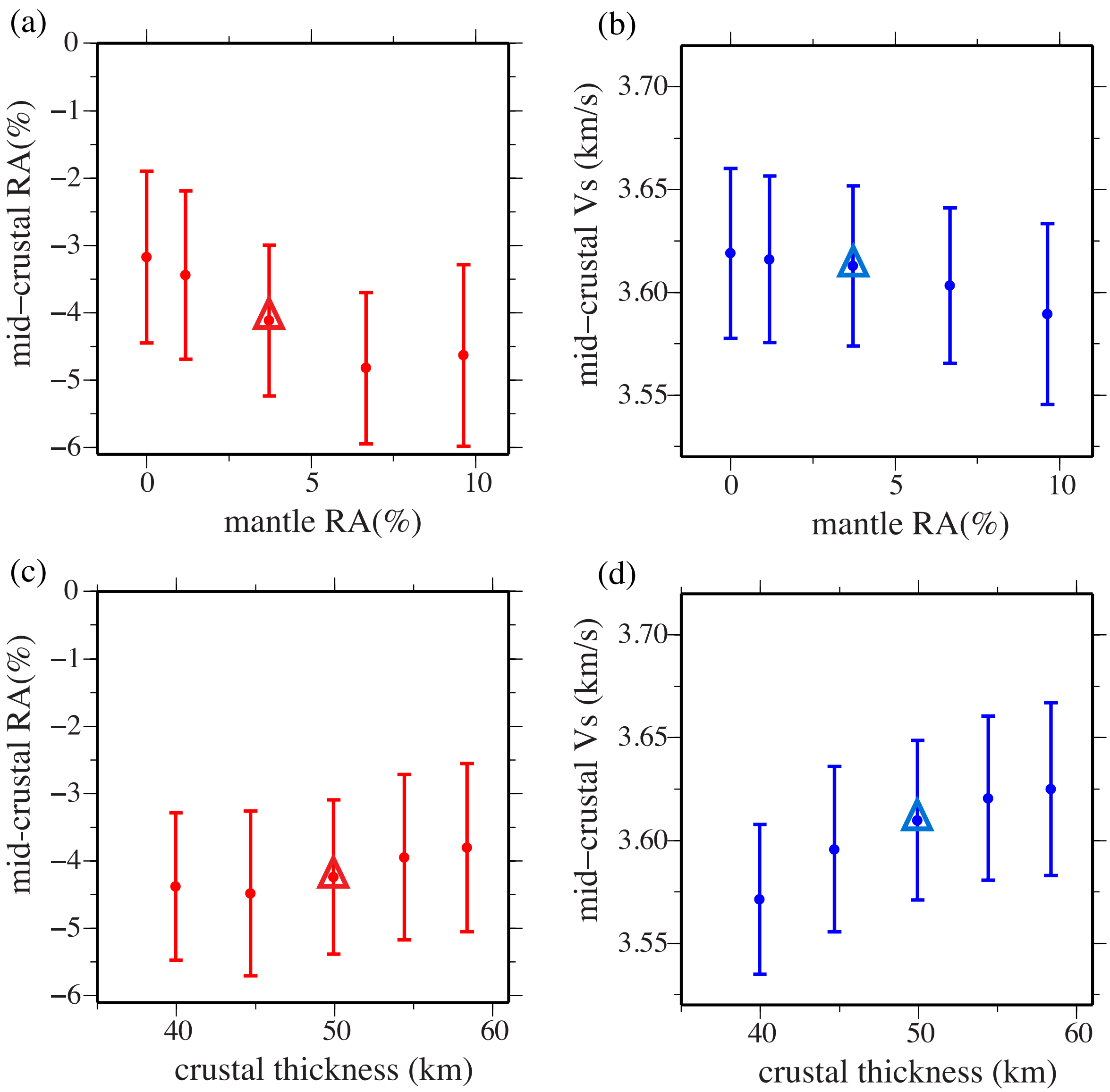

Figure 16. Trade-off between the depth-averaged (from Moho to 150 km) amplitude of mantle radial anisotropy used in the inversion and (a) the depth-averaged (±5 km around the middle crust) mid-crustal radial anisotropy and (b) the depth-averaged (±5 km around the middle crust) mid-crustal Voigt-averaged Vs. Each dot is the depth-averaged value and half-widths of the error bars are the depth-averaged one-standard deviation uncertainty. Both come from the inversion with a given mantle radial anisotropy at location D identified in Fig. 1a. The triangles are the values in our final model. (c)&(d) Similar to (a)&(b), but showing the trade-off between the crustal thickness and (c) the depth-averaged mid-crustal radial anisotropy and (d) the depth-averaged mid-crustal Voigt-averaged Vs.

Figure 17

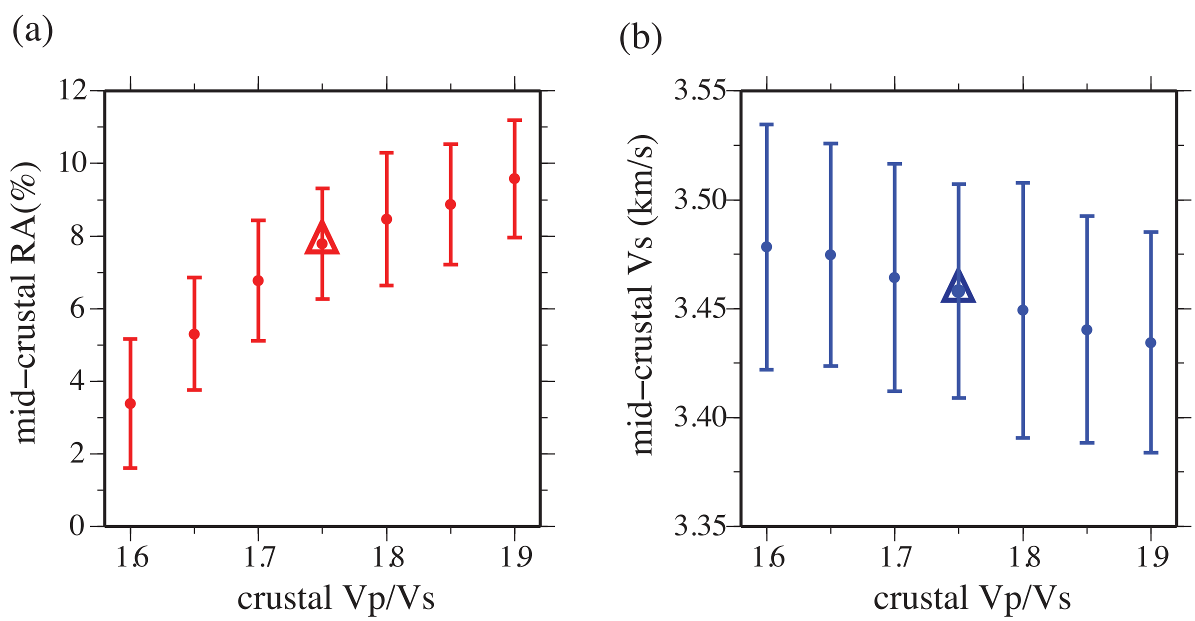

Figure 17. Similar to Fig. 16, but for the trade-off between the fixed value of the crustal Vp/Vs used in the inversion and (a) the depth-averaged (from 30 to 40 km) crustal radial anisotropy and (b) the depth-averaged (from 30 to 40 km) mid-crustal Voigt-averaged Vs. Values are from inversion with a given crustal Vp/Vs at location B identified in Fig. 1a.

Figure 18

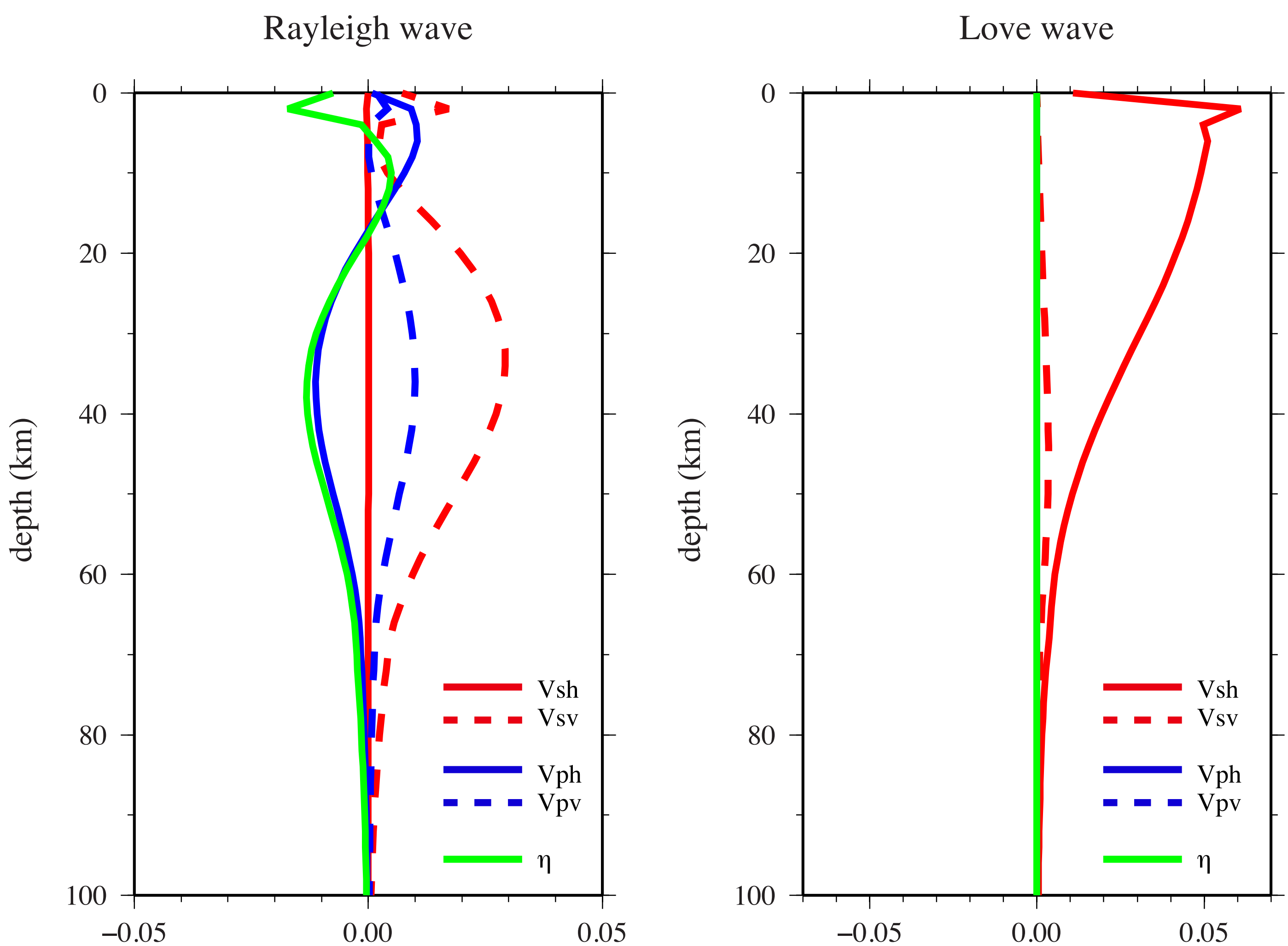

Figure 18. Example sensitivity kernels for Rayleigh and Love wave phase speeds at 30 sec period to perturbations in Vsv, Vsh, Vpv, Vph, and η at different depths.

Figure 19

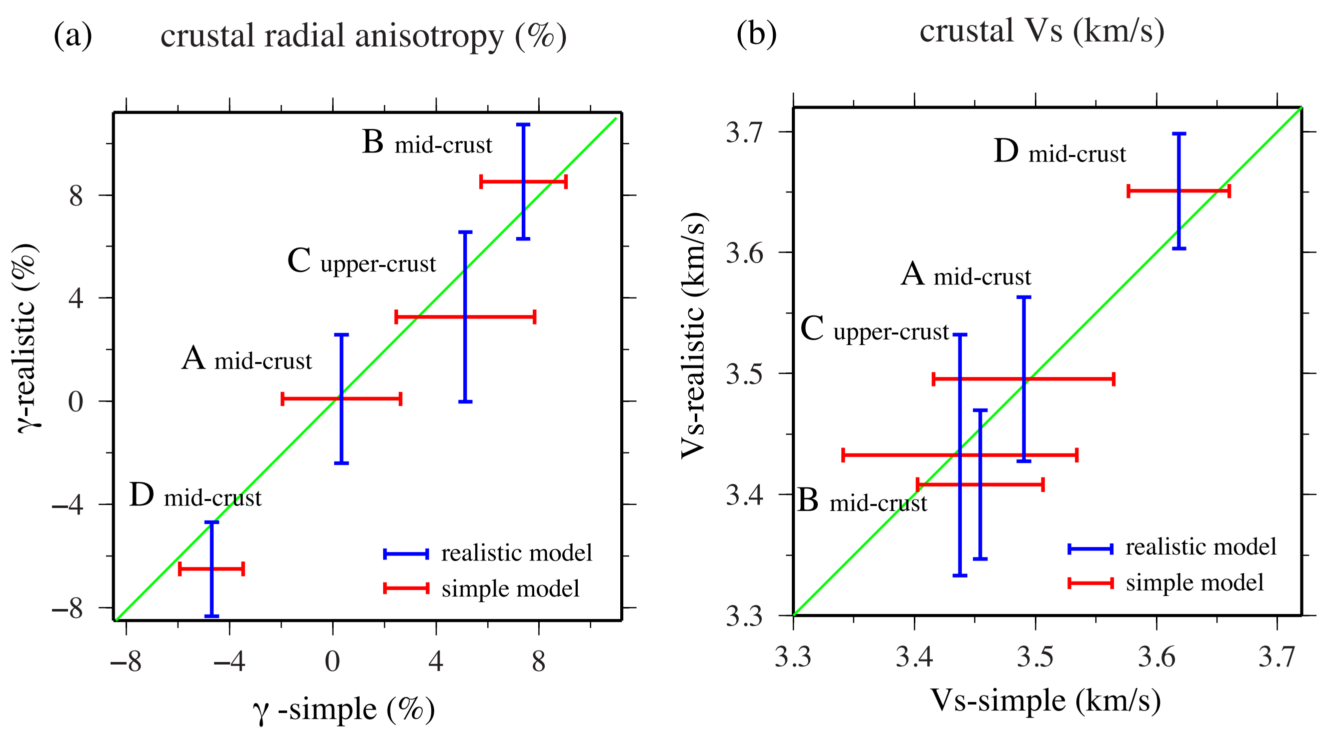

Figure 19. Comparison of the inversion results between the simple model of Vs radial anisotropy (γ-simple, red error-bars; $\varepsilon = 0$, $\eta = 1$) and the realistic model (γ-realistic, blue error-bars; $\varepsilon = 0.5\gamma$, $\eta = 1\text{-}4.2\gamma$) for (a) crustal Vs radial anisotropy and (b) crustal Voigt-averaged Vs. Both plots are for the four locations (A-D) identified in Fig. 1a. The results at locations A, B, and D are depth-averaged over the middle crust, while results at location C is depth-averaged over the upper crust. The half-widths of the error bars are the depth-averaged uncertainty (1σ). Green lines are the locus of points for identical results from the simple and realistic models of Vs radial anisotropy and all error bars overlap this line.

Figure 20

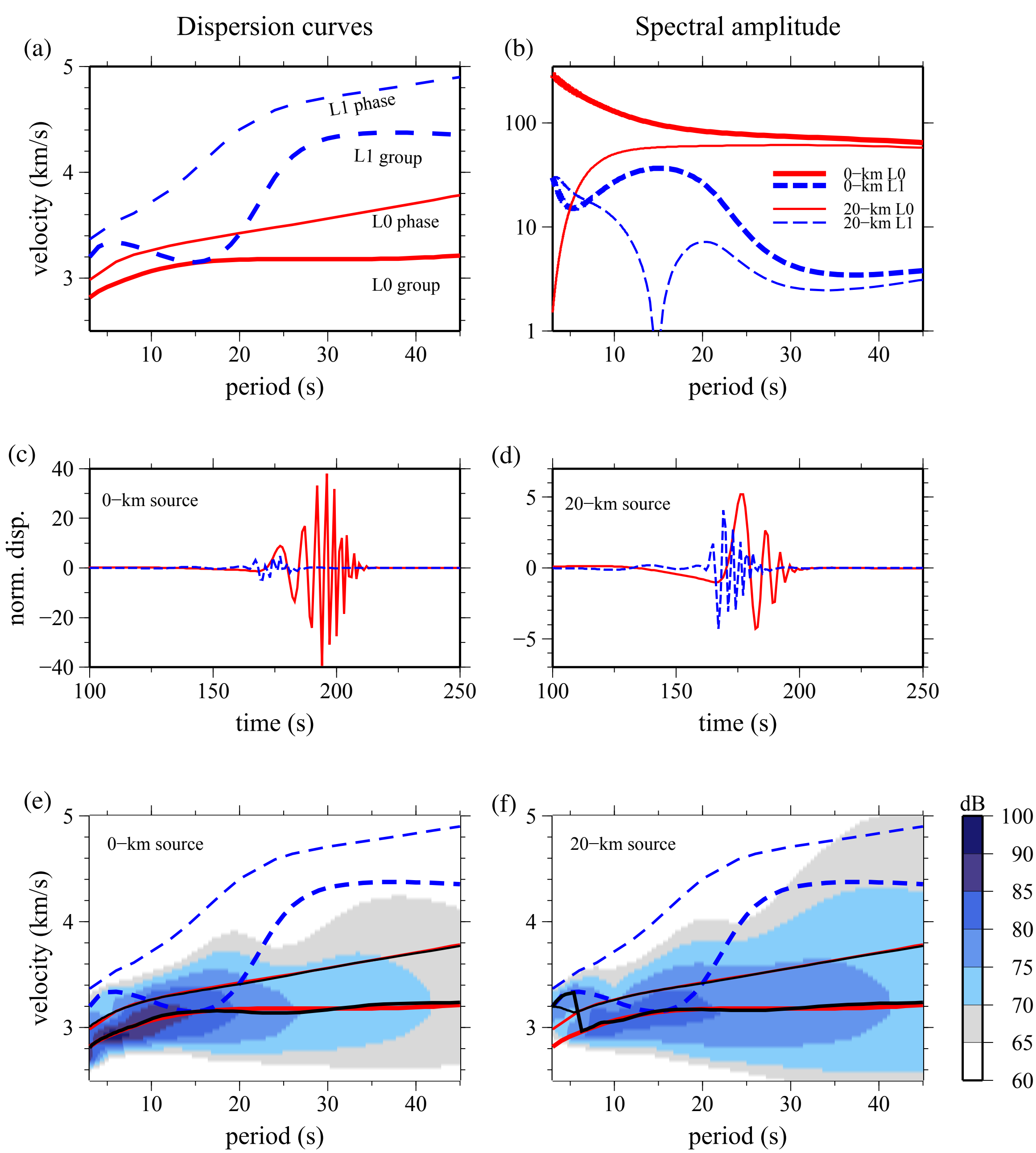

Figure 20. Synthetic results for the fundamental and higher mode Love waves. (a) Dispersion curves computed from an isotropic model based on the structure at location B in Fig. 1a. Red lines represent phase- and group- velocity dispersion curves of the fundamental model Love wave (L0) and dashed blue lines represent that of the first higher mode Love wave (L1). (b) Spectral amplitudes computed for a horizontal force at the surface (bold lines) or at 20 km depth (thin lines) for the fundamental Love wave (red lines) and first overtone Love wave (blue lines). (c) Green's function computed from the same model in (a) with a single horizontal force located at the surface (0-km depth). Red line indicates the fundamental Love wave; the dashed blue line is the first overtone Love wave. (d) Similar to (c), but computed with a single horizontal force located at 20-km depth. (e)-(f) Frequency-time analysis (FTAN) diagram for the superposition of the Green's functions shown in (c) and (d), respectively. Red and blue lines are the dispersion curves shown in (a) and black lines are the phase and group velocity dispersion curves measured using FTAN.

Figure 21

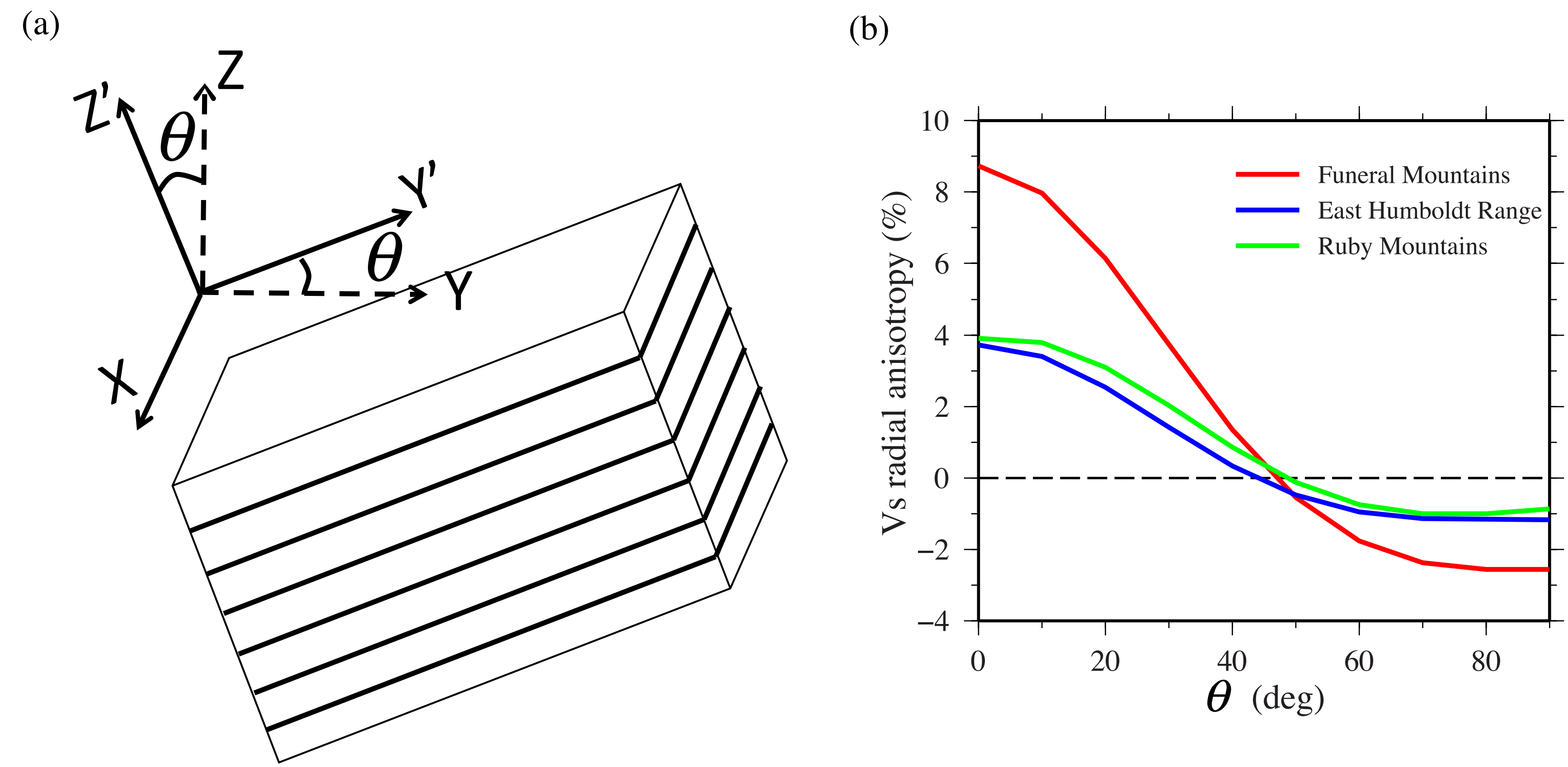

Figure 21. (a) Pictorial definition of the rotation angle θ for a hexagonally symmetric system. (b) Vs radial anisotropies, γ = (Vsh-Vsv)/Vs, plotted as a function of rotation angle θ, computed by re-orientating the elastic tensors of the crustal rock samples of Erdman et al. [2013]. Samples locations are identified by line color as indicated.